

The Pennsylvania State University  
The Graduate School  
College of Engineering

**APPLICATION OF TRADE SPACE VISUALIZATION TO DISCRETE AND  
CONTINUOUS COMPLEX DYNAMICAL SYSTEMS**

A Thesis in  
Aerospace Engineering  
by  
Daniel Jordan

© 2009 Daniel Jordan

Submitted in Partial Fulfillment  
of the Requirements  
for the Degree of  
Master of Science

May 2009

The thesis of Daniel Jordan was reviewed and approved\* by the following:

David B. Spencer

Associate Professor of Aerospace Engineering

Thesis Adviser

Timothy W. Simpson

Professor of Mechanical and Industrial Engineering

George A. Lesieutre

Professor of Aerospace Engineering

Head of the Department of Aerospace Engineering

\*Signatures are on file in the Graduate School.

## Abstract

Engineering design problems often contain correlations and trade-offs that may or may not be obvious or well-understood. As design problem complexity increases, decision makers find it more and more difficult to grasp these trade-offs effectively. The rapid growth of computing power now allows the simulation of millions of design alternatives. Understanding the trade-offs associated with these alternatives has never been more important. Trade space visualization tools are being developed to aid decision makers by allowing them to effectively explore a design space and identify the underlying trade-offs and nuances particular to a specific problem. These tools provide great potential in evaluating complex dynamical systems in the aerospace industry, among others.

This work explores the application of the Applied Research Lab Trade Space Visualizer (ATSV) to various discrete and continuous complex dynamical systems. First, the motivation for and capabilities of ATSV are covered. Then, ATSV is applied to two test problems: (1) a nonlinear mass-spring-damper system and (2) a simple two-burn impulsive spacecraft maneuver. Optimal Pareto solution sets are obtained for each system. Finally, the application of ATSV to more complicated continuous thrust spacecraft maneuvers is considered. The identification of a known optimal solution is followed by modification of the equations of motion to include a discrete hardware-side design variable, namely, engine type. Optimal solutions are located for each corresponding design variable option. A study is performed to understand the sensitivity of optimal trajectories to perturbations of the initial orbit. For each problem explored in this work, qualitative observations are made on the effectiveness of ATSV as a solution acquisition tool with particular emphasis on ATSV's visual steering capabilities.

## Table of Contents

List of Figures .....	v
List of Tables .....	vii
List of Symbols .....	viii
Chapter 1: Introduction .....	1
Chapter 2: Trade Space Visualization.....	2
2.1 Motivation.....	2
2.2 Multi-Dimensional Trade Space Visualization using ATSV .....	3
2.2.1 Plots.....	3
2.2.2 Brush and Preference Controls and Pareto Optimality .....	5
2.2.3 Datasets and Sampling.....	7
2.2.4 Evolutionary Search using Differential Evolution.....	9
2.3 ATSV-Excel-MATLAB System.....	10
Chapter 3: ATSV Test Problems .....	12
3.1 Nonlinear Mass-Spring-Damper .....	12
3.1.1 Problem Formulation .....	12
3.1.2 Results.....	14
3.2 Two-Burn Impulsive Spacecraft Maneuvers .....	16
3.2.1 Problem Formulation .....	16
3.2.2 Results.....	20
Chapter 4: Continuous-Thrust Orbital Maneuvers .....	28
4.1 Introduction.....	28
4.2 Previous Work .....	28
4.3 Problem Formulation .....	29
4.3.1 Constant Acceleration.....	29
4.3.2 Constant Thrust.....	30
4.4 Problem Specification.....	31
4.5 Results.....	32
4.5.1 Optimal Solution Acquisition via Visual Steering.....	33
4.5.2 Constant Acceleration.....	35
4.5.3 Constant Thrust.....	38
4.5.4 Constant Thrust Sensitivity Study .....	40
Chapter 5: Conclusions .....	48
5.1 Conclusions.....	48
5.2 Suggestions for Future Work .....	49
5.3 Suggested ATSV Improvements, Modifications, and Future Work.....	49
Appendix A: Examples of ATSV's Other Plot Types .....	51
Appendix B: Definition of $[M]$ .....	54
Appendix C: Partial Derivatives of $[M]$ .....	56
Appendix D: Excel Interfaces used for Continuous Thrust Problem Formulations .....	64
References.....	66

## List of Figures

Figure 1: Example Glyph Plot Showing 7 Variables Simultaneously .....	4
Figure 2: Example Scatter Plot Showing 3 Objective Functions.....	5
Figure 3: Brush/Preference Controls Window for Example Automobile Dataset.....	6
Figure 4: Brushed Car Dataset Showing Infeasible Designs (Gray), Feasible Designs (Red), and the Pareto Solutions (Marked by +). .....	7
Figure 5: Example of Guided Pareto Sampling .....	8
Figure 6: Example Excel Wrapper (left) that Contains Problem Model and Corresponding Settings for Exploration Engine in ATSV .....	10
Figure 7: Illustration of Nonlinear Mass-Spring-Damper System.....	12
Figure 8: Excel Front-End for Nonlinear Mass-Spring-Damper Test Problem.....	13
Figure 9: ATSV Exploration Engine Showing Decision Space Search Ranges for Nonlinear Mass-Spring-Damper Test Problem .....	14
Figure 10: Two Views of Glyph Plot Showing Preliminary Randomly Sampled Dataset with $cost$ , $v_{max}$ , and $freq_{closest}$ on the Spatial Axes. ....	15
Figure 11: Scatter Plots (a) Before a Guided Pareto Sampler Evolution with Guiding Points Marked by Black Circle and (b) Many Generations Later .....	15
Figure 12: Scatter Plot Showing Close-up of Non-Continuous Pareto Frontier Caused by Discrete Decision $m$ .....	16
Figure 13: Illustration of Classical Orbital Elements [20].....	17
Figure 14: Graphical Illustration of Two-Burn Transfer .....	18
Figure 15: Illustration of Flight Path Angle $\Phi$ and Out-of-Plane Angle $\beta$ . ....	18
Figure 16: Flowchart Depicting the Algorithm of the MATLAB Code.....	20
Figure 17: (a) Static Dataset Consisting of 10,000 Members. (b) Isosurface Showing Plane of Interest Near GEO Altitude and Pareto Solutions .....	21
Figure 18: Brush/Preference Controls Window for Orbital Problem Solution Set .....	22
Figure 19: (a) Static Dataset Brushed to Final Orbital Radius Between 40,000 and 45,000 km. (b) Histogram plot of Inputs Brushed in the Same Manner.....	22
Figure 20: (a) and (b) Two Perspectives of Densely Populated Region of Interest with Iso-surface at GEO Altitude.....	23
Figure 21: Scatter Matrix Plot of Variables of Interest.....	24
Figure 22: Solution Set and Pareto Frontier for Time of Flight vs. Total Impulsive Velocity Change ( $\pm 50$ km Brush) .....	25
Figure 23: Total Impulsive Velocity Change vs. Inclination Change from First Burn ( $\pm 50$ km Brush).....	25
Figure 24: Optimal Solution Acquisition via Visual Steering Flow Chart.....	33
Figure 25: Example Selection of Solutions of Interest used to Guide the Next Evolution .....	34
Figure 26: Progression of a Typical Search Using the Guided Pareto Sampler .....	35
Figure 27: Semi-Major Axis and Inclination as a Function of Time for Optimal Trajectory found within $\pm 500\%$ of Reference [22].....	36
Figure 28: Eccentricity as a Function of Time for Optimal Trajectory found within $\pm 500\%$ of Reference [22].....	37
Figure 29: Yaw $\alpha$ and Pitch $\beta$ as a Function of Time for Optimal Trajectory found within $\pm 500\%$ of Reference [22].....	37

Figure 30: Semi-Major Axis and Inclination as a Function of Time for Different $I_{sp}$ 's, Constant Acceleration Case Also Shown .....	39
Figure 31: Eccentricity as a Function of Time for Different $I_{sp}$ 's, Constant Acceleration Case Also Shown .....	39
Figure 32: Yaw $\alpha$ and Pitch $\beta$ Angles as a Function of Time for Different $I_{sp}$ 's, Constant Acceleration Case Also Shown.....	40
Figure 33: Semi-Major Axis and Inclination as a Function of Time for Perturbations of $a_o$ .....	41
Figure 34: Eccentricity as a Function of Time for Perturbations of $a_o$ .....	42
Figure 35: Yaw $\alpha$ and Pitch $\beta$ Angles as a Function of Time for Perturbations of $a_o$ .....	42
Figure 36: Semi-Major Axis and Inclination as a Function of Time for Perturbations of $i_o$ .....	43
Figure 37: Eccentricity as a Function of Time for Perturbations of $i_o$ .....	44
Figure 38: Control Angles as a Function of Time for Perturbations of $i_o$ .....	44
Figure 39: Semi-Major Axis and Inclination as a Function of Time for a Perturbation of $\Omega_o$ .....	46
Figure 40: Eccentricity as a Function of Time for a Perturbation of $\Omega_o$ .....	46
Figure 41: Control Angles as a Function of Time for a Perturbation of $\Omega_o$ .....	47

## List of Tables

Table 1: Structure of Static (.csv) Spreadsheet Data Files.....	7
Table 2: Impulsive Orbital Problem Decision Variables and Objectives with Respective Ranges/Preferences .....	19
Table 3: Initial and Desired Final Orbit Characteristics .....	20
Table 4: Attributes of Solution with Minimum $\Delta V_{Total}$ .....	26
Table 5: Comparison between ATSV Results and Minimum Combined Plane Change Algorithm .....	27
Table 6: Optimal Initial Adjoint Variables for LEO to GEO Transfer Found by Kechichian [22].....	28
Table 7: (a) Initial LEO “Baseline” Orbit Characteristics and (b) Final GEO Orbit Characteristics.....	31
Table 8: Summary of Explored Cases for Continuous Thrust Problem Formulations .....	32
Table 9: Typical Optimal Final Classical State .....	35
Table 10: “Near Optimal” Adjoint Variable Initial Conditions for Constant Thrust-Acceleration LEO to GEO Transfer .....	36
Table 11: Optimal Adjoint Variable Initial Conditions for Constant-Thrust LEO to GEO Transfers and Comparison with Constant Acceleration Transfer.....	38
Table 12: Optimal Adjoint Variable Initial Conditions for Constant Thrust LEO to GEO Transfer for Perturbations of $a_o$ .....	40
Table 13: Optimal Adjoint Variable Initial Conditions for Constant Thrust LEO to GEO Transfer for Perturbations of $i_o$ .....	43
Table 14: Optimal Adjoint Variable Initial Conditions for Constant Thrust LEO to GEO Transfer for a Perturbation of $\Omega_o$ .....	45

## List of Symbols

### Nonlinear Mass-Spring-Damper:

$m$	.....	Mass (kg)
$k_1, k_2, k_3$	.....	Linear, quadratic, and cubic spring stiffness (N/m <sup>order</sup> )
$c$	.....	Damping coefficient (N s/m)
$x$	.....	Linear amplitude (m)
$v$	.....	Linear velocity (m/s)
$\omega$	.....	Excitation frequency (rad/s)
$f_0$	.....	Excitation amplitude (m)
$v_{max}$	.....	Maximum velocity (m/s)
$freq_{closest}$	.....	Closest frequency to excitation (rad/s)
$cost$	.....	Cost function

### Classical Orbital Elements:

$a$	.....	Semi-major Axis (km)
$e$	.....	Eccentricity
$i$	.....	Inclination (degrees)
$\mathcal{Q}$	.....	Right ascension of the ascending node (degrees)
$\omega$	.....	Argument of periapsis (degrees)
$\theta$	.....	True anomaly (degrees)

### Two-Burn Impulsive Spacecraft Maneuvers:

$i_1$	.....	Initial inclination (deg)
$i_2$	.....	Final inclination (deg)
$r_2$	.....	Final orbital radius (km)
$\Delta V_1$	.....	First impulsive velocity change (km/s)
$\Delta V_2$	.....	Second impulsive velocity change (km/s)
$\Delta V_{Total}$	.....	Total impulsive velocity change (km/s)
$\Delta i_1$	.....	Inclination change delivered on the first burn (degrees)
$\Delta i_2$	.....	Inclination change delivered on the second burn (degrees)
$TOF$	.....	Time of flight (min)
$\Phi$	.....	Flight path angle (degrees)
$\beta$	.....	Out-of-plane angle (degrees)
$s$	.....	Percentage of total inclination change delivered on first burn (degrees)

### Continuous-Thrust Orbital Maneuvers:

$a, h, k, p, q, L$	.....	Equinoctial orbital elements
$\lambda_a, \lambda_h, \lambda_k, \lambda_p, \lambda_q, \lambda_L$	.....	Adjoint variables (sec/km), (sec), (sec), (sec), (sec), (sec/rad)
$\bar{x}_e$	.....	Equinoctial state vector
$\bar{\lambda}$	.....	Adjoint variable state vector
$f_t$	.....	Thrust acceleration magnitude (km/s <sup>2</sup> )
$\bar{u}$	.....	Thrust unit vector
$m$	.....	Spacecraft mass (kg)
$\alpha$	.....	In-plane control angle, yaw (deg)
$\beta$	.....	Out-of-plane control angle, pitch (deg)
$H$	.....	Hamiltonian
$f$	.....	Weighted sum, cost function



## **Acknowledgements**

The work presented in this thesis was supported by the National Science Foundation under Grant No. CMMI-0620948.

I would like to thank my advisor, Dr. David Spencer, for all the opportunities, guidance, and friendship he has given me throughout my undergraduate and graduate career. I would also like to acknowledge Dr. Timothy Simpson, Dr. Mike Yukish, Gary Stump, and the rest of the ATSV development team. I have learned so much from you all.

Finally, I wish to thank my family for their constant love and support throughout my life. They have always given me the tools I need to succeed.

# Chapter 1: Introduction

In industry, a seemingly infinite number of engineering design problems are modeled by complex dynamical systems. Practical analyses of these systems often reveal that solving real-world problems is rarely as simple as stakeholders wish. Frequently, a decision maker must consider trade-offs that exist between competing objectives and decisions of interest. The rapid growth of computational and graphical power of personal computers in recent years has sparked the scientific community's interest in visualizing complex problem trade spaces, trade space optimization using evolutionary strategies, and the ability to enhance search by integrating the human back into the automated optimization process.

This thesis applies trade space visualization software to several discrete and continuous complex dynamical systems in order to

1. Locate optimal solutions or solution sets,
2. Gain a practical understanding of underlying correlations within datasets, and
3. Comment on the efficacy of solution acquisition through human-in-the-loop optimization via visual steering.

A thorough explanation of trade space visualization and the software used in this work is given in Chapter 2. The subject of Chapter 3 is the application of trade space visualization software to two simple test problems: a nonlinear mass-spring-damper system and a two-burn impulsive spacecraft maneuver. Continuous-thrust orbital maneuvers and the acquisition of optimal spacecraft trajectories via visual trade space exploration are the focus of Chapter 4. General conclusions drawn from this research are the subject of Chapter 5.

## Chapter 2: Trade Space Visualization

Engineering design problems often contain correlations and trade-offs that may or may not be obvious or well-understood. For simple engineering problems, these trade-offs may be trivial or even negligible. As design problems become more and more complex, it is necessary to develop tools that permit decision makers to grasp these nuances effectively. Trade space visualization tools are designed for this purpose. This chapter describes in detail the motivation for trade space visualization (TSV) and the TSV software used in this thesis, the Applied Research Lab Trade Space Visualizer (ATSV).

### 2.1 Motivation

Complex design can be considered a decision making process, where a classical approach to the optimal decision process can be described by [1]:

- Identify options
- Identify ways to evaluate options
- Weight each evaluation dimension
- Do the rating
- Pick the option with the highest score

This method, *rational choice analyses*, is taught in engineering and business curriculums across the country. With this approach, rational choices are made after applying game-theoretic or statistical-theoretic methods to a problem [2]. More recently, there has been a body of research focusing on observing expert decision makers. As a result, some have proposed new ideas on how optimization-based design should be approached.

Balling has introduced a new paradigm for the optimization-based design process which he calls *Design by Shopping* [3]. He notes that designers using traditional optimization-based design processes were often left unsatisfied with their results. This is usually the result of the design problem being improperly formulated when the objectives and constraints are initially defined. “The objectives and constraints used in optimization were not what the owners and stakeholders really wanted... in many cases, people don’t know what they really want until they see some designs.” Furthermore, in a psychological study, Wilson and Schooler [4] have found that people often do worse at decision making tasks when they are asked to explain the reasons for their preferences. The *Design by Shopping* process allows a decision maker to first explore the design space in order to form “realistic expectations of what is possible” [3]. This gives the user more control over the optimization process by first allowing them to form an *a posteriori* articulation of preferences based on visualization and then choose an optimal design based on those preferences [5].

When exploring a trade space, equally optimal solutions with respect to multiple conflicting objectives are known as Pareto optimal points within the data set. Pareto optimality is described in detail in Section 2.2.2. Finding the Pareto set in a large design space without efficient search capabilities can be arduous. A suitable set of computationally-efficient algorithms have been developed as part of our previous work

(See References [6]-[8]) and have since been incorporated into ATSV, allowing us to evolutionarily search the design space and interactively “steer” solutions during the exploration process.

Within the visualization community, interactive optimization-based design methods fall mainly into the category of computational steering whereby the user (i.e., designer) interacts with a simulation during the optimization process to help “steer” the search process toward what looks like an optimal solution. The steering process allows the designer to gain new perspectives on correlations within the problem and use intuition, heuristics, or some other method to adjust the design space to move towards solutions that they feel are promising. Visual Steering can be defined as the process of observing a search and making adjustments to it in real time as the user sees fit. It allows the user to simultaneously explore the trade space and exploit new information and insights as they are gained [9]. On the importance of visualization in engineering optimization, Messac and Chen [10] noted: “If effectively exploited, visualizing the optimization process in real time can greatly increase the effectiveness of practical engineering optimization.” Furthermore, Ng [11] advocates the use of data visualization and interaction to support the designer in making informed decisions and trade-offs during multiobjective optimization. Many others argue that visualization should be considered a solution tool and that “human-in-the-loop” optimization has significant advantages over black-box search algorithms [12], [13].

The Applied Research Lab (ARL) Trade Space Visualizer (ATSV)\* used in this research has been developed to support the exploration phase of the design process [14]-[16]. Throughout this work, ATSV is utilized as a trade space exploration tool for evaluating design and objective spaces. Section 2.2 more fully describes the functionality of the in-development ATSV software.

## **2.2 Multi-Dimensional Trade Space Visualization using ATSV**

ATSV is a Java application that displays multi-dimensional trade spaces using glyph, histogram, scatter, scatter matrix, and parallel coordinate plots [16]. ATSV offers combinations of visualization and evaluation tools that aid in problem solving such as: higher dimensional plots, plot linking, brush controls, preference shading, and real-time visualization of evolutionary search [14]-[16]. The software is designed such that the user can implement visual steering commands to navigate multi-attribute trade spaces via various samplers. Since ATSV is developed in Java, its cross-platform compatibility allows relatively simple model integration, giving it an advantage over many commercially-available software systems. The following subsections describe ATSV features that are used in this thesis including plots, preference and brush controls, sampling types, and ATSV’s evolutionary search technique.

### **2.2.1 Plots**

For complex decision and objective spaces, the glyph plot is the key to visualizing many dimensions simultaneously. The glyph plot is capable of displaying eight dimensions

---

\* “Applied Research Laboratory Trade Space Visualization”, <http://www.atsv.psu.edu>, date cited 3/01/09.

simultaneously: three spatial dimensions as well as point size, color, transparency, orientation, and text overlay. Using the mouse, the user can navigate through the dataset, plotting any variable with respect to any of the other seven variables. Figure 1 shows an example glyph plot which displays seven variables simultaneously: three objectives, three decisions, and a preference function.

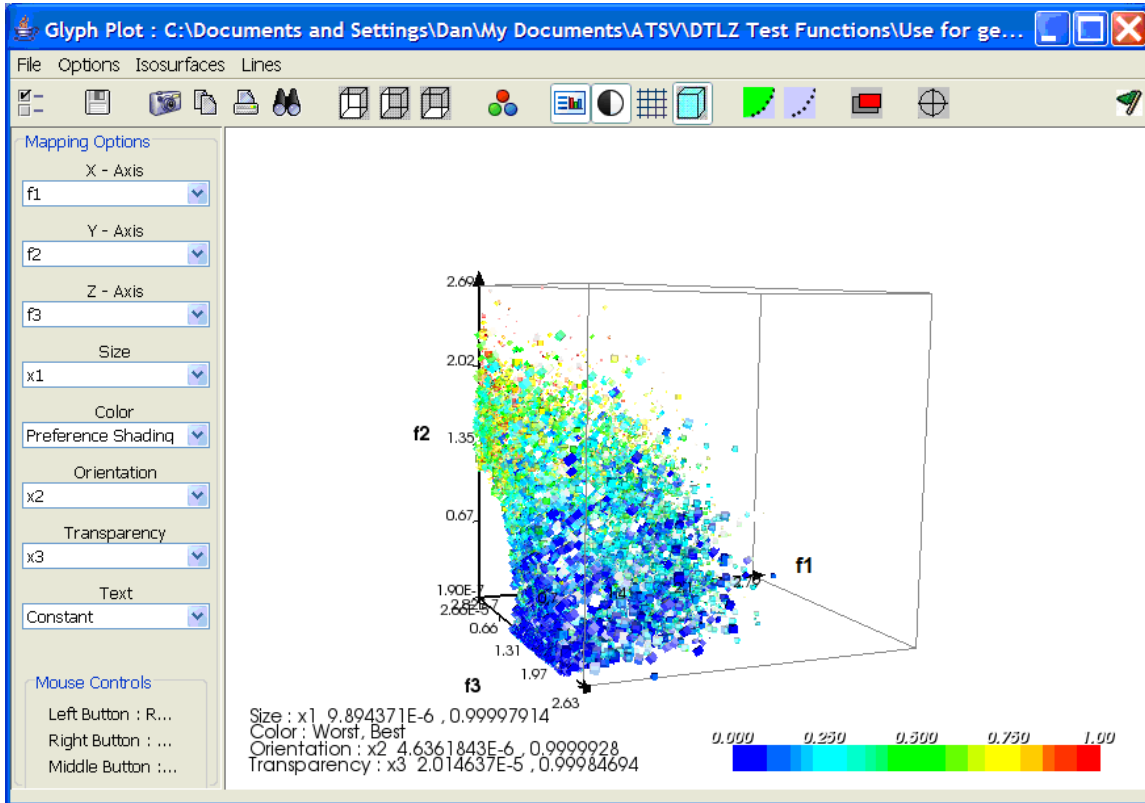


**Figure 1: Example Glyph Plot Showing 7 Variables Simultaneously**

Objective functions  $f_1$ ,  $f_2$ , and  $f_3$  are plotted on the spatial axes. Decision variables  $x_1$ ,  $x_2$ , and  $x_3$  are represented by point size, orientation, and transparency respectively. In Figure 1, point color represents the quality of solutions based on the preference controls specified by the user. A detailed explanation of preference controls can be found in Section 2.2.2.

The two-dimensional scatter plot is preferred for simpler problems containing less decisions and objectives. The scatter plot allows the user to visualize two spatial dimensions and a third dimension represented by color. An example scatter plot is shown in Figure 2. Objectives  $f_1$  and  $f_2$  are plotted on the x and y spatial axes and objective  $f_3$  is represented by the color contour.

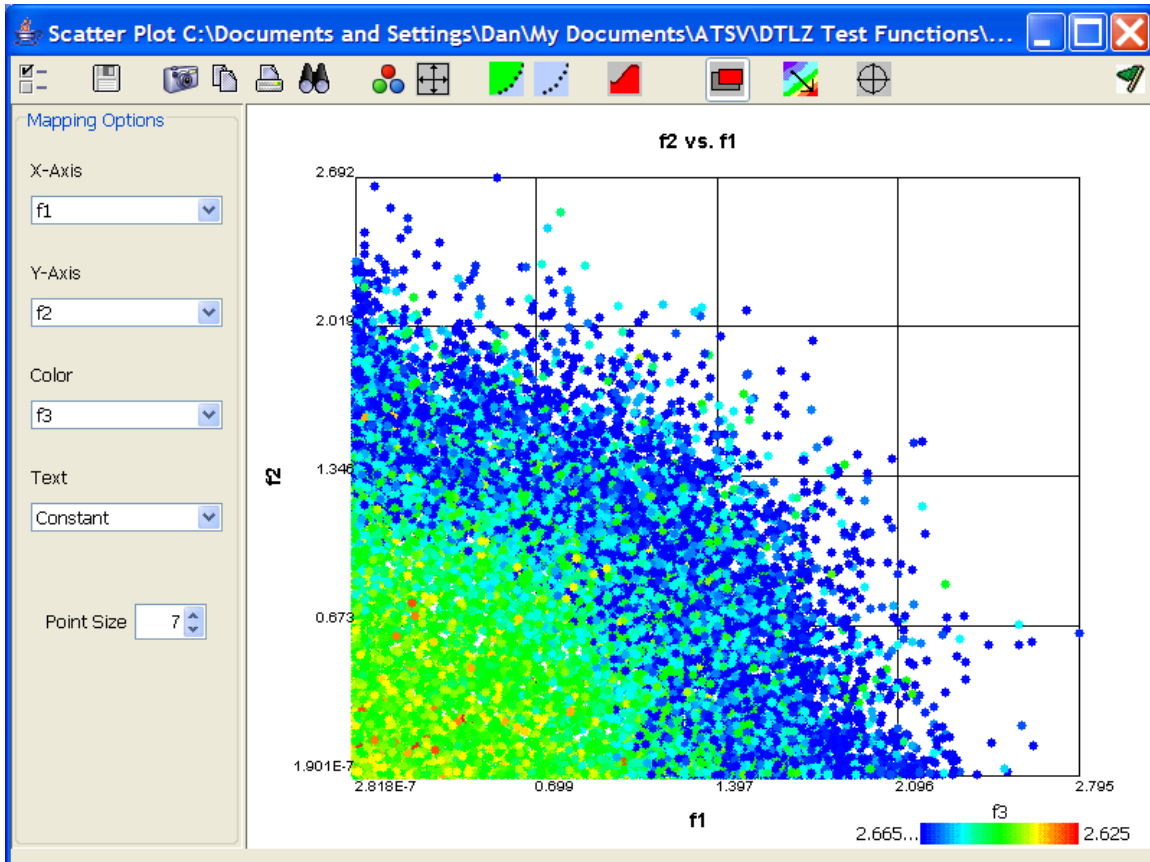


**Figure 2: Example Scatter Plot Showing 3 Objective Functions**

ATSV can also display scatter matrix, parallel coordinates, and histogram plots. The scatter matrix shows thumbnail images of 2D scatter plots showing each variable versus every other variable. This allows the user to quickly locate and recognize patterns in decision space and objective function data. The parallel coordinates plot shows graphical representations of relationships between design inputs and objective functions as lines between values. It is useful for identifying connections and relationships between variables of interest that might otherwise be difficult to discover. Statistical distributions of values of design inputs and objective functions are visualized with the histogram plot. This type of visualization is useful for understanding how design input distributions may affect objective functions of interest. The two-dimensional histogram plot allows the user to visualize distributions of two variables of interest simultaneously. Examples of scatter matrix, parallel coordinates, and histogram plots can be found in Appendix A.

### **2.2.2 Brush and Preference Controls and Pareto Optimality**

For each decision space and objective function of interest, there is the ability to view only specified points between certain feasible ranges by “brushing” the dataset [16]. Preference controls allow the user to specify a desired minimization or maximization of specific objective functions, permitting ATSV to filter the corresponding Pareto frontier (optimal solution set) from the dataset.

The Pareto frontier, also known as the Pareto set or non-dominated set, is the set of solutions that are simultaneously optimal in each objective of interest. These points are considered “non-dominated” because no other points in the dataset are more preferred when considering all objectives simultaneously [17]. Accordingly, “dominated” solutions are those which are less optimal in one or more objectives than the non-dominated solutions.

As an example, ATSV is used to explore a trade space populated with 277 different automobiles. Each automobile has unique properties: highway efficiency, horsepower, model, make, year, fuel capacity, number of cylinders, etc. Some or all of these properties may be of interest to the decision maker. For example, the decision maker may have preferences on two objectives for an automobile trade space: maximize horsepower and maximize highway fuel efficiency. ATSV Brush and Preference Controls can be added for each decision or objective of interest. If the decision maker has knowledge of what range of these values are feasible, the minimum and maximum values can be entered to “brush” out infeasible values. For example, the user can reduce the visible dataset to automobiles with horsepower between 150 and 250, and highway efficiency above 20 mpg. The Brush/Preference Controls window corresponding to these settings is shown in Figure 3.

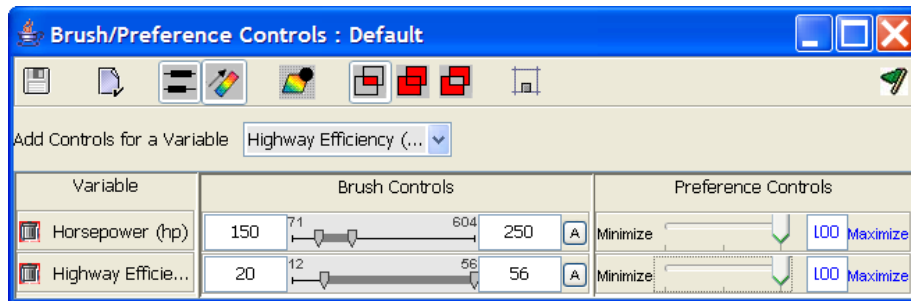


**Figure 3: Brush/Preference Controls Window for Example Automobile Dataset**

The resulting brushed dataset showing highway efficiency versus horsepower might look something like Figure 4. The gray points show designs rendered infeasible as specified by the brush controls. The red points are feasible solutions within the specified ranges. Points marked with a black + symbol show the Pareto frontier formulated from the preference controls [6], [16]. These are the solutions that mutually maximize horsepower and highway efficiency and lie within the feasible objective space.

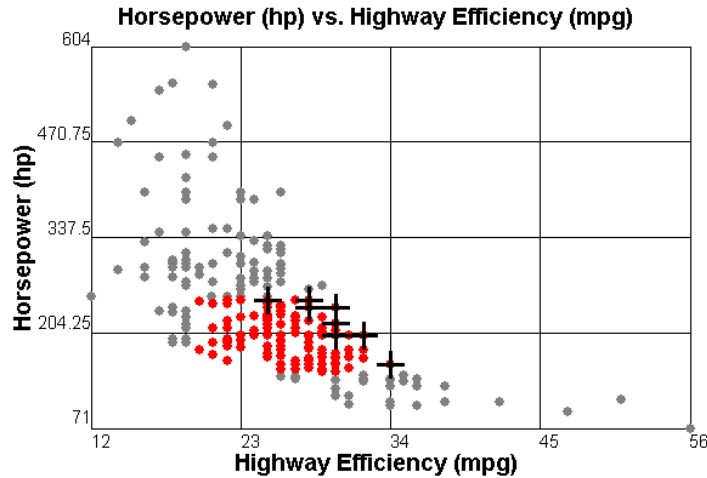


**Figure 4: Brushed Car Dataset Showing Infeasible Designs (Gray), Feasible Designs (Red), and the Pareto Solutions (Marked by +).**

### 2.2.3 Datasets and Sampling

ATSV can explore design spaces statically or dynamically. Static data sets, generated from an external model, are read from comma-, space-, or tab-delimited text or spreadsheet files (filename.csv in Excel). Decision variables and objective functions and their values for each solution alternative are organized within these files as shown in Table 1.

**Table 1: Structure of Static (.csv) Spreadsheet Data Files**

Solution Alternative	Decision Variable #1	Decision Variable #2	Objective Function #1	Objective Function #2	...	Objective/ Decision #n
1	<value>	<value>	<value>	<value>	...	...<value>
2	<value>	<value>	<value>	<value>	...	...<value>
3	<value>	<value>	<value>	<value>	...	...<value>

Dynamic datasets more fully utilize the full potential of ATSV by integrating visual steering into the exploration process. Dynamic datasets are generated by integrating ATSV with external code via a “wrapper” that allows ATSV to directly sample design inputs to generate new design alternatives and visualize objective function outputs. The process of sampling a design input and generating a new solution alternative is also known as a single function evaluation.

Currently, ATSV has the ability to specify five types of visual steering commands to generate new data by random sampling, manual sampling, attractor-based sampling, preference-based sampling, and Pareto sampling [16]. Random sampling will randomly generate values for each design input between specified limits with uniform or normal distributions. This type of sampling is designed to populate the objective space with



random points, possibly to attempt to identify general trends early in the exploration process. Manual sampling allows the user to precisely pick design input values using slider bars and visualize the corresponding single solution in the objective space. Preference based sampling will generate points in a region of interest specified by the weights on objectives of interest in the Preference Controls. Pareto sampling will generate solutions along the Pareto frontier. The Pareto frontier must be defined by the user by specifying a direction of preference for each objective function under consideration. ATSV’s attractor based sampling creates points in the objective space close to a desired location, specified by an “attractor”.

Attractors, specified in the interface by the  $\oplus$  icon, generate points near a specified n-dimensional location in the trade space. These attractors, also referred to as point samplers, can be used to create a cluster of points in the trade space in order to “fill gaps” or explore a specific space in more detail. An evolutionary algorithm, specifically Differential Evolution [18], is used to guide the sampling process for the attractor, Pareto, and Preference samplers in order generate points in the objective space from n-dimensional discrete and continuous inputs [14]. Details on the implementation of Differential Evolution within ATSV can be found in Section 2.2.4.

A new modification of ATSV’s Pareto sampler, the guided Pareto sampler, allows the user to select some or all of the initial population from a current dataset to be used in the evolution process [16]. This can be used to search specific regions of the objective space by biasing the initial population based on user intuition or knowledge gained from a previous evolution. This type of “human-in-the-loop” evolution provides obvious advantages over traditional black-box evolutionary strategies by integrating the solution process with heuristics that cannot yet be modeled by software. In Figure 5, an example of ATSV’s guided Pareto sampling is shown for an arbitrary objective space consisting of objectives  $f_1$ ,  $f_2$ , and  $f_3$ . The plot on the left shows the selection of 11 points used to guide the evolution process, and the plot on the right represents the same dataset a few generations later. Note that the new solutions produced in the evolution process are similar to the points selected for guiding.

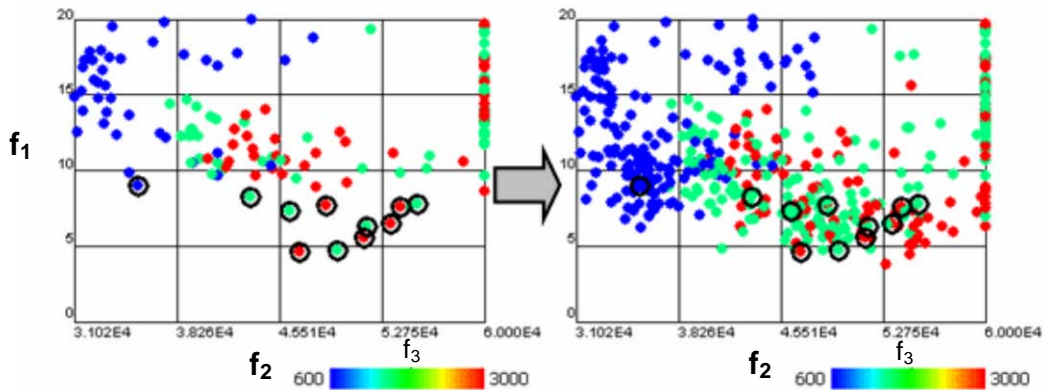


**Figure 5: Example of Guided Pareto Sampling**

## 2.2.4 Evolutionary Search using Differential Evolution

Differential Evolution (DE) is an evolutionary algorithm that was created by Price and Storn and has gained popularity in recent years due to its relatively simplistic technique and robust capabilities with regard to optimization [18]. DE is a real-coded algorithm that uses the fundamental operators of mutation, crossover, and selection.

Initially, a random population ( $P_x$ ) of  $Np$   $D$ -dimensional vectors are generated. The elements of a vector of size  $D$  represent  $D$  individual design parameters (decisions) and a population of size  $Np$  represents  $Np$  vectors in the evolution process. Once the current population of target vectors  $P_x$  is initialized, DE produces an intermediate population of  $Np$  mutant vectors ( $P_{v,g}$ ). These mutant vectors are the result of adding a scaled vector difference between two other random vectors to a third base vector. A trial population ( $P_u$ ) is then generated by recombining each vector in the current population with a mutant vector. The crossover probability in this recombination technique determines how many of the parameters from a mutant vector are copied to the target vector. These trial vectors are then compared against their corresponding target vectors; if a trial vector has an equal or better fitness than its corresponding target, it replaces the target vector in the next generation [18]. Analogous to biological evolution, each time this process repeats a new “generation” of solutions is created.

There are many DE strategies and they are described succinctly using the following notation: DE / base vector choice method / # of vector differences added to base vector / distribution of parameters donated by mutants. For example, the DE strategy “DE/Rand/1/bin” chooses a base vector randomly, one vector difference is added to the base vector, and the number of parameters donated by the mutant vector follows a binomial distribution [18].

Though DE was originally designed for single objective optimization problems, it can be extended into the multi-objective optimization realm by modifying the selection procedure using a Pareto-based approach [17]. The Pareto Differential Evolution method incorporates the fast nondominated sorting and ranking selection scheme developed by Deb et al. used in the successful NSGA-II algorithm [19]. After the trial population is generated from the mutation and crossover operators, it is combined with the parent population and the combined set undergoes a nondominated sorting and ranking. The ranking procedure used in the NSGA-II algorithm incorporates the use of non-dominated rank and diversity rank to promote Pareto frontier convergence and prevent solution crowding [17], [19]. Using this technique, the next generation is then comprised of the best  $Np$  members of the population and the entire process repeats until some stopping criterion is met. In ATSV’s Pareto sampler, which employs the aforementioned modified DE technique, the stopping criterion is set to a maximum number of generations by way of modifying the maximum number of dataset members [16].

## 2.3 ATSV-Excel-MATLAB System

In order to fully exercise the search and visualization capabilities of ATSV, it is necessary to directly link ATSV to the problem model. Currently, ATSV links efficiently with Java, C++, and Excel wrapper files. These wrapper files “wrap” around the problem model, making integration into ATSV simpler; it bypasses the modification of the model code directly and instead links ATSV with any model that accepts inputs and delivers outputs.

For most problems, the wrapper type that is most easily created and maintained is the Excel wrapper because of its widespread use and simple user interface. An Excel wrapper is simply an Excel spreadsheet that links directly to ATSV. The spreadsheet contains cells for each problem input and output. The spreadsheet can be used as a link to another program (e.g., MATLAB) or can contain the problem model itself.

Figure 6 shows a simple example of an Excel wrapper that contains the problem model and the corresponding settings for the Exploration Engine in ATSV. Here, cells read or written by ATSV are highlighted in yellow; the decision variables  $x_1$  and  $x_2$  are listed in the left table, and the objectives  $f_1$  and  $f_2$  are listed in the right table. In this example, the problem model is simply the addition of  $x_1$  and  $x_2$  for objective  $f_1$  and the division of  $x_1$  by  $x_2$  for objective  $f_2$ .

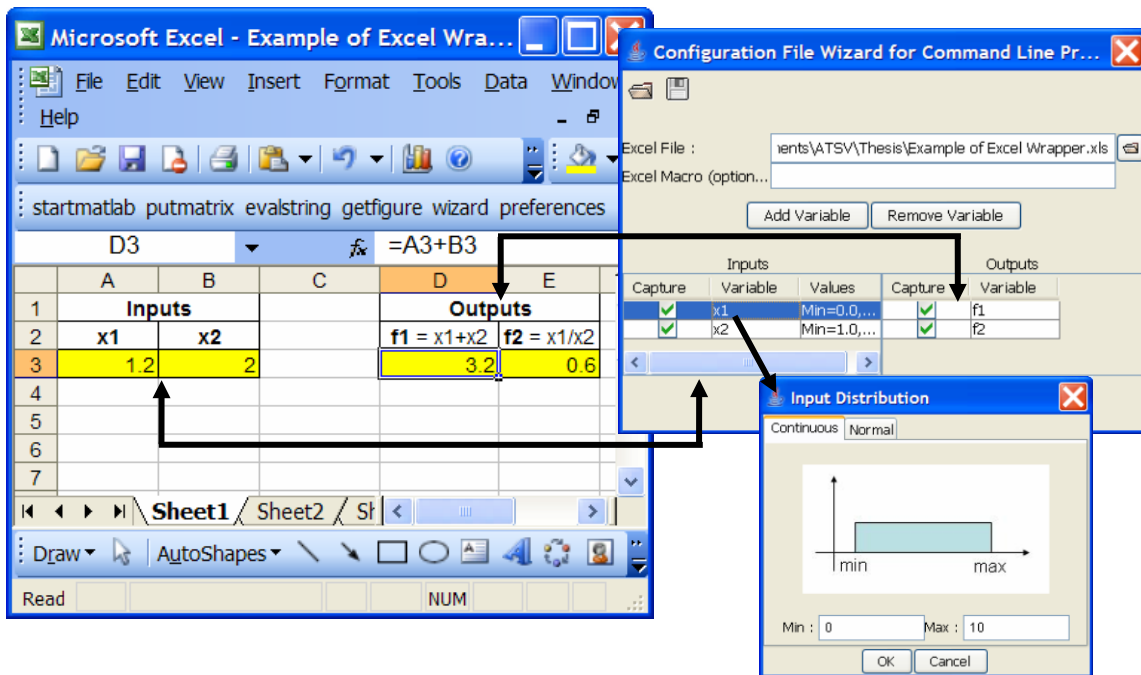


**Figure 6: Example Excel Wrapper (left) that Contains Problem Model and Corresponding Settings for Exploration Engine in ATSV**

The top right window in Figure 6 shows the creation of the Exploration Engine configuration file used to link ATSV to Excel. This is how variables are assigned to specific cells and how input sampling boundaries are set. Once the Exploration Engine is

created, ATSV can explicitly change inputs  $x_1$  and  $x_2$  in Excel and read the outputs  $f_1$  and  $f_2$  after those cells are updated by the problem model.

Engineering problems requiring optimization are often more complex than the library of mathematical functions Excel offers. For problems that require integration of dynamical equations of motion, it is convenient to have the ability to utilize any of the integration functions built into MATLAB libraries. This can be accomplished by using an Excel wrapper that links to MATLAB via the Spreadsheet Link. Developed by Mathworks as an add-on to MATLAB, Spreadsheet Link allows Excel to call MATLAB functions directly from a cell formula. The only downfall of the integration of MATLAB into Excel is the trade-off associated with MATLAB, primarily the trading of robustness for computational efficiency. It can be argued that MATLAB's built-in integration functions are not the fastest computational integrators. Developing a Java program which integrates the equations of motion may actually be faster per function evaluation. However, the time it would take to develop such software may outweigh any overall gains it may inherently have. For this reason, dynamical equations of motion are numerically integrated in MATLAB, which is then connected to ATSV via the method described in this section. In the next chapter, the application of ATSV to two simple test problems is explored.

## Chapter 3: ATSV Test Problems

### 3.1 Nonlinear Mass-Spring-Damper

In order to test ATSV's visual steering capabilities on a problem that requires integration of dynamical equations of motion, a simple nonlinear mass-spring-damper problem is developed and tested first.

#### 3.1.1 Problem Formulation

A simple drawing of the nonlinear mass-spring-damper system is shown in Figure 7. The mass  $m$  is restricted to linear motion with amplitude  $x$  and velocity  $v$ . The mass is subject to the periodic forcing function  $f(t)$  as well as a linear damping coefficient  $c$  and linear, quadratic, and cubic spring stiffnesses  $k_1$ ,  $k_2$ , and  $k_3$  respectively.

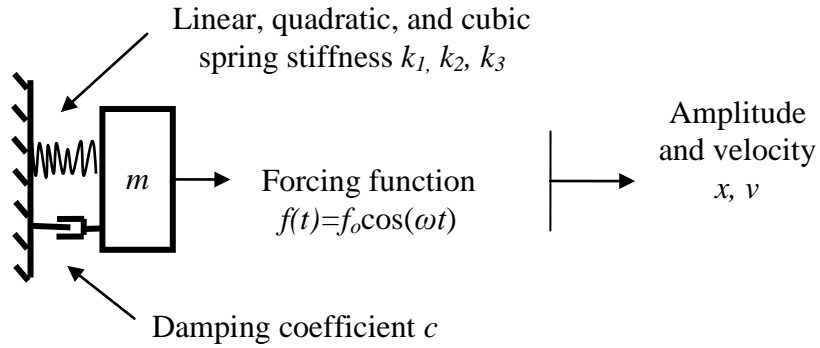


**Figure 7: Illustration of Nonlinear Mass-Spring-Damper System**

From simple vibration theory, the system state vector  $\bar{y}$  and its dynamical equations of motion are defined as:

$$\bar{y} = \begin{bmatrix} x \\ v \end{bmatrix} \quad (1)$$

$$\bar{y} = \begin{bmatrix} \dot{x} \\ \dot{v} \end{bmatrix} = \begin{bmatrix} v \\ \frac{f_o \cos(\omega t)}{m} - 2\xi\omega_n v - \omega_n^2 x - \frac{1}{m}(k_2 x^2 - k_3 x^3) \end{bmatrix} \quad (2)$$

$$\text{Damping Ratio } \xi = \frac{c}{2} \sqrt{\frac{m}{k_1}} \quad (3)$$

$$\text{Natural Circular Frequency } \omega_n = \sqrt{\frac{k_1}{m}} \quad (4)$$

The Excel front-end for this problem is shown in Figure 8. The design space is summarized in the topmost table, the initial conditions and integration options are listed in the middle table, and the objective space is summarized in the bottommost table. The

“execute” button exists as a debugging tool and will run a single model simulation without ATSV.

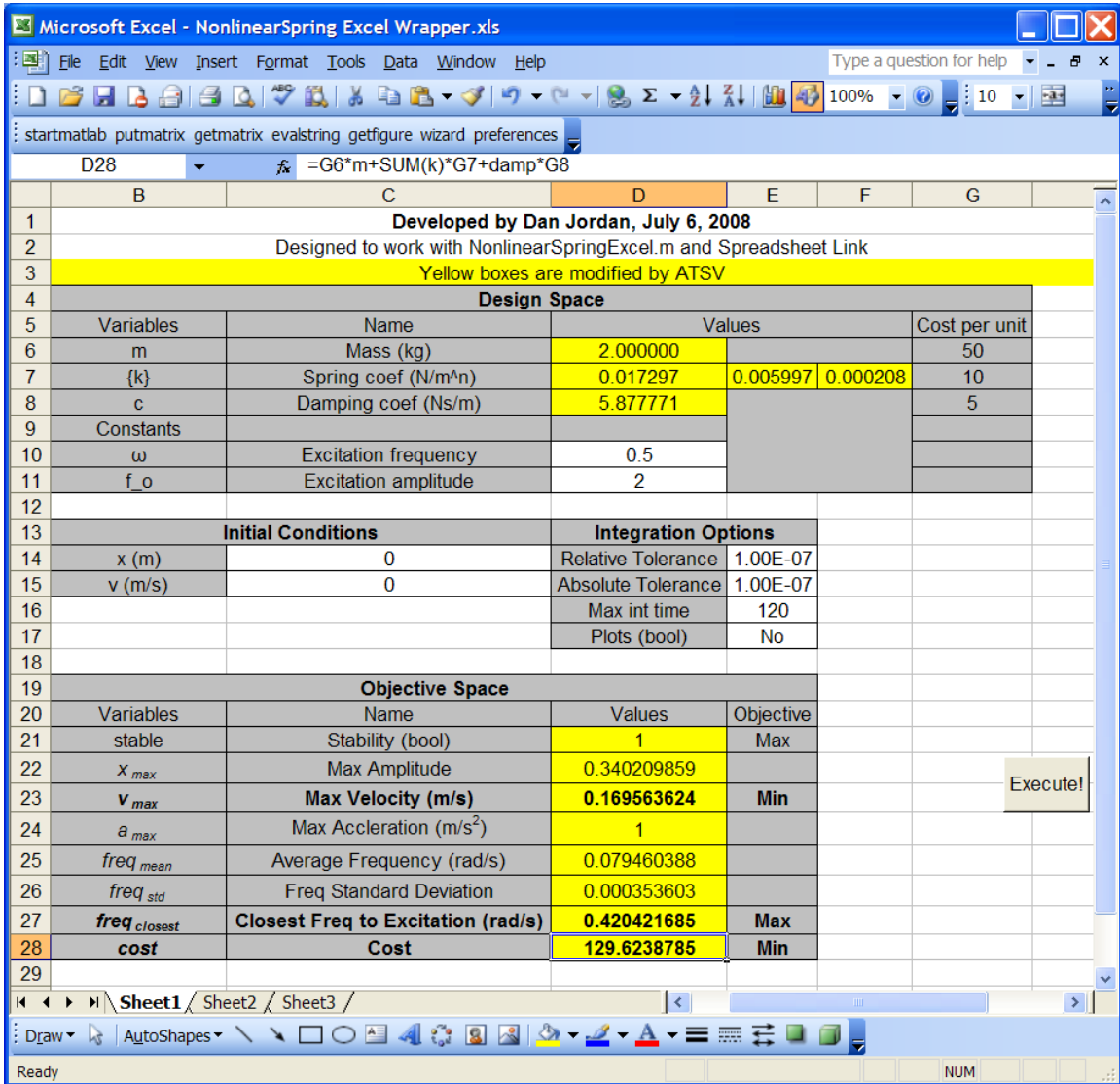
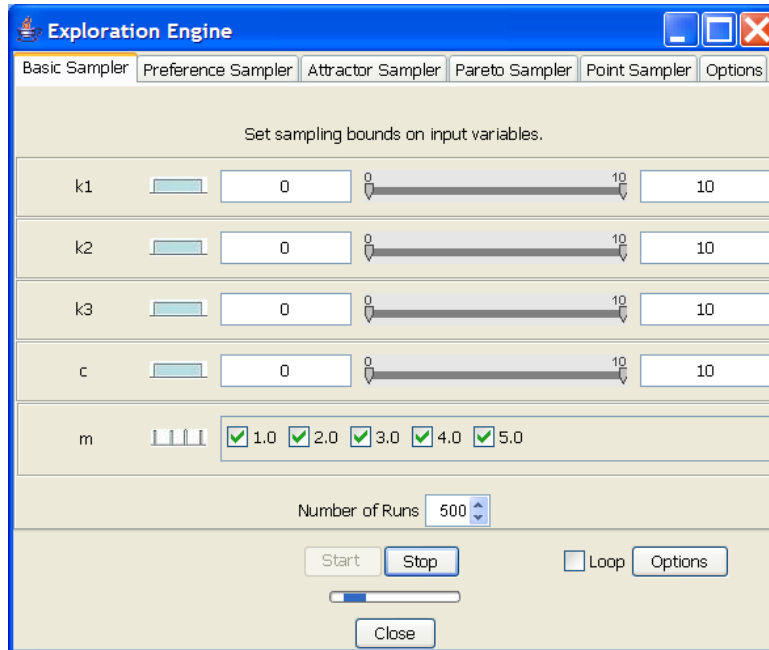


Figure 8: Excel Front-End for Nonlinear Mass-Spring-Damper Test Problem

Cells read or written by ATSV are highlighted in yellow. Note that the decision space consists of five components which describe the specific physics of the problem ( $m$ ,  $k_1$ ,  $k_2$ ,  $k_3$ ,  $c$ ) subject to an external forcing function described by an excitation frequency and amplitude ( $\omega$ ,  $f_o$ ). Not all of the objectives listed in the bottommost table are necessarily of interest; they are included in this Exploration Engine in the event new objectives are to be explored with the same wrapper. For this particular test problem, the objectives of interest ( $v_{max}$ ,  $freq_{closest}$ , and  $cost$ ) are shown in bold. These objectives are to maximize the difference between the excitation frequency ( $f_o$ ) and the first mode frequency of the vibration and simultaneously minimize the maximum absolute velocity experienced by the mass ( $m$ ) and the cost function. The cost function is a hypothetical function which models the “cost” of the system based on cost per unit of individual components ( $m$ ,  $k_1$ ,

$k_2, k_3, c$ ). The cost per unit is arbitrarily defined here in cells G5-G8 and the resulting summation, shown in the Formula Bar, can be found in cell D28 in Figure 8.

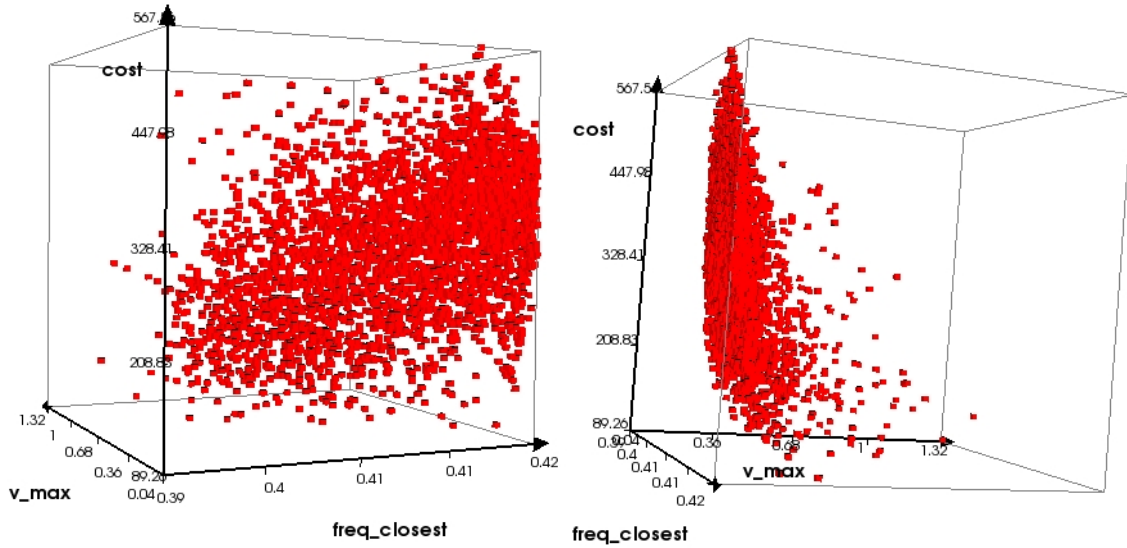
The ATSV Exploration Engine used to generate the results in Section 3.1.2 is shown in Figure 9. The decision space search ranges are arbitrarily defined as  $[0, 10]$  (continuous) for  $k_1, k_2, k_3$ , and  $c$  and  $[1, 2, 3, 4, 5]$  (discrete) for  $m$ . The external forcing function parameters are chosen to be  $\omega = 0.5$  rad/s and  $f_o = 2$  N.



**Figure 9: ATSV Exploration Engine Showing Decision Space Search Ranges for Nonlinear Mass-Spring-Damper Test Problem**

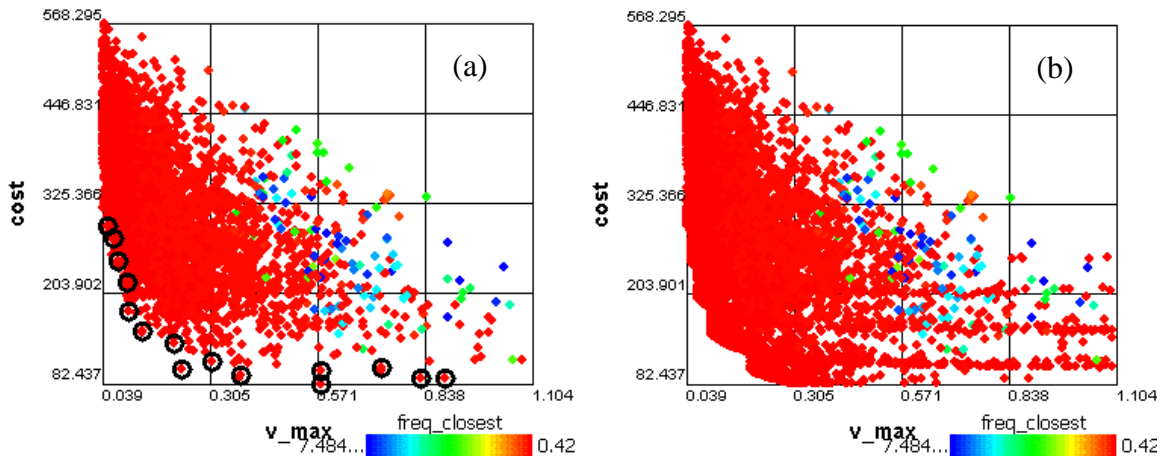
### 3.1.2 Results

Figure 10 shows a glyph plot of 5000 randomly sampled solutions with the  $cost$ ,  $v_{max}$ , and  $freq_{closest}$  objectives plotted on the spatial axes. From inspection, there is competition between the minimization of  $cost$  and  $v_{max}$  but the maximization of  $freq_{closest}$  does not compete with any other objective.



**Figure 10: Two Views of Glyph Plot Showing Preliminary Randomly Sampled Dataset with *cost*, *v\_max*, and *freq\_closest* on the Spatial Axes.**

Since one of the objectives does not compete with the others, the dataset can be more easily visualized without information loss as a scatter plot. Scatter plots of the competing objectives *cost* and *v\_max* with *freq\_closest* as the color contour are shown in Figure 11(a) and (b). Solutions from the randomly sampled dataset are used to guide the evolution process using the guided Pareto sampler. These points are marked by a black circle in Figure 11(a). Figure 11(b) shows the dataset many generations later. By selecting points near the Pareto frontier in the preliminary dataset to guide the evolution, solutions are generated along the *cost* vs. *v\_max* Pareto frontier quickly.



**Figure 11: Scatter Plots (a) Before a Guided Pareto Sampler Evolution with Guiding Points Marked by Black Circle and (b) Many Generations Later**



A more precise visualization of the Pareto optimal solutions for this nonlinear mass-spring-damper system is shown in Figure 12. The color contour has been set to the decision variable,  $m$ , the discrete system mass. As shown, the discreteness of a single decision creates observable gaps in the behavior of the non-dominated solution set. The “stair-step” pattern can be considered the superposition of Pareto frontiers for each respective value of  $m$  on the same plot. Since the discrete decision  $m$  highly influences the mechanics of the system, one might expect to observe correlated discreteness in the solution set.

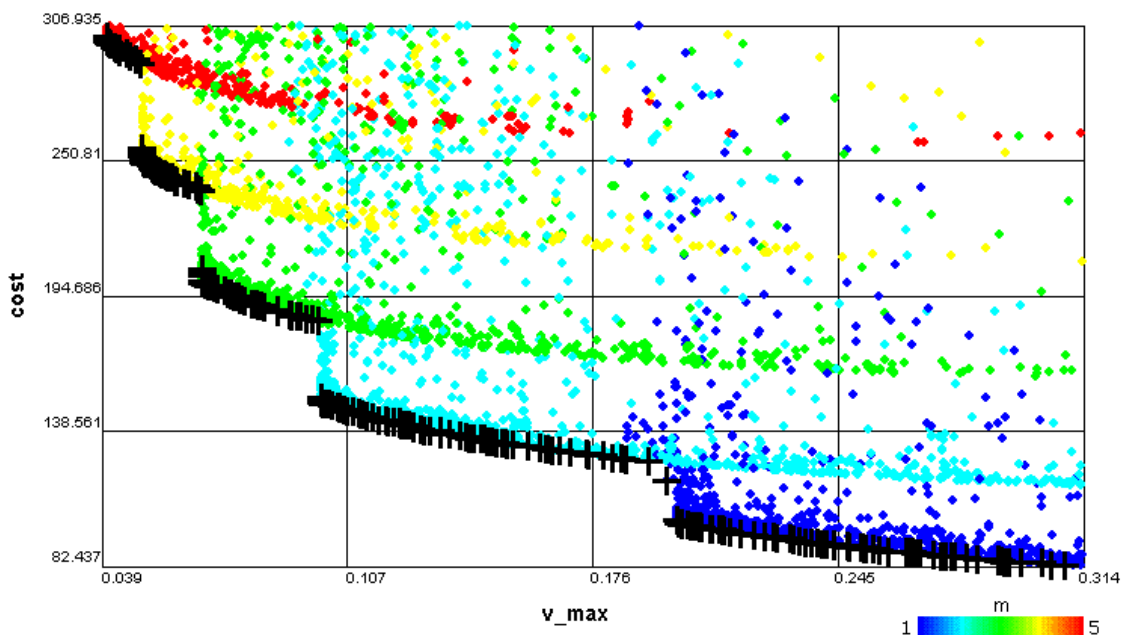


**Figure 12: Scatter Plot Showing Close-up of Non-Continuous Pareto Frontier Caused by Discrete Decision  $m$**

## 3.2 Two-Burn Impulsive Spacecraft Maneuvers

The two-burn impulsive orbital spacecraft maneuver test problem discussed in this section explores the capabilities of ATSV when using static datasets. The visualization of solutions and the location of the Pareto solution set is accomplished without linking ATSV to the problem model.

### 3.2.1 Problem Formulation

A spacecraft in orbit can be defined by a set of six orbital elements which describe its orientation in space [20]. The classical orbital elements (semi-major axis  $a$ , eccentricity  $e$ , inclination  $i$ , right ascension of the ascending node  $\Omega$ , argument of periapsis  $\omega$ , and true anomaly  $\theta$ ) describe the size ( $a$ ) and shape ( $e$ ) as well as the orientation ( $i$ ,  $\Omega$ ,  $\omega$ ) of the orbit. The sixth element ( $\theta$ ) describes the angular position of the spacecraft on the

particular orbit described by the previous five elements. An illustration of these elements is shown in Figure 13.

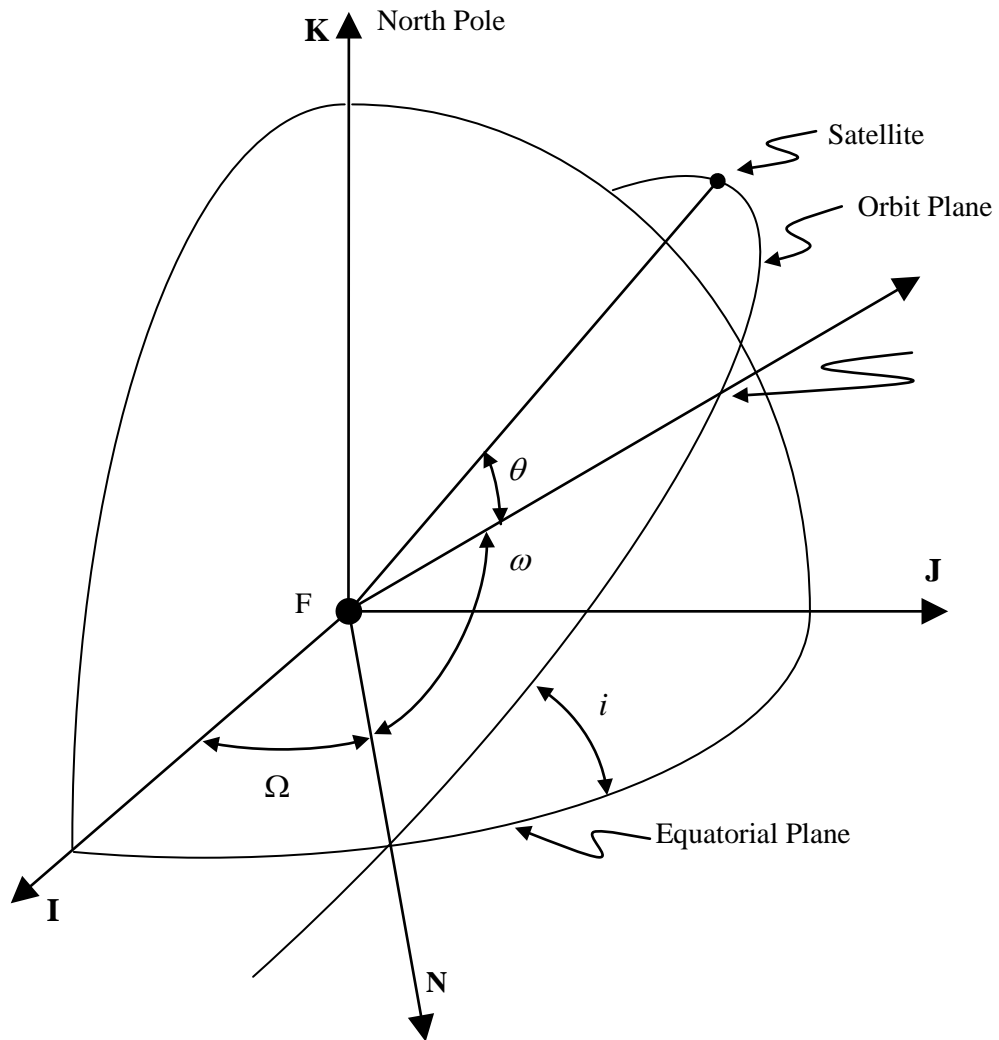


**Figure 13: Illustration of Classical Orbital Elements [20]**

The test problem of interest models an impulsively delivered two-burn plane change spacecraft maneuver from an initial circular orbit to a higher altitude circular orbit. The impulsive changes in velocities ( $\Delta V$ 's) are constrained to be delivered at the nodal crossings (see Figure 14 points A and B) to prevent alteration of the right ascension of the ascending node. A graphical illustration of this two-burn transfer is shown in Figure 14.

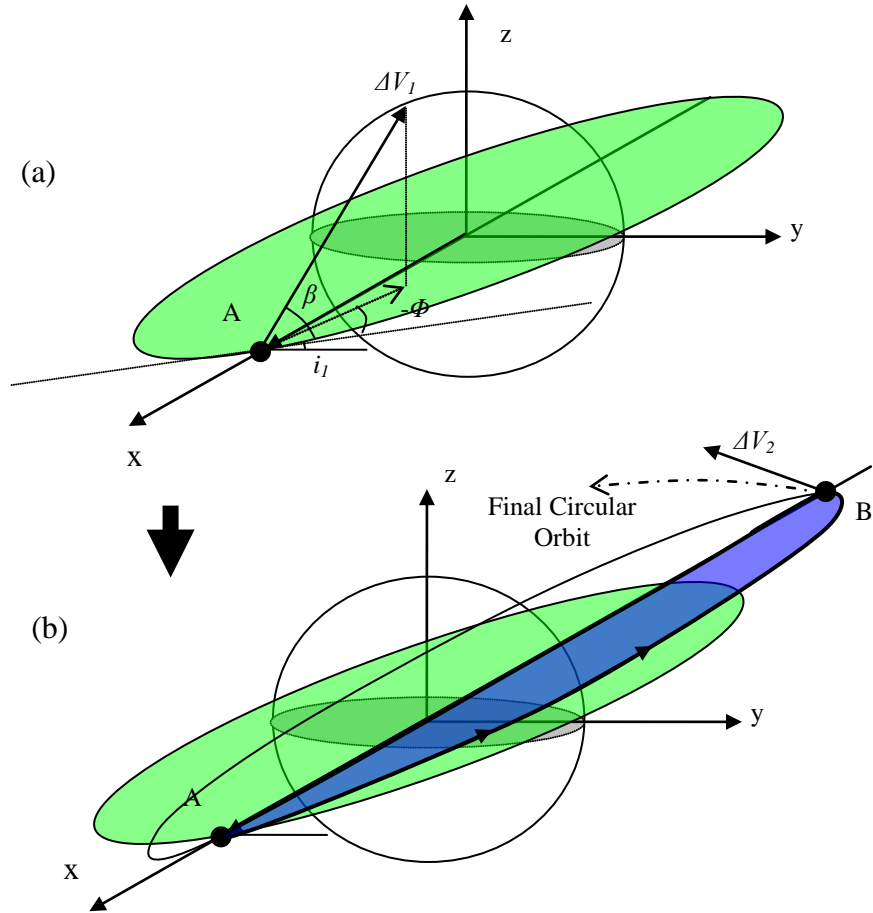


**Figure 14: Graphical Illustration of Two-Burn Transfer**

The green orbit is the initial circular orbit at inclination  $i_1$  shown in Figure 14(a) and (b), the blue orbit is the arc traced by the transfer ellipse at inclination  $i_t$ , and the dotted line represents the direction of the final circular orbit at inclination  $i_2$ .  $\Delta V_1$  is the impulsively-delivered velocity change at the first nodal crossing, and it is delivered at a flight path angle of  $\Phi$  with respect to the orbit tangential direction, and an out-of-plane angle  $\beta$  as shown in Figure 15 and Figure 14(a), where  $x'$ - $y'$  is the plane of the initial circular orbit. The problem decisions and objectives with corresponding ranges and preferences are summarized in Table 2.

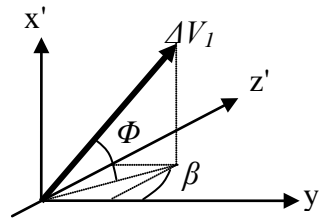


**Figure 15: Illustration of Flight Path Angle  $\Phi$  and Out-of-Plane Angle  $\beta$ .**

**Table 2: Impulsive Orbital Problem Decision Variables and Objectives with Respective Ranges/Preferences**

<b>Decision Variables</b>	<b>Range</b>
$\Delta V_1$	$\Delta V_1 > 0$
Out-of-plane angle, $\beta$	$-90^\circ < \beta < -90^\circ$
Flight path angle, $\Phi$	$-45^\circ < \Phi < 45^\circ$
<b>Objectives</b>	<b>Preference</b>
$\Delta V_{Total}$	Minimize
Time of Flight	Minimize
Final Orbital Radius $r_2$	Maximize
Practical	Discrete Boolean

Note that only outputs of critical design criteria are listed in Table 2. All relevant variables generated in the model are included in the dataset.

The MATLAB code algorithm developed for this example is shown as a flow chart in Figure 16. First, the inclination ( $i_1$ ) and altitude of the initial circular orbit are specified. Then, the essential orbital elements are calculated for this initial orbit. Next, the code randomly varies  $\Delta V_1$ ,  $\Phi$ , and  $\beta$  between the ranges specified in Table 2, and the resulting characteristics regarding the transfer and final orbits are obtained. This information, including objective functions  $\Delta V_{Total}$ , time of flight, and final orbital radius, is calculated by solving Lambert’s problem using Lagrange coefficients [20].

Each orbit trio is evaluated for practicality based on the rotation of the orbit planes between the initial, transfer, and final orbits. If the transfer orbit has an inclination that is not between the inclination of the initial and final orbits, the solution is considered impractical. Though these solutions are feasible, they represent all orbit trios aligned with a “one step backward, two steps forward” approach. Once the program has looped through all population members, all objectives of interest are written to a comma-delimited (.csv) spreadsheet file.

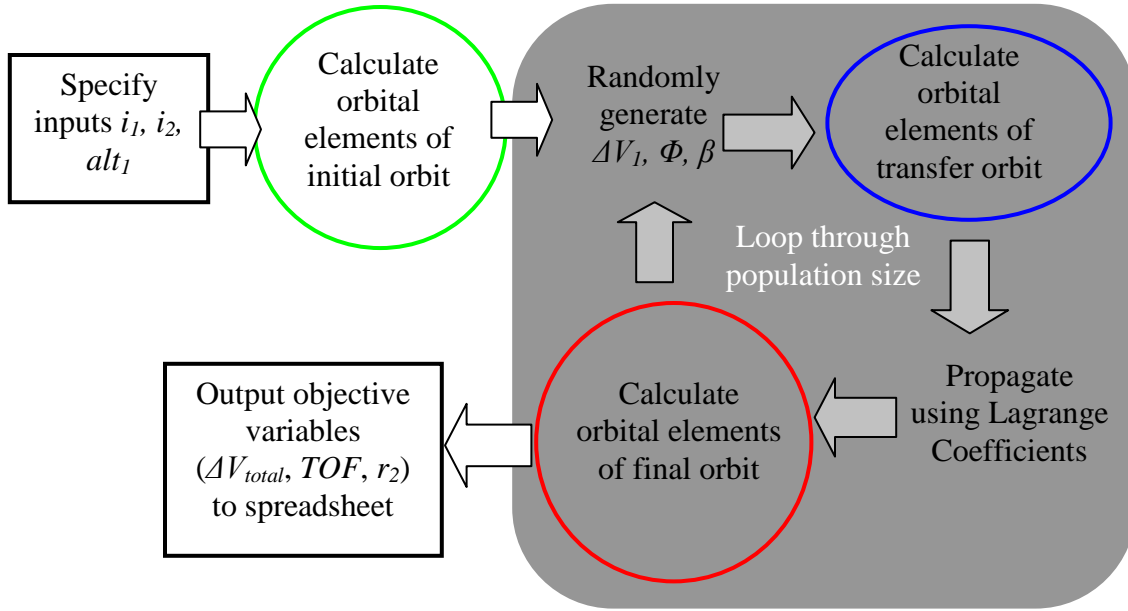


**Figure 16: Flowchart Depicting the Algorithm of the MATLAB Code**

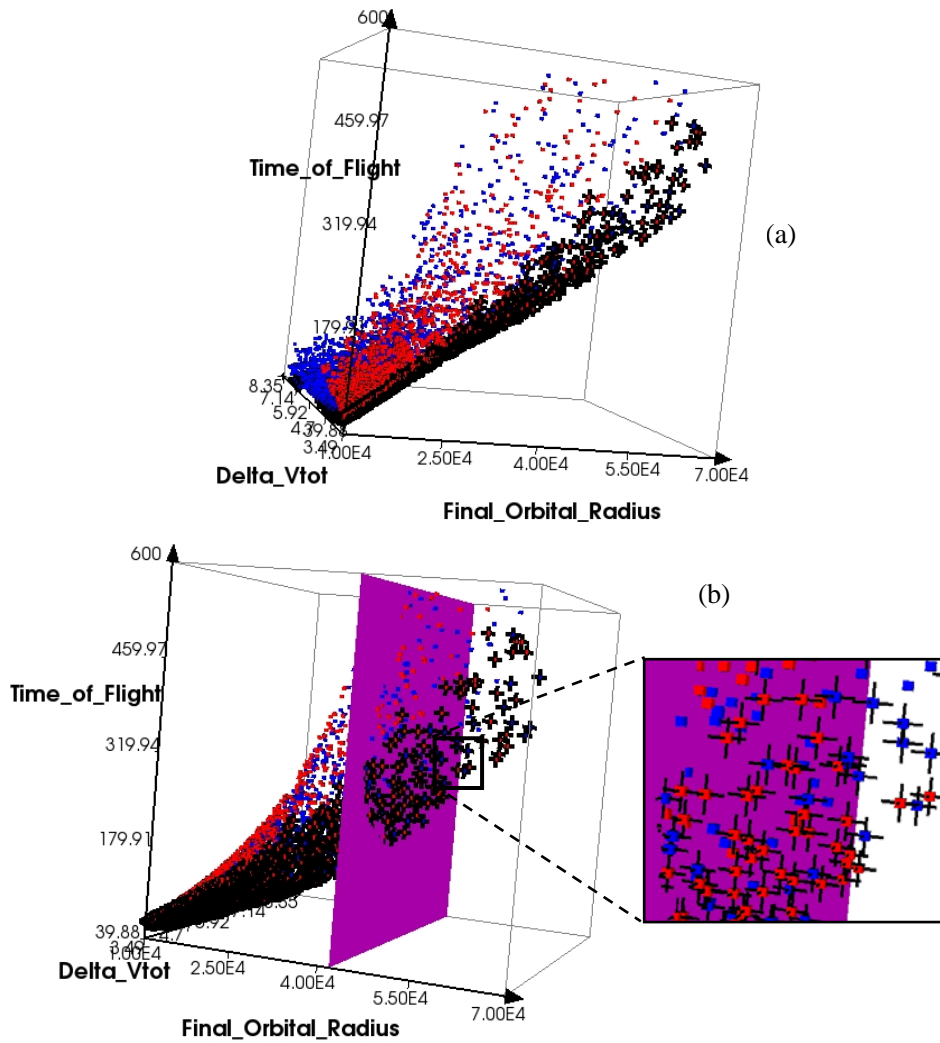
Common initial orbital parameters were chosen for the solutions generated in this work, as listed in Table 3. The initial inclination  $i_1$ , initial circular orbit altitude, and final inclination  $i_2$ , were chosen to represent an orbital transfer from 28.5°, 500 km low-Earth orbit (LEO) to equatorial geosynchronous Earth orbit (GEO).

**Table 3: Initial and Desired Final Orbit Characteristics**

Initial altitude	LEO 500 km
Initial inclination $i_1$	28.5°
Final altitude	GEO 35,786 km
Final inclination $i_2$	0°

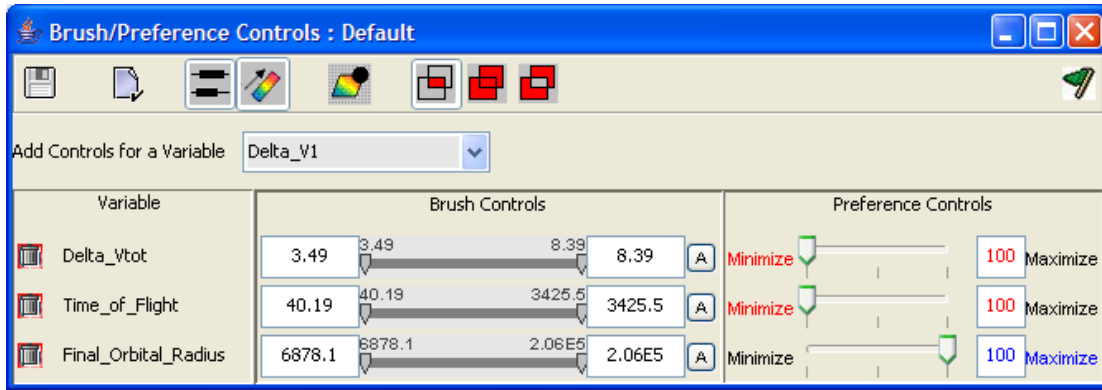
### 3.2.2 Results

Using the MATLAB code as described by Figure 16, a static dataset consisting of 10,000 members is generated for the orbital transfer problem specified in Table 3. Plotting the three objective functions of interest ( $\Delta V_{Total}$ , time of flight, and final orbital radius) on each of the spatial axes creates a three-dimensional envelope, as shown in Figure 17. Figure 17(b) shows an iso-surface at a final orbital radius corresponding to the final desired altitude of 35,786 km. This plane shows the region of interest to be further explored in ATSV.



**Figure 17: (a) Static Dataset Consisting of 10,000 Members. (b) Isosurface Showing Plane of Interest Near GEO Altitude and Pareto Solutions**

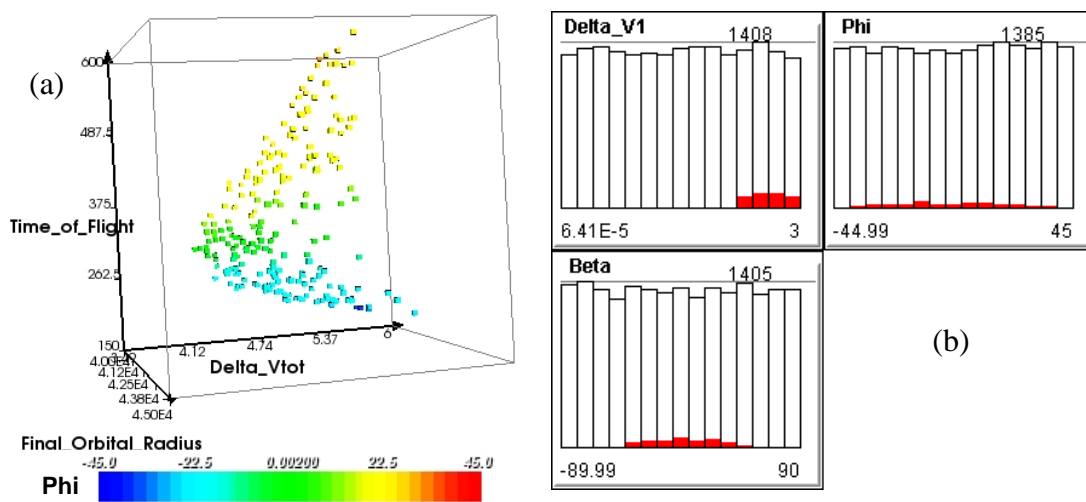
The red and blue points are solutions that are practical and impractical, respectively, based on the aforementioned criteria. The solutions marked with a black + symbol represent the Pareto solutions as specified by the preferences shown in the Preference/Brush Control Window in Figure 18. These settings aim to highlight solutions that simultaneously minimize  $\Delta V_{Total}$  and time of flight while maximizing the radius of the final circular orbit.



**Figure 18: Brush/Preference Controls Window for Orbital Problem Solution Set**

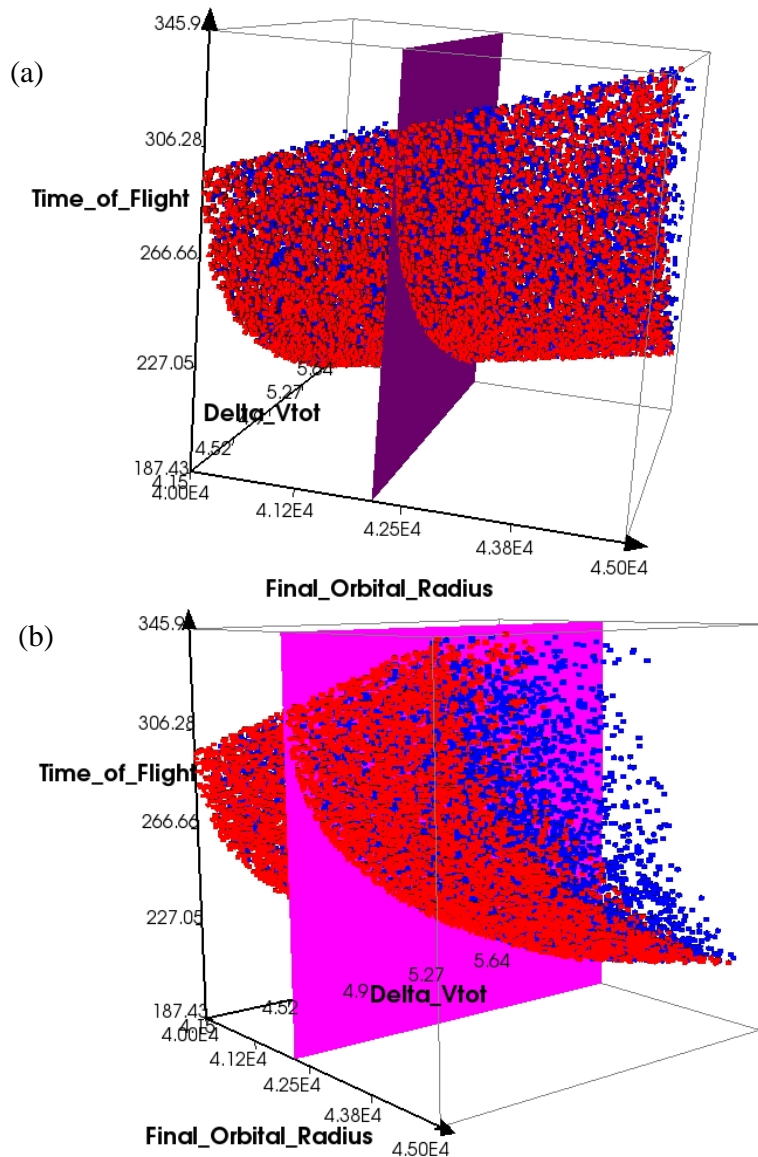
The static dataset shown in Figure 17 has been brushed to exclude all points that have a final orbital radius outside the region of interest, nominally specified to be between a final orbital radius of 40,000 km and 45,000 km. The resulting dataset is shown in Figure 19(a).

Figure 19(b) shows the problem input distribution for the first impulsive maneuver as an ATSV histogram. The white bars show the total distribution of each input (approximately uniform), and the red bars show the distribution of inputs for the brushed dataset. Essentially, any bins without red represent inputs that create solutions far away from the area of interest. Proceeding logically, the range of inputs should be reduced by the user to increase the likelihood of generating solutions within the region of interest. From visual inspection of the histograms, reducing inputs to larger values of  $\Delta V_I$  would be most effective. Also, as shown in the color contour in Figure 19(a), non-positive values of  $\Phi$  create solutions along the Pareto frontier that minimize  $\Delta V_{Total}$  and flight time.



**Figure 19: (a) Static Dataset Brushed to Final Orbital Radius Between 40,000 and 45,000 km. (b) Histogram plot of Inputs Brushed in the Same Manner**

By changing the random distribution of  $\Delta V_1$  from [0, 3.0] km/s to [2.0, 3.0] km/s and  $\Phi$  from  $[-45^\circ, 45^\circ]$  to  $[-45^\circ, 0]$  in the model, a population of 10,000 solutions generates approximately 500 new points in the region of interest. By generating static datasets, brushing to the region of interest, and exporting visible designs, the solutions in the region of interest are stored in a separate file. Just a few iterations of this technique result in the concatenation of all these region specific points shown in Figure 20(a) and (b).



**Figure 20: (a) and (b) Two Perspectives of Densely Populated Region of Interest with Iso-surface at GEO Altitude**

With a more densely populated region of interest, trends in the dataset can be more easily interpreted. As shown in Figure 20, the three-dimensional envelope formed by the



practical (red) points seems to be representable by a continuous Pareto surface. Because of the specific physics which describe the model, this apparent continuity leads to the conclusion that this problem may be suited for visualization through static datasets. In other words, the nature of the problem results in easily acquired Pareto solutions through random sampling, and no “gaps” exist near the Pareto frontier that must be filled.

Using ATSV’s scatter matrix plot, one can easily view trends between variables of interest. A scatter matrix, brushed to  $\pm 50$  km from the target GEO altitude, is shown in Figure 21. Once again, gray points represent “brushed out” points, and red and blue points are the practical and impractical solutions respectively which fall within this criterion. Because of this  $\pm 50$  km brushing, the trends that follow can be considered specific to the LEO to GEO problem parameters listed in Table 3. Though not all points fall precisely on the plane formed by the geostationary altitude, these solutions are considered in the neighborhood and would undoubtedly be subject to orbital fine tuning and phasing, but this is beyond the scope of this demonstration.

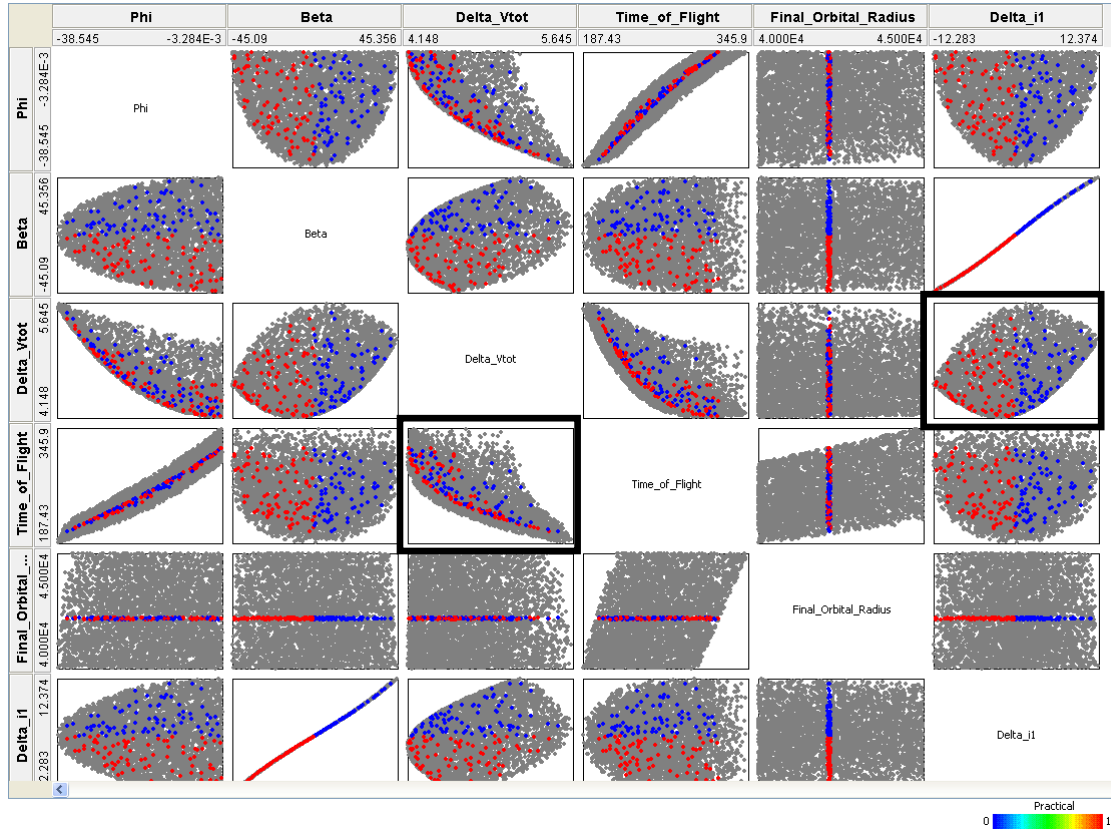


**Figure 21: Scatter Matrix Plot of Variables of Interest**

The two highlighted scatter plots, time of flight vs.  $\Delta V_{Total}$ , and  $\Delta V_{Total}$  vs.  $\Delta i_1$  are of particular interest. These plots are enlarged and shown in Figure 22 and Figure 23 respectively. The trend of the Pareto frontier in Figure 22 shows an inverse relationship between time of flight and  $\Delta V_{Total}$ . Furthermore, it resembles the expected solution for a

two-dimensional version of this problem with no plane change (from Lambert's problem) [20]. Intuitively, the trend's shape remains similar for different desired final orbit sizes.

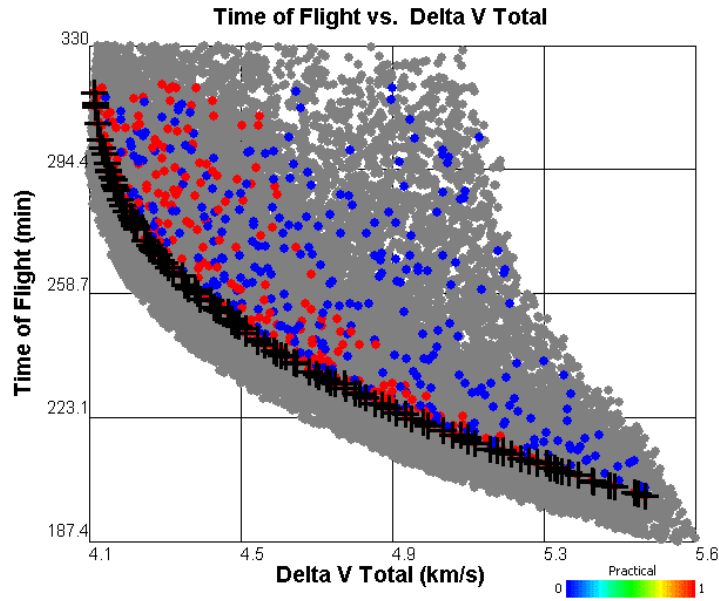


**Figure 22: Solution Set and Pareto Frontier for Time of Flight vs. Total Impulsive Velocity Change ( $\pm 50$  km Brush)**

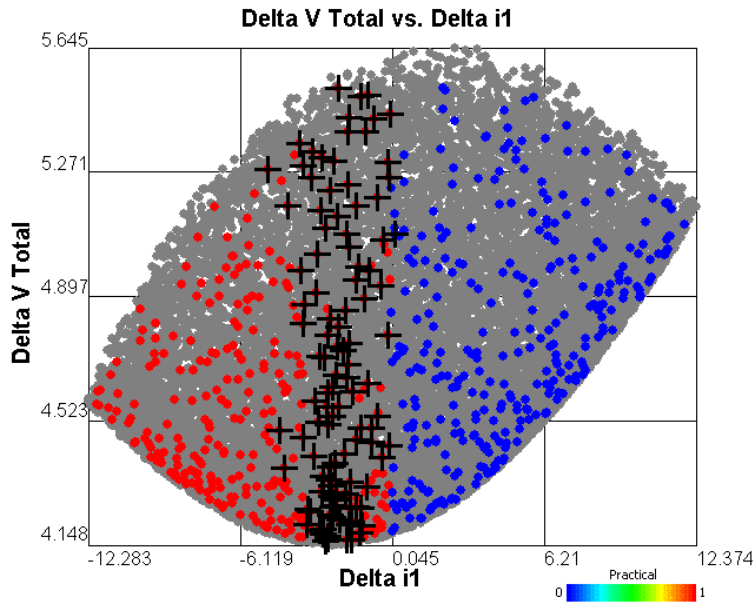


**Figure 23: Total Impulsive Velocity Change vs. Inclination Change from First Burn ( $\pm 50$  km Brush)**

Figure 23 shows  $\Delta V_{Total}$  vs. the change in inclination after the first impulsive maneuver ( $\Delta i_1$ ). Because of the nature of this specific plane change as well as the manner in which

angle  $\beta$  is defined, solutions must have a negative  $\Delta i_1$  value to be considered practical. As orbital dynamics theory suggests, the optimal (Pareto) plane change transfers shown here are solutions that impulsively deliver the most inclination change during the second burn (at a lower orbital velocity). Consequently, the optimal solutions have small  $\Delta i_1$ 's, shown in Figure 23 to be within a range of  $0^\circ$  to  $5^\circ$ .

The Pareto design that most effectively minimizes  $\Delta V_{Total}$  has the design attributes listed in Table 4.

**Table 4: Attributes of Solution with Minimum  $\Delta V_{Total}$**

$\Delta V_1$	2.403 km/s
Out-of-plane angle, $\beta$	$-11.05^\circ$
Flight path angle, $\Phi$	$-0.3776^\circ$
$\Delta V_{Total}$	4.1625 km/s
Time of Flight	316.41 min
Final Orbital Altitude	35,740 km
$\Delta i_1$	$-2.645^\circ$

Vallado [20] explored a similar three-dimensional two-burn plane change orbital mechanics problem. The  $\Delta i_1$  and  $\Delta i_2$  which lead to the lowest  $\Delta V_{Total}$  can be solved for iteratively in what Vallado labels the “minimum combined plane change” algorithm:

$$\sin(s\Delta i) = \frac{\Delta V_1 V_{final} V_{transfer,b} \sin((1-s)\Delta i)}{\Delta V_2 V_{initial} V_{transfer,a}} \quad (5)$$

where  $V_{initial}$  and  $V_{final}$  are the initial and final circular orbital speeds respectively,  $V_{transfer,a}$  and  $V_{transfer,b}$  are the speeds at points A and B respectively, as shown in Figure 14, and  $s$  is a scaling factor that represents the percentage of the total inclination change which is delivered on the first burn:

$$\Delta i_1 = s\Delta i \text{ and } \Delta i_2 = (1-s)\Delta i \quad (6)$$

Solving the equation iteratively yields an optimal  $s$ , which results in the optimal distribution of plane change between the initial and final maneuvers. For the initial and final orbit characteristics listed in Table 3, this algorithm yields the optimal transfer parameters listed in Table 5.

**Table 5: Comparison between ATSV Results and Minimum Combined Plane Change Algorithm**

<b>Parameter</b>	<b>ATSV</b>	<b>Vallado Algorithm [20]</b>	<b>% Difference</b>
$\Delta V_{Total}$	4.1625 km/s	4.1620 km/s	0.01%*
<i>Final Orbital Altitude</i>	35,740 km	35,786 km	0.13%
$\Delta i_1$	2.645°	2.262°	14.5%
$\Delta i_2$	25.855°	26.238°	-
* Negligible within uncertainty			

As shown in the last column of Table 5, the percent difference between the ATSV results and the minimum combined plane change algorithm results is small. The total impulsive velocity change is the same within the uncertainty of the algorithm calculation. The algorithm yields an optimal initial plane change of 2.645° which is 14.5% higher than what ATSV found. However, since ATSV did not locate a solution precisely at geostationary altitude, the comparison to the iterative algorithm serves more as a verification of the data and less as an optimality criterion.

The application of ATSV to the two-burn impulsive orbital spacecraft maneuver test problem discussed in this section permitted the visualization of trade-offs between time of flight and total required velocity change using only static datasets. The minimum impulsive velocity change solution found when using ATSV was comparable to a known optimal solution. The next chapter focuses on continuous-thrust orbital maneuvers which require integration of nonlinear equations of motion. Furthermore, this problem formulation is explored in ATSV using dynamic datasets and the guided Pareto sampler is used to search for optimal trajectories.

## Chapter 4: Continuous-Thrust Orbital Maneuvers

### 4.1 Introduction

This chapter explores the application of ATSV to continuous-thrust orbital maneuvers. Both constant thrust and constant acceleration transfers are explored with both continuous and discrete design variables. Section 4.2 briefly covers relevant previous work and Section 4.3 explores the specifics regarding the constant acceleration and constant thrust problem formulations. Section 4.4 describes the orbit transfer of interest and Section 4.5 discusses the results of each problem formulation and a constant thrust sensitivity study.

### 4.2 Previous Work

The first to explore optimizing low-thrust trajectories using the variation of parameter equations to model orbital perturbations with equinoctial elements as well as adjoint variables was Edelbaum, Sackett, and Malchow in 1973 [21]. Due to the limited computing power at that time, averaging of the state and adjoint equations of motion was employed to allow reasonable computation time. Kechichian solved the same problem using precision-integration of the equations of motion and compared the results to Edelbaum's averaging technique; the accuracy differences between the two techniques were significant [22]. In his work, the initial adjoint variables were optimized using an iterative scheme based on a general descent method, where the aim was to optimize an objective function consisting of a weighted sum of the differences between actual and desired orbital properties. The result was an optimized set of initial adjoint variables that corresponded to the minimum-time minimum-fuel trajectory from low-Earth orbit to geostationary-Earth orbit, as shown in Table 6.

**Table 6: Optimal Initial Adjoint Variables for LEO to GEO Transfer Found by Kechichian [22]**

Adjoint Variable	Initial Value
$\lambda_{a,o}$	1.260484756 sec/km
$\lambda_{h,o}$	386.5626962 sec
$\lambda_{k,o}$	-9388.262635 sec
$\lambda_{p,o}$	-2277.132367 sec
$\lambda_{q,o}$	-17430.27218 sec
$\lambda_{L,o}$	515.5487187 sec/rad
$H$	1.002694
$TOF$	58624.094 s

More recently, the problem has been revisited by Igarashi in the attempt to search specific bounds ( $\pm 5\%$ ,  $\pm 10\%$ ,  $\pm 20\%$ ) on the set of known optimal initial adjoint variables

using a variety of evolutionary algorithms [23]. The results found in Igarashi's work closely matched those found by Kechichian.

The goal of the work described in this chapter is to revisit this problem once again using an evolutionary algorithm, specifically Differential Evolution, which has been integrated into ATSV. The bounds on the known optimal initial adjoint variables are extended beyond what was explored by Igarashi in an attempt to find other optimal or near-optimal solutions. Furthermore, the constant thrust-acceleration problem formulation, which was used by all referenced papers in this section, is altered to model a similar but distinct constant thrust problem, which allows the integration of a hardware-side discrete design variable, engine specific impulse. Also, qualitative and quantitative observations will be made on the effectiveness of the integration of the user/designer into the real-time visualization and multi-objective optimization elements of ATSV.

### 4.3 Problem Formulation

Because of the manner in which the classical orbital elements are defined (see Section 3.2.1 for details), singularities arise in the equations of motion when certain elements are undefined. For example, the right ascension of the ascending node  $\Omega$  is defined as the angle between  $\hat{i}$  and the node vector  $\vec{n}$ . For equatorial orbits ( $i = 0^\circ, 180^\circ$ ) the ascending node vector  $\vec{n}$  does not exist; therefore  $\Omega$  is undefined. Similar singularities arise for circular orbits where eccentricity  $\vec{e}$  has no direction.

In order to avoid the singularities associated with the classical orbital elements for circular and/or non-inclined orbits, equinoctial orbital elements ( $a, h, k, p, q, L$ ) are used in the equations of motion [24]. The simple transformation, shown below, eliminates all singularities except for the retrograde orbit with  $i = 180^\circ$ .

<i>Classical to Equinoctial</i>	<i>Equinoctial to Classical</i>	
$a = a$	$a = a$	
$h = e \sin(\omega + \Omega)$	$e = (h^2 + k^2)^{1/2}$	
$k = e \cos(\omega + \Omega)$	$i = 2 \tan^{-1} \left( \sqrt{p^2 + q^2} \right)$	
$p = \tan(i/2) \sin(\Omega)$	$\Omega = \tan^{-1}(p/q)$	(7)
$q = \tan(i/2) \cos(\Omega)$	$\omega = \tan^{-1}(h/k) - \tan^{-1}(p/q)$	
$L = \theta + \omega + \Omega$	$\theta = L - \tan^{-1}(h/k)$	

#### 4.3.1 Constant Acceleration

Edelbaum, et al. [21], using the calculus of variations, developed the equations of motion describing how a spacecraft's orbit's equinoctial elements change with time due to an applied thrust. A set of these equations, modified by Kechichian [22], are shown as

$$\dot{\vec{x}}_e = f_t[M] \vec{u} + n \vec{e}_L \quad (8)$$

$$\dot{\bar{\lambda}} = \frac{\partial H}{\partial \dot{\bar{x}}_e} = -\bar{\lambda}^T \frac{\partial [M]}{\partial \bar{x}_e} \bar{u} f_t - \lambda_L \frac{\partial n}{\partial \bar{x}_e} \quad (9)$$

The equinoctial element state vector  $\bar{x}_e$  and its derivative  $\dot{\bar{x}}_e$ , as well as the adjoint variable state vector (Lagrange multiplier)  $\bar{\lambda}$  and its derivative  $\dot{\bar{\lambda}}$  are respectively defined as

$$\bar{x}_e = \begin{bmatrix} a \\ h \\ k \\ p \\ q \\ L \end{bmatrix} \quad \dot{\bar{x}}_e = \begin{bmatrix} \dot{a} \\ \dot{h} \\ \dot{k} \\ \dot{p} \\ \dot{q} \\ \dot{L} \end{bmatrix} \quad \bar{\lambda} = \begin{bmatrix} \lambda_a \\ \lambda_h \\ \lambda_k \\ \lambda_p \\ \lambda_q \\ \lambda_L \end{bmatrix} \quad \dot{\bar{\lambda}} = \begin{bmatrix} \dot{\lambda}_a \\ \dot{\lambda}_h \\ \dot{\lambda}_k \\ \dot{\lambda}_p \\ \dot{\lambda}_q \\ \dot{\lambda}_L \end{bmatrix} \quad (10)$$

The matrix  $[M]$  is a  $6 \times 3$  matrix containing expressions involving partial derivatives of each state element in  $\bar{x}_e$ ; further information regarding the definition of  $[M]$  can be found in Appendix B and Appendix C. The vector  $\bar{u}$  is a unit vector pointing in the thrust direction,

$$\bar{u} = \frac{[M]^T \bar{\lambda}}{\|[M]^T \bar{\lambda}\|} \text{ where } \begin{bmatrix} u_f = \cos \alpha \cos \beta \\ u_g = \sin \alpha \cos \beta \\ u_w = \sin \beta \end{bmatrix} \quad (11)$$

The angles  $\alpha$  and  $\beta$  are yaw (in plane) and pitch (out-of-plane) angles respectively, and  $f_t$  is the constant applied acceleration. The mean motion  $n$  is given by  $n = (\mu/a^3)^{1/2}$  where  $\mu$  is the gravitational parameter. The scalar Hamiltonian for this system is defined as

$$H = \bar{\lambda}^T [M] \bar{u} f_t + \lambda_L \bar{e}_L \quad (12)$$

where  $\bar{e}_L = [0 \ 0 \ 0 \ 0 \ 0 \ 1]^T$  and the end condition,  $H = 1.0$ , corresponds to the minimum-time minimum-fuel transfer.

### 4.3.2 Constant Thrust

In order to formulate the problem such that the spacecraft experiences constant thrust instead of constant acceleration, some minor modifications to the equations of motion (Equations (8)-(12)) are made. A seventh state variable, spacecraft mass  $m$ , is added to the state vector  $\bar{x}_e$ , and its adjoint counterpart  $\lambda_m$  is added to the adjoint variable state vector  $\bar{\lambda}$ . The value of  $f_t$  is no longer constant with time and is replaced in Equations (8), (9), and (12) by its definition

$$f_t = \frac{T}{m} \quad (13)$$

This formulation introduces a discrete design variable, engine specific impulse,  $I_{sp}$ . The equations of motion are also modified to include,  $\dot{m}$  and  $\dot{\lambda}_m$ , as defined in Equations (14) and (15). With these modifications, simultaneous integration of Equations (8) and (9) proceeds as specified in Section 4.4.

$$\dot{\lambda}_m = -\| [M]^T \bar{\lambda} \| \frac{T}{m^2} \quad (14)$$

$$\dot{m} = -\frac{T}{I_{sp} g_o} \quad \text{where } g_o = 9.80665 \times 10^{-3} \text{ km/s}^2 \quad (15)$$

#### 4.4 Problem Specification

The orbit transfer between the low-Earth orbit (LEO) specified in Table 7(a) and the geosynchronous orbit (GEO) specified Table 7(b) is the transfer of interest for this work – identical to the transfer explored in References [22] and [23].

**Table 7: (a) Initial LEO “Baseline” Orbit Characteristics and (b) Final GEO Orbit Characteristics**

(a) Initial Low-Earth Orbit				(b) Final Desired Orbit	
Classical		Equinoctial		Classical	
$a_o$	7000 (km)	$a_o$	7000 (km)	$a_{desired}$	42000 (km)
$e_o$	0	$e_o$	0	$e_{desired}$	0.001
$i_o$	28.5°	$i_o$	28.5°	$i_{desired}$	1°
$\Omega_o$	0°	$\Omega_o$	0°	$\Omega_{desired}$	0°
$\omega_o$	0°	$\omega_o$	0°	$\omega_{desired}$	0°
$\theta_o$	-220°	$L_o$	-220°	$\theta_{desired}$	Free

For the constant acceleration problem described in the previous section, the initial conditions of the equinoctial state  $\bar{x}_{e,o}$  are known but the initial conditions of the adjoint variables  $\bar{\lambda}_o$  are unknown. Therefore, the decision space consists of the initial conditions of these six adjoint variables. Given  $\bar{\lambda}_o$  and  $f_i$  ( $f_i = 9.8 \times 10^{-5} \text{ km/s}^2$ ), Equations (8) and (9) are simultaneously integrated using the ODE45 function in MATLAB with relative and absolute tolerances set at  $10^{-8}$ . Integration is set to terminate if the semi-major axis  $a$  reaches  $a_{desired}$ , if inclination increases or semi-major axis decreases within a small tolerance, or if a maximum integration time is achieved as specified by the user. At the termination of integration, the states of interest are the final equinoctial state  $\bar{x}_{e,f}$  and the Hamiltonian  $H$  of the system.

For the constant thrust problem,  $T$  and  $m_o$  are chosen such that the initial acceleration is equal to the applied acceleration used for the constant acceleration problem formulation ( $f_i|_{t=0} = T/m_o = 9.8 \times 10^{-5} \text{ km/s}^2$ ). Also, the decision space has one more decision variable,  $I_{sp}$ . Note that the additional adjoint variable  $\lambda_m$  has no bearing on the integration of the equinoctial state and therefore is not considered a decision variable.

The objectives are to achieve the desired final orbit  $\bar{x}_{e,desired}$  and minimize time of flight via the transversality condition  $H = 1.0$ . This “target oriented” objective is transformed into a “goal oriented” objective by considering the minimization of a weighted sum of absolute differences between the final state and the desired final state, as shown in Equation (16). Note that the weights and the order of terms comprising  $f$  can



significantly affect the ability of a search algorithm to properly converge to an optimal solution. An explanation of how this issue is bypassed using visual steering is covered in Section 4.5.1.

$$f = w_1 |a - a_{desired}| + w_2 |h - h_{desired}| + w_3 |k - k_{desired}| + w_4 |p - p_{desired}| + w_5 |q - q_{desired}| + w_6 |H - 1.0| \quad (16)$$

The Excel interfaces used for the ATSV-Excel-MATLAB system specified in Section 2.3 for the constant acceleration and constant thrust problem formulations are shown in Appendix C and Appendix D respectively. The information in Table 8 summarizes the search specifics and cases explored in three subsections of Results and Discussion.

**Table 8: Summary of Explored Cases for Continuous Thrust Problem Formulations**

<b>Constant Acceleration</b>	
<i>Search Range:</i>	<i>Objective:</i>
±10% of Table 6	Explore decision space immediately surrounding known optimal solution listed in Table 6 over a wider spectrum than Reference [23] and identify other optimal or near optimal solutions, if any, within each search range.
±25% of Table 6	
±50% of Table 6	
±500% of Table 6	
<b>Constant Thrust</b>	
<i>Search Range:</i>	<i>Objective:</i>
Custom based on $I_{sp}$ , on the order of ±500% of Table 6	Identify optimal trajectories for engine $I_{sp}$ values of 3000, 1500, and 600 seconds.
<b>Constant Thrust Sensitivity Study</b>	
<i>Search Range:</i>	<i>Objective:</i>
Custom based on case, on the order of ±500% of Table 6	Find optimal solutions for small perturbations of initial LEO orbit listed in Table 7(a) for $I_{sp}=3000$ sec. Observe sensitivity of decision variables to these perturbations.
<i>Cases:</i>	
$a_o$ : ±100 km, -200 km	
$i_o$ : -1.5°, +1.5°, +3°	
$\Omega_o$ : +45°	

## 4.5 Results

This section discusses the results of the constant acceleration and constant thrust trajectory optimization case studies listed in Table 8. Section 4.5.1 discusses the visual steering commands used to find optimal continuous thrust trajectories. Sections 4.5.2 and 4.5.3 explore optimal solutions for a constant applied acceleration and a constant applied

thrust respectively. Section 4.5.4 examines the sensitivity of optimal constant thrust solutions to perturbations in the initial low-Earth orbit.

### 4.5.1 Optimal Solution Acquisition via Visual Steering

One of the many goals of ATSV is to use an engineer’s intuition and/or knowledge gained from prior experience with a particular engineering problem in order to enhance search. As with any model implementation using ATSV, over the many hours of sampling the design space, the most efficient visual steering commands were constantly refined as problem-specific wisdom was gained. The most effective technique found for this problem formulation can be described by the flow chart in Figure 24.

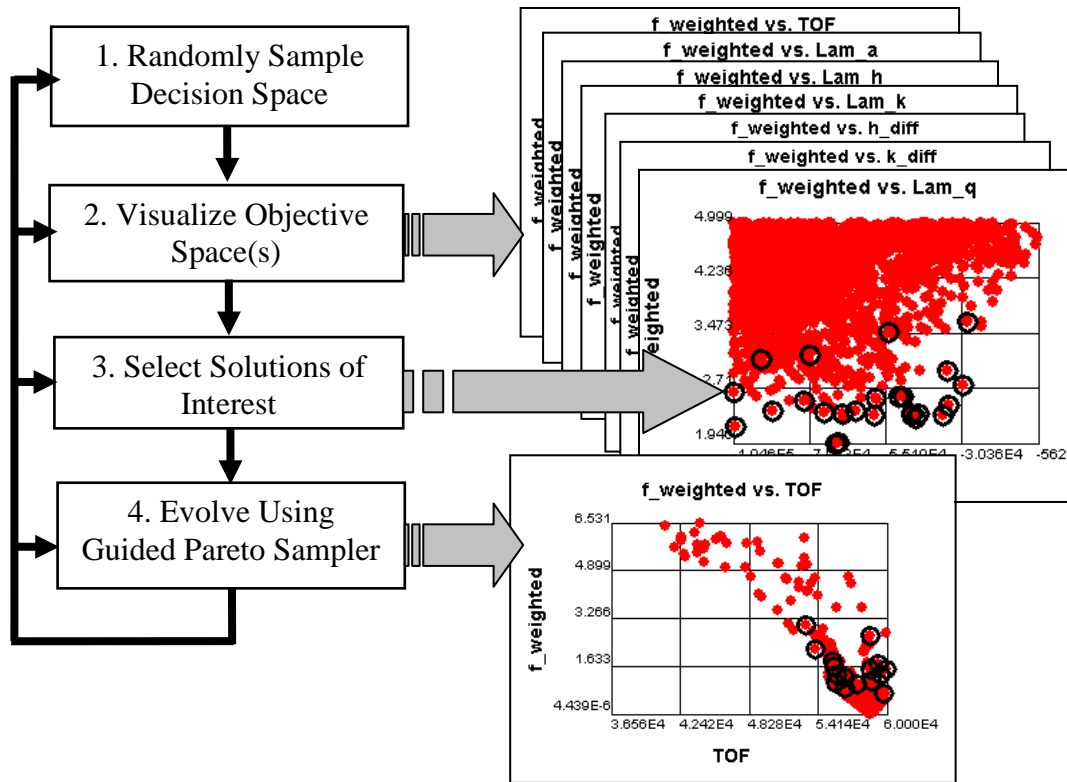
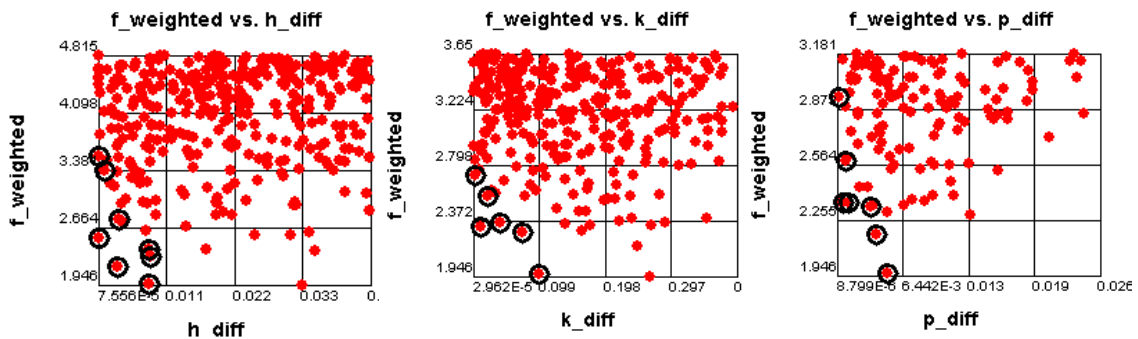


Figure 24: Optimal Solution Acquisition via Visual Steering Flow Chart

First, the decision space is sampled randomly and uniformly anywhere from 100,000 to 1,000,000 times. The objective and decision spaces are then visualized in a variety of combinations using ATSV’s scatter plots. The visualization of  $f$  vs.  $TOF$ ,  $\lambda_{a,o}$ ,  $\lambda_{h,o}$ ,  $\lambda_{k,o}$ ,  $|a - a_{desired}|$ ,  $|h - h_{desired}|$ , etc. reveals promising solutions that exist from the randomly sampled set. Solutions of interest are then selected and the exploration of the design space is driven by the guided Pareto sampler.

The selection of “solutions of interest” is a problem-specific and designer-specific process that can be difficult to quantify because it relies on abstract information such as a designer’s intuition, knowledge, and/or problem-specific wisdom. Generally, solutions that have small  $f$  are chosen to guide evolutions in early iterations of the exploration process.

Because of the size of the decision space, solutions often converge to false optima, meaning the progress of solution evolution will halt with  $f \gg 0$ . Pre-convergence issues may also arise from improper weighting of the terms comprising the definition of  $f$ . If this occurs, some or all of the steps listed in Figure 24 are revisited until  $f$  approaches zero or it is determined that no solution exists within the given decision space range. In order to overcome pre-convergence, a diverse selection of points is chosen to guide the evolution. Generally, a variety of promising solutions are chosen by examining which terms in  $f$  are lagging in the evolution process. An example of promising solution selection using this technique is illustrated in the three scatter plots shown in Figure 25. In this example,  $|h-h_{desired}|$ ,  $|k-k_{desired}|$ , and  $|p-p_{desired}|$  are “lagging” after an evolution has pre-converged, meaning their magnitudes are much greater than the other terms comprising  $f$ . As shown, points are selected that simultaneously minimize  $f$  and these lagging terms to guide the next evolution. By visually steering the trade space with ATSV, optimal solutions are efficiently located without tediously fine-tuning the weights on specific objectives.



**Figure 25: Example Selection of Solutions of Interest used to Guide the Next Evolution**

The guided Pareto sampler’s ability to pause, adjust, and alter an evolution can drastically increase the efficiency of evolutionary search. Figure 26(a)-(f) shows the progression of many guided Pareto searches toward optimality over many iterations of the technique described by Figure 24. Each plot shows  $f$  vs. time of flight, and the solutions chosen to guide a particular evolution are highlighted by black circles. Using this method, the progression toward false optima shown in Figure 26(b) and (d) is easily overcome. With a combination of visualization, evolutionary search, and intuition/knowledge inspired adjustments, the designer is able to visually “steer” solutions toward optimality in order to obtain minimum-time minimum-fuel constant acceleration and constant thrust orbit transfers.

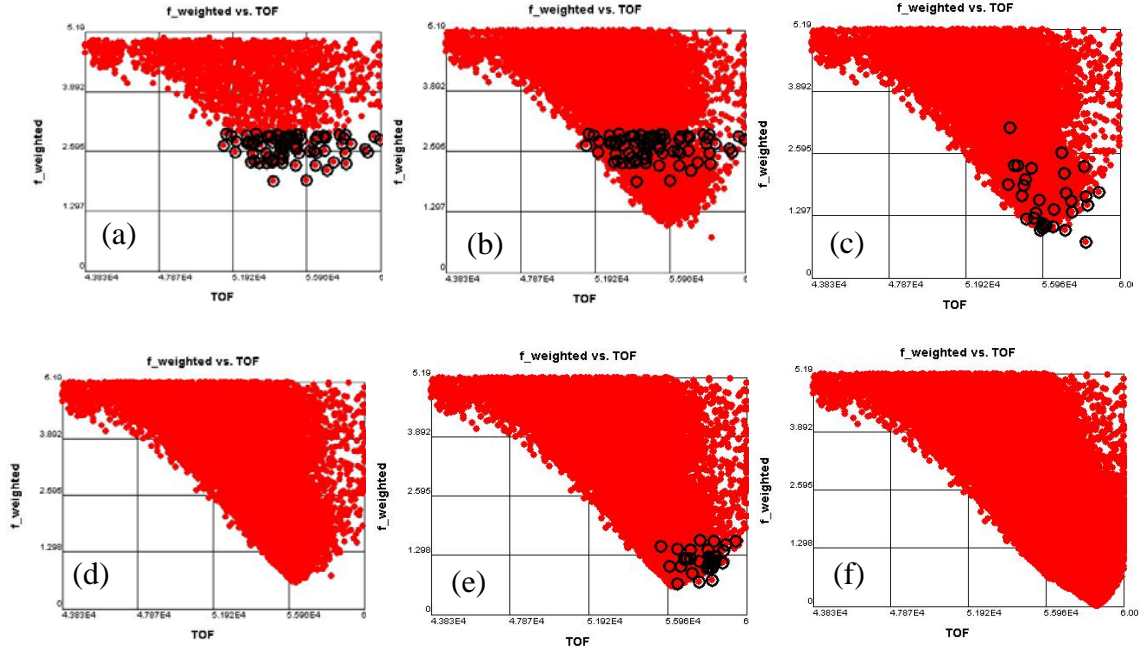


**Figure 26: Progression of a Typical Search Using the Guided Pareto Sampler**

In order to quantify the point at which the minimization of  $f$  is sufficient for optimality, the final state of the solution explored in the next section (listed in Table 10) is shown in Table 9. In general, solutions which have  $f$  on the order of  $1 \times 10^{-5}$  or less are considered optimal, and the values of the final state of the classical elements in this table are a good measure of the accuracy of all optimal solutions presented in this work.

**Table 9: Typical Optimal Final Classical State**

	Goal	Sufficiently Optimal
$a_{desired}$	42000 (km)	42000 (km)
$e_{desired}$	0.001	0.000999677
$i_{desired}$	$1^\circ$	$0.99999726^\circ$
$\Omega_{desired}$	$0^\circ$	$9.76092E-05^\circ$
$\omega_{desired}$	$0^\circ$	$0.010314043^\circ$
$\theta_{desired}$	Free	Free
$H$	1.0	0.999999
$f$	0	$4.44 \times 10^{-6}$

## 4.5.2 Constant Acceleration

Within the decision space search ranges of  $\pm 10\%$ ,  $\pm 25\%$ , and  $\pm 50\%$  of the known optimal solution listed in Table 6, each evolution process converged toward this known solution. For the  $\pm 500\%$  search range, some evolutions converged toward the solution listed in Table 6 and others converged to a solution which the author considers to be clearly distinct. This “near optimal” solution and a comparison with the optimal solution found

in Reference [22] are shown in Table 10. Although only two of the six elements of  $\bar{\lambda}_o$  converge to within 1% of the values listed in Table 6, the time of flight for the near optimal solution is only 0.007% greater. Furthermore, the time history of the classical orbital elements and the thrust vector control angles are almost identical when compared to corresponding time histories for the solution listed in Table 6, as shown in Figure 27, Figure 28, and Figure 29. Moreover, trends of  $a$ ,  $i$ ,  $e$ ,  $\alpha$ , and  $\beta$  with time closely match the time history behavior from References [22] and [23].

The assumption that  $\lambda_{h,o}$  and  $\lambda_{p,o}$  are less sensitive than the other initial adjoint variables to the solution quality may be fair, but the idea that these variables are largely insensitive is not. Upon replacing the value of  $\lambda_{h,o}$  for the optimal set listed in Table 10 with the optimal value from Reference [22], which the author calls  $\lambda_{h,o[22]}$ , solution quality jumps down five orders of magnitude. Similar behavior is evident when applying this test for  $\lambda_{p,o}$ ,  $\lambda_{h,o}$  and  $\lambda_{p,o}$  simultaneously, and various randomly chosen values between  $[\lambda_{p,o} \lambda_{p,o[22]}]$  and  $[\lambda_{h,o} \lambda_{h,o[22]}]$ .

**Table 10: “Near Optimal” Adjoint Variable Initial Conditions for Constant Thrust-Acceleration LEO to GEO Transfer**

$\bar{\lambda}_o$	Optimal Value	% Difference from Reference [22]
$\lambda_{a,o}$ (sec/km)	1.278695	1.445%
$\lambda_{h,o}$ (sec)	590.5856	52.779%
$\lambda_{k,o}$ (sec)	-9333.9	-0.579%
$\lambda_{p,o}$ (sec)	-3397.12	-49.184%
$\lambda_{q,o}$ (sec)	-17526.5	-0.552%
$\lambda_{L,o}$ (sec/rad)	503.6537	2.307%
<i>TOF</i> (sec)	58628.61	0.007%

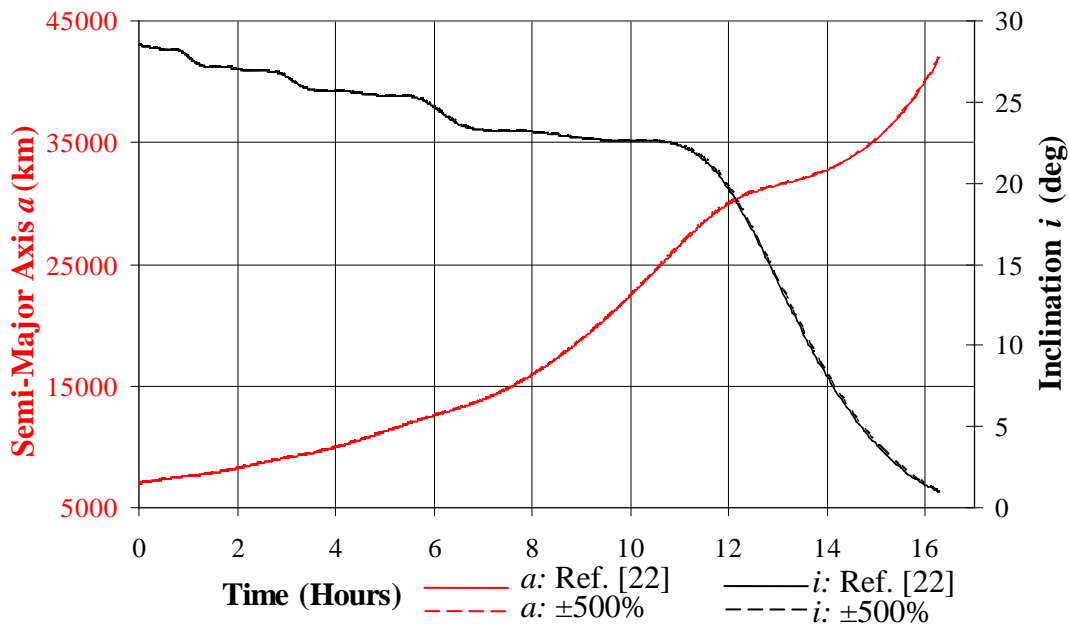


**Figure 27: Semi-Major Axis and Inclination as a Function of Time for Optimal Trajectory found within  $\pm 500\%$  of Reference [22]**

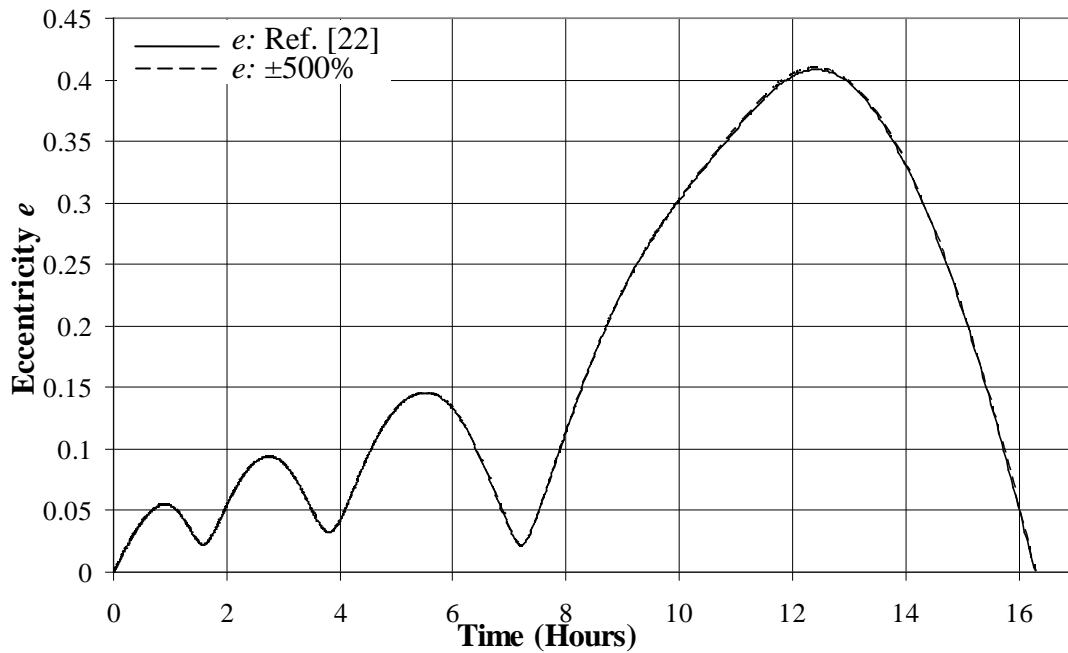


**Figure 28: Eccentricity as a Function of Time for Optimal Trajectory found within  $\pm 500\%$  of Reference [22]**

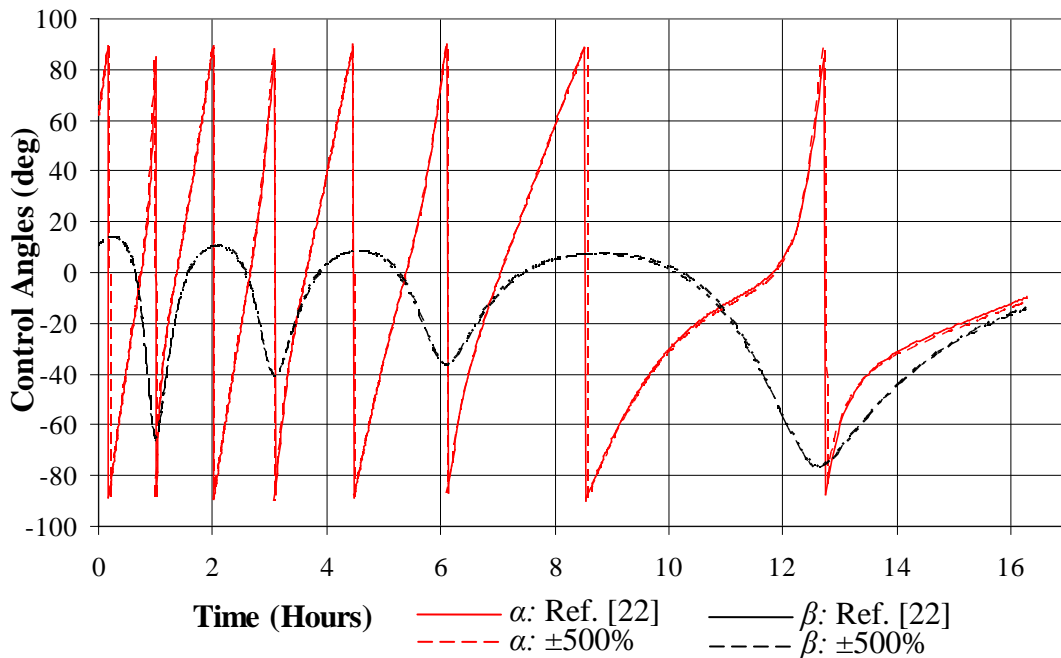


**Figure 29: Yaw  $\alpha$  and Pitch  $\beta$  as a Function of Time for Optimal Trajectory found within  $\pm 500\%$  of Reference [22]**

The existence of a near optimal solution is intriguing and implies that there are multiple distinct sets of adjoint variable initial conditions which lead to nearly the same behavior

of the orbital elements with time. Accordingly, the concept of “optimality” as referred to in this work should be considered near-optimal, and not truly mathematically optimal.

### 4.5.3 Constant Thrust

The goal of the work in this section is to introduce a new design variable, spacecraft specific impulse ( $I_{sp}$ ), by changing the constant acceleration problem formulation to a constant thrust formulation and identify optimal trajectories for three values of  $I_{sp}$  – 3000, 1500, and 600 seconds. These engine specific impulses represent nominal values for ion, Hall, and Arcjet thrusters respectively. Optimal adjoint variable initial conditions for engine specific impulses of 3000 and 1500 seconds are listed with the optimal constant acceleration solution in Table 11.

**Table 11: Optimal Adjoint Variable Initial Conditions for Constant-Thrust LEO to GEO Transfers and Comparison with Constant Acceleration Transfer**

	Constant Acceleration	Constant Thrust	
		$I_{sp} = 3000$ (sec)	$I_{sp} = 1500$ (sec)
$\lambda_{a,o}$ (sec/km)	1.278695	0.69733703	0.34768197
$\lambda_{h,o}$ (sec)	590.5856	533.6483	157.534
$\lambda_{k,o}$ (sec)	-9333.9	-8038.6123	-6918.626
$\lambda_{p,o}$ (sec)	-3397.12	-4434.298	-3290.7383
$\lambda_{q,o}$ (sec)	-17526.5	-11725.732	-7789.5884
$\lambda_{L,o}$ (sec/rad)	503.6537	520.88696	524.09375
$TOF$ (sec)	58628.61	55108.215	51821.383
$f$	$4.44 \times 10^{-6}$	$2.70619 \times 10^{-6}$	$1.30803 \times 10^{-6}$

Corresponding time histories of  $a$ ,  $i$ ,  $e$ ,  $\alpha$ , and  $\beta$  for each solution listed in Table 11 are shown in Figure 30, Figure 31, and Figure 32 respectively. As expected, optimal trajectory time histories of the constant thrust formulations are similar to the optimal time histories of the constant acceleration formulation. These time histories are merely stretched and perturbed between cases in fairly observable patterns. The zoomed view in Figure 30 illustrates the manner in which solutions converge toward local optima for different thrusting magnitudes; near the first hour of flight,  $a(t)$  seems to switch between a constant acceleration “path” and respective constant thrust “paths”. This is certainly a result of the differences between time histories of  $\alpha$  between thrusting magnitudes near the first hour of flight, as shown in the zoomed view in Figure 32.

The inability to locate a solution for  $I_{sp} = 600$  within the specified search range is a direct result of this “switching” behavior. Although the  $I_{sp} = 1500$  solution is slightly sub-optimal by observation, it was found within the set integration behavior tolerance for  $da/dt$ . Our conclusion that the switching behavior of the  $I_{sp} = 600$  solution stops the integration early by tripping the  $da/dt$  tolerance was confirmed by temporarily widening this tolerance. In order to find a suitably optimal solution for  $I_{sp} = 600$ , the search space should be widened.

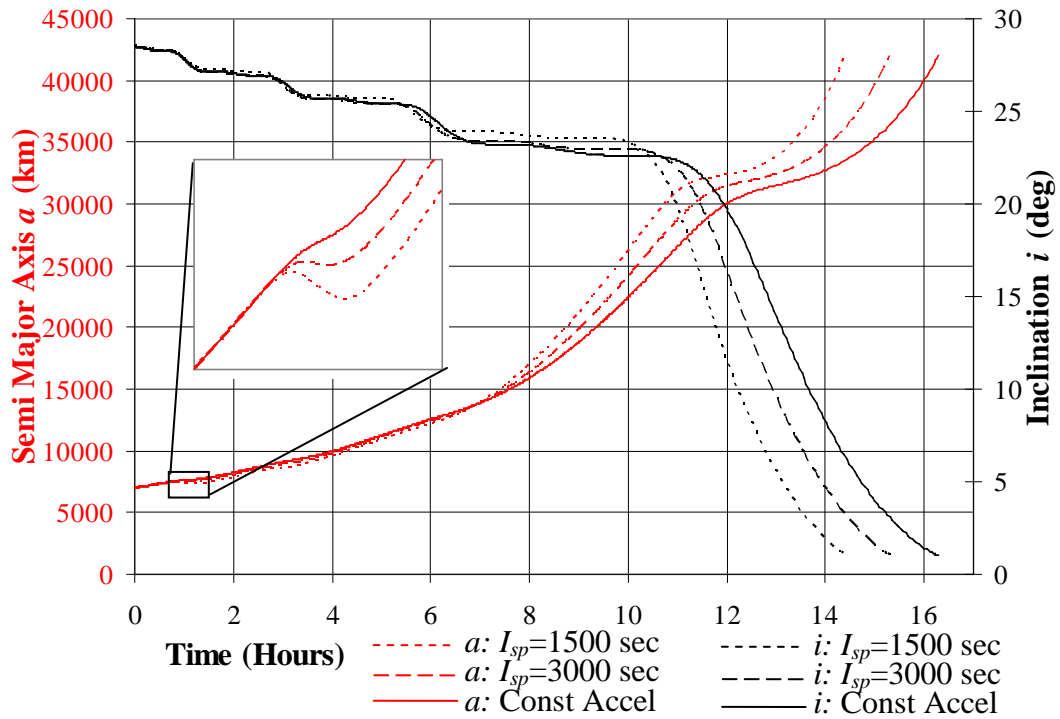


**Figure 30: Semi-Major Axis and Inclination as a Function of Time for Different  $I_{sp}$ 's, Constant Acceleration Case Also Shown**

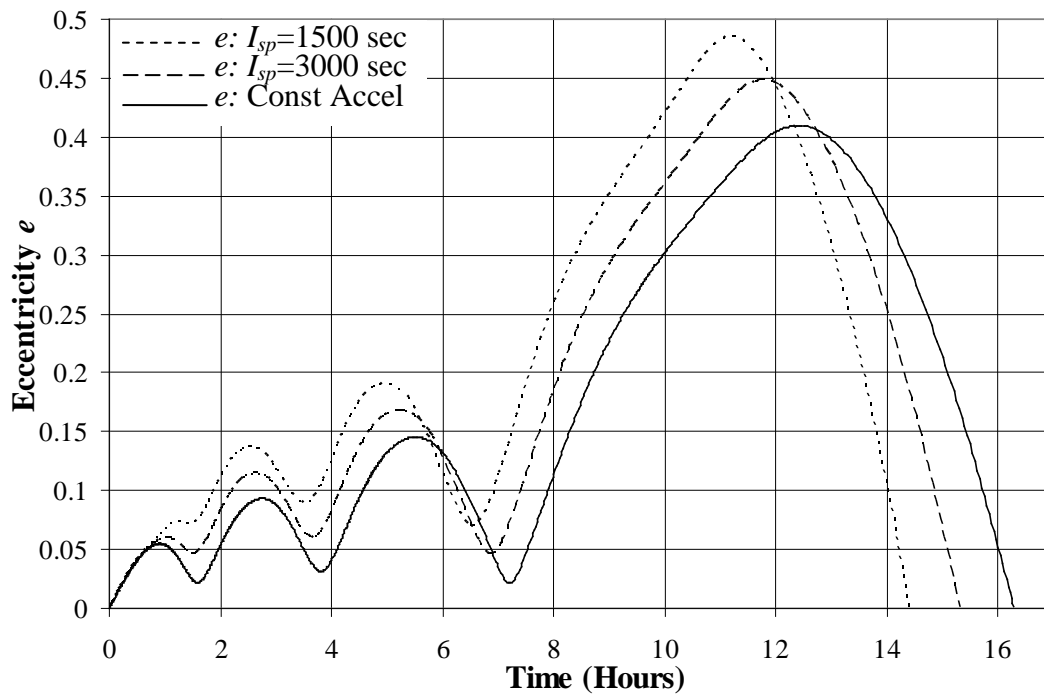


**Figure 31: Eccentricity as a Function of Time for Different  $I_{sp}$ 's, Constant Acceleration Case Also Shown**



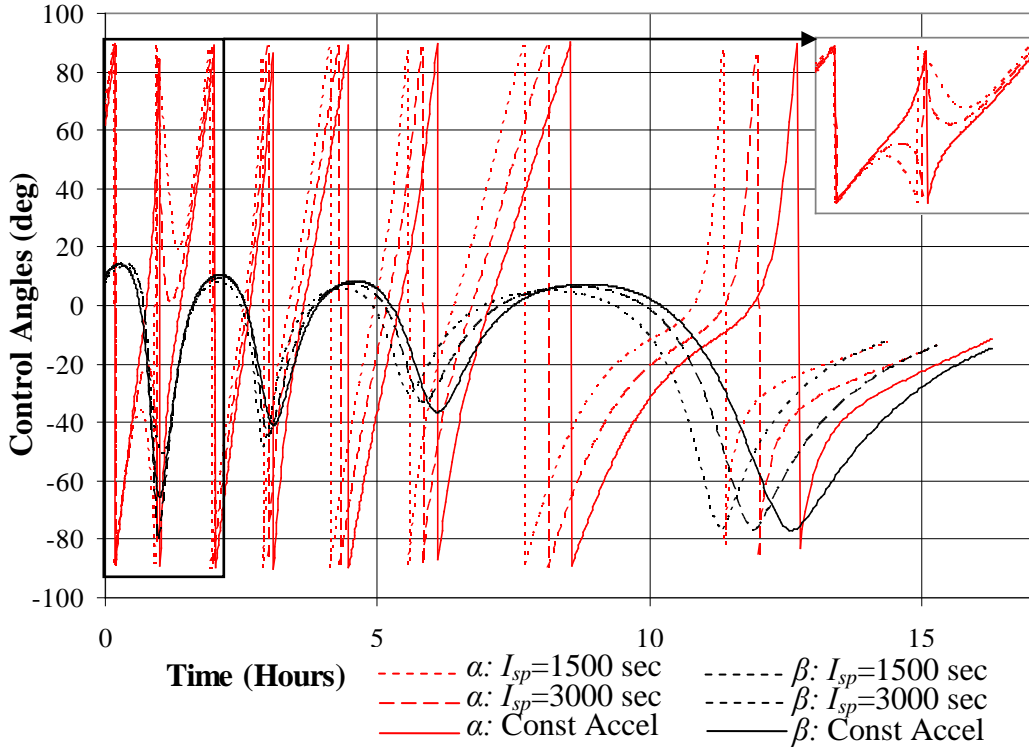


**Figure 32: Yaw  $\alpha$  and Pitch  $\beta$  Angles as a Function of Time for Different  $I_{sp}$ 's, Constant Acceleration Case Also Shown**

#### 4.5.4 Constant Thrust Sensitivity Study

The effect of perturbations of the initial LEO orbit on optimal solution locations and time history behaviors of the classical orbital elements is the subject of this section. Optimal solutions for three perturbations of  $a_o$  are shown in Table 12 and the corresponding time histories of  $a$ ,  $i$ ,  $e$ ,  $\alpha$ , and  $\beta$  are shown in Figure 33, Figure 34, and Figure 35 respectively.

**Table 12: Optimal Adjoint Variable Initial Conditions for Constant Thrust LEO to GEO Transfer for Perturbations of  $a_o$**

Case	Reduce $a_o$ by 200 km	Reduce $a_o$ by 100 km	LEO Baseline	Increase $a_o$ by 100 km
$a_o$ (km)	6800	6900	7000	7100
$\lambda_{a,o}$ (sec/km)	1.1291151	0.8583417	0.69733703	0.5512262
$\lambda_{h,o}$ (sec)	637.88965	434.3169	533.6483	479.97333
$\lambda_{k,o}$ (sec)	-8044.9556	-8073.547	-8038.6123	-8018.0605
$\lambda_{p,o}$ (sec)	-4501.453	-3710.8276	-4434.298	-4372.634
$\lambda_{q,o}$ (sec)	-12532.672	-11907.58	-11725.732	-11443.644
$\lambda_{L,o}$ (sec/rad)	437.805	492.61642	520.88696	554.9187
$TOF$ (sec)	55281.285	55173.723	55108.215	55047.832
$f$	$8.01962 \times 10^{-6}$	$2.86172 \times 10^{-5}$	$2.70619 \times 10^{-6}$	$1.22834 \times 10^{-5}$

As shown in the zoomed view of Figure 33, the “switching” behavior observed for  $a(t)$  in the previous thrust magnitude study is evident for perturbations of  $a_o$  as well. Within the

first hour of flight, the spacecraft's semi-major axis "path" is pushed toward a path closely shared by all four time histories. This behavior is reflected in the plot of the control angles shown in Figure 35 as well, as time history traces of  $a$  clearly deviate from each other near the first hour of flight. Once again, the inefficiency associated with  $da/dt < 0$  for  $a_o = 7100$  is within the integration tolerance; however, upon exploring  $a_o = 7200$ , a solution could not be found without widening this tolerance.

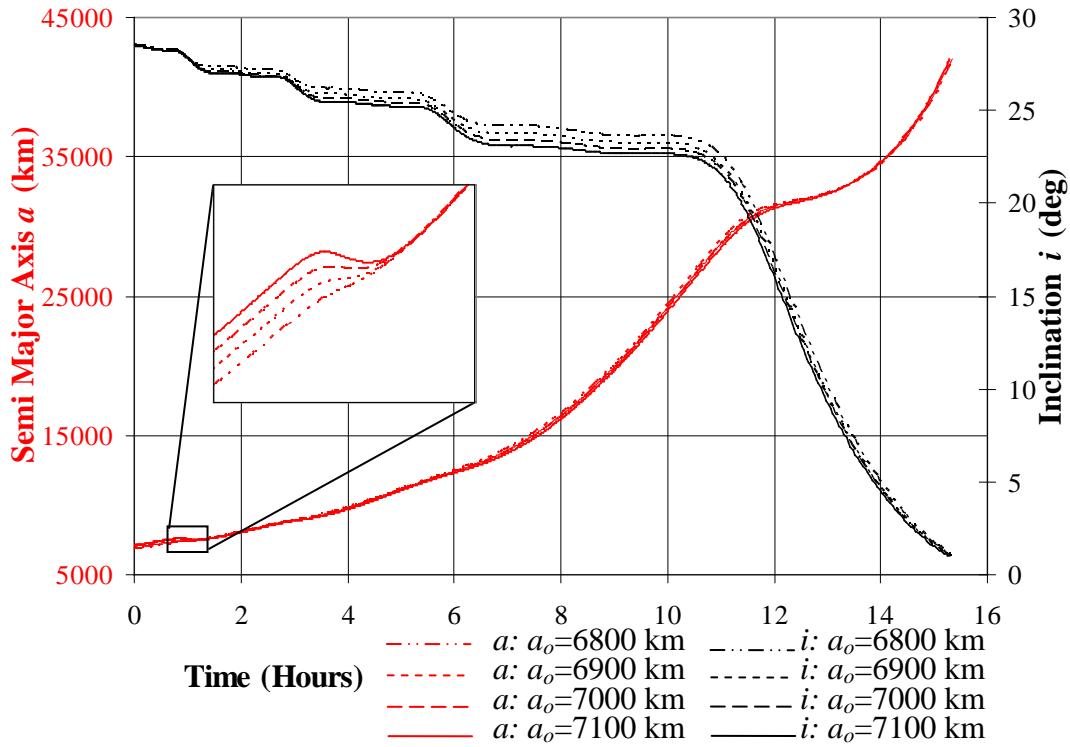


**Figure 33: Semi-Major Axis and Inclination as a Function of Time for Perturbations of  $a_o$**

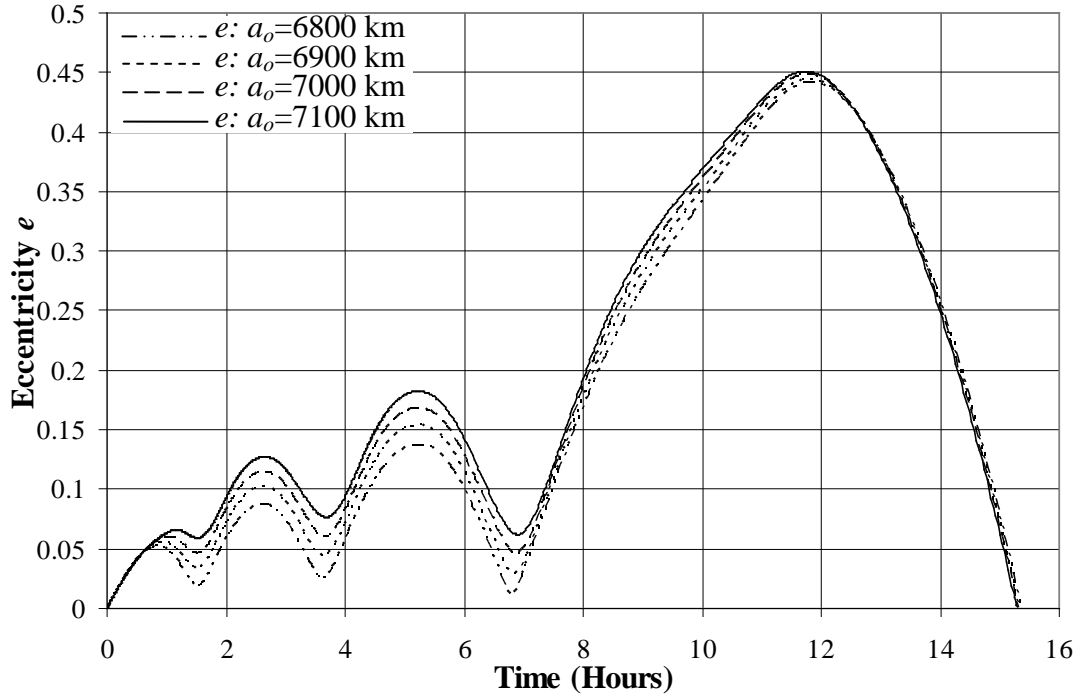


**Figure 34: Eccentricity as a Function of Time for Perturbations of  $a_o$**

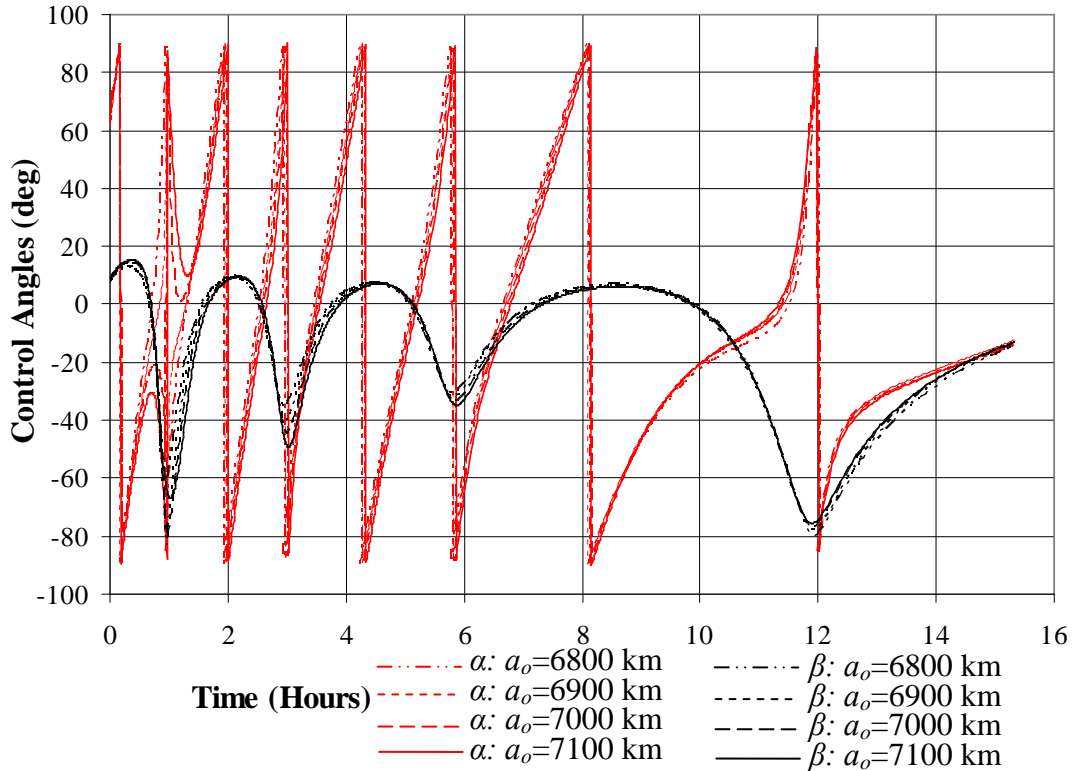


**Figure 35: Yaw  $\alpha$  and Pitch  $\beta$  Angles as a Function of Time for Perturbations of  $a_o$**

Optimal solutions for perturbations of  $i_o$  are shown in Table 13, and corresponding time histories of  $a$ ,  $i$ ,  $e$ ,  $\alpha$ , and  $\beta$  are shown in Figure 36, Figure 37, and Figure 38,

respectively. For small perturbations of  $i_o$ , the traces of  $a$  and  $i$  transition smoothly without any observable “path jumping” behavior as seen previously. In a likely related qualitative observation, the optimal solutions listed in Table 13 were significantly easier to locate than optimal solutions for perturbations of  $a_o$ .

**Table 13: Optimal Adjoint Variable Initial Conditions for Constant Thrust LEO to GEO Transfer for Perturbations of  $i_o$**

Case	Decrease $i_o$ by 1.5°	LEO Baseline	Increase $i_o$ by 1.5°	Increase $i_o$ by 3°
$i_o^\circ$	27	28.5	30	31.5
$\lambda_{a,o}$ (sec/km)	0.6574024	0.69733703	0.69065297	0.71647274
$\lambda_{h,o}$ (sec)	511.76782	533.6483	19.841057	-252.63708
$\lambda_{k,o}$ (sec)	-7961.5703	-8038.6123	-8194.975	-8304.928
$\lambda_{p,o}$ (sec)	-4217.71	-4434.298	-1681.8203	240.4904
$\lambda_{q,o}$ (sec)	-10711.217	-11725.732	-12365.268	-13426.1875
$\lambda_{L,o}$ (sec/rad)	532.33765	520.88696	539.70374	541.8904
TOF (sec)	54951.48	55108.215	55257.68	55453.97
$f$	$2.80097 \times 10^{-6}$	$2.70619 \times 10^{-6}$	$1.14312 \times 10^{-6}$	$4.77427 \times 10^{-6}$

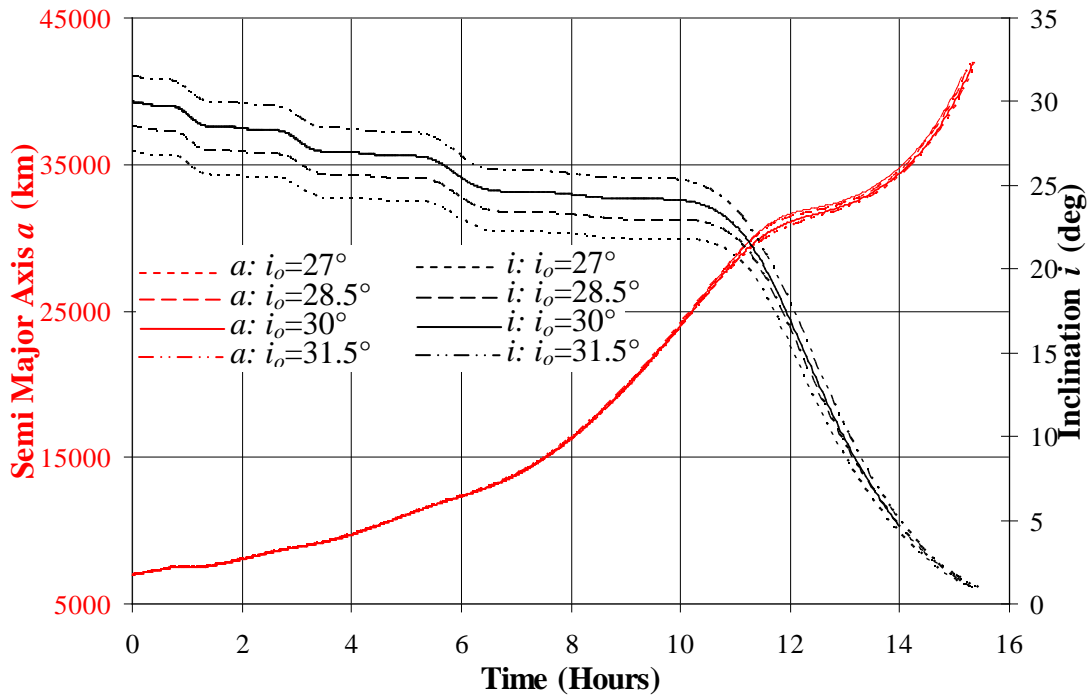


**Figure 36: Semi-Major Axis and Inclination as a Function of Time for Perturbations of  $i_o$**

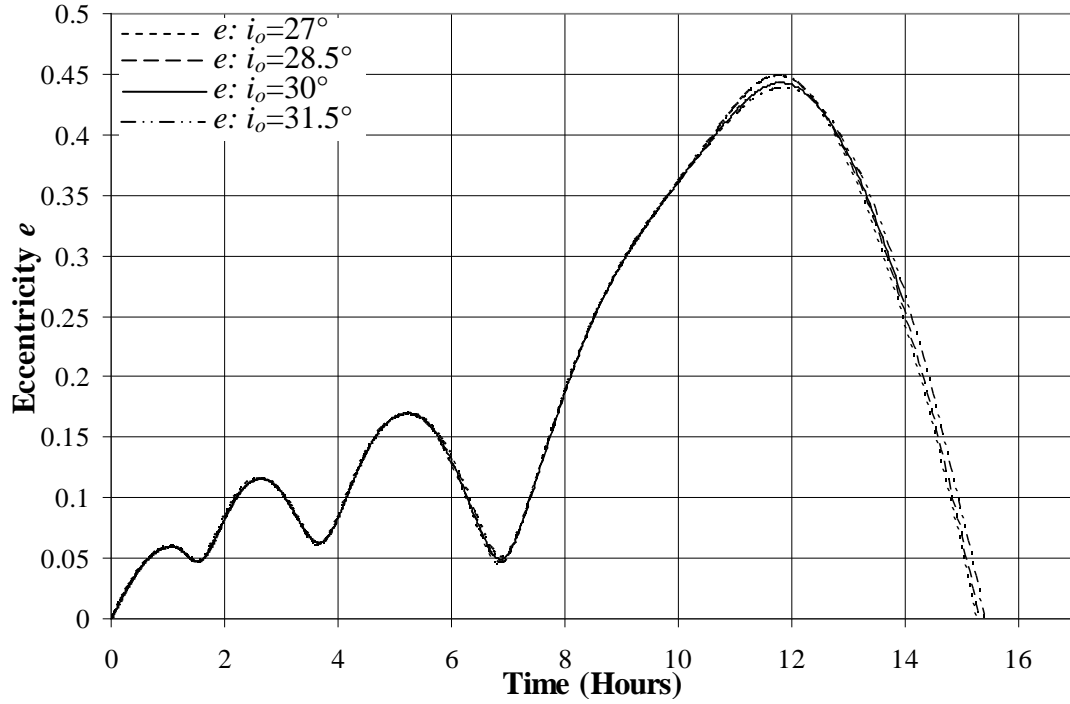


Figure 37: Eccentricity as a Function of Time for Perturbations of  $i_0$

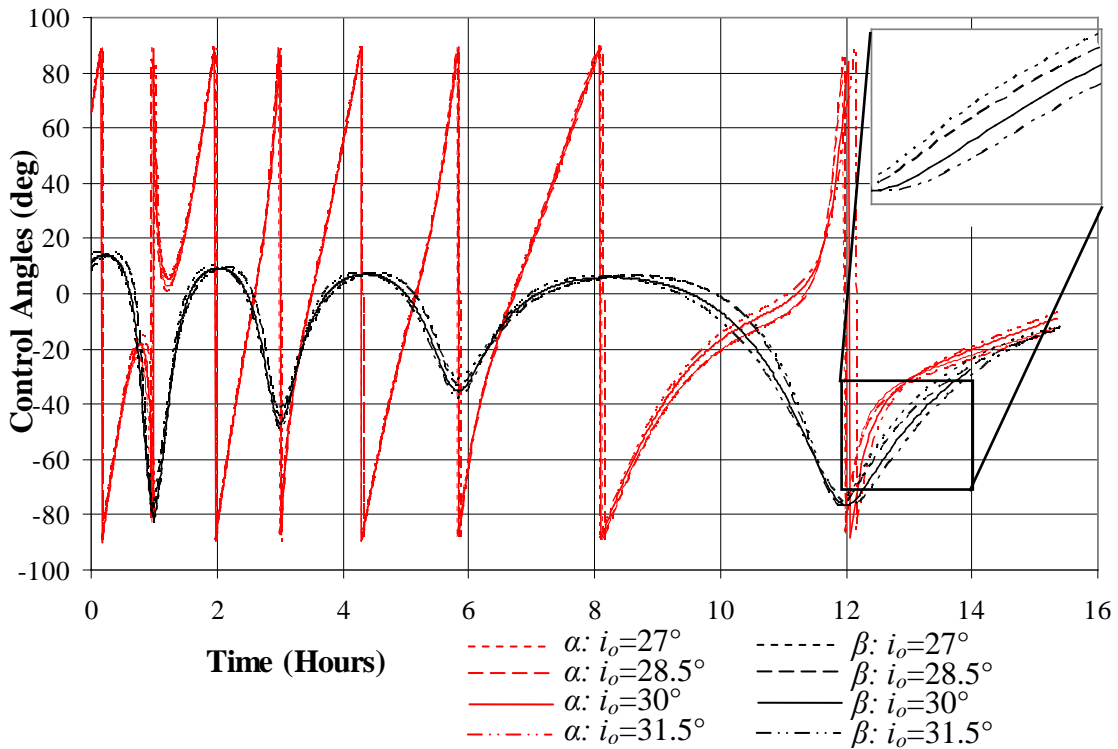


Figure 38: Control Angles as a Function of Time for Perturbations of  $i_0$

Realizations of  $e(t)$  are almost identical between perturbations of  $i_0$ . As one might expect, toward the end of flight, traces of  $i$  for positive perturbations ( $+1.5^\circ$ ,  $+3^\circ$ ) “catch up” and the trace of  $i$  for the negative perturbation ( $-1.5^\circ$ ) “slows down” such that all four

meet at the correct final inclination of  $1^\circ$ . This is undoubtedly the effect of the behavior of  $\beta$  during the transfer as shown in Figure 38. The zoomed view shows more precisely how  $\beta$  influences the observed “catch up” and “slow down” behavior, where positive perturbation transfers have the thrust vector pointed further out of plane for longer than the negative perturbation and baseline LEO transfer.

Due to time constraints, only a single perturbation of  $\Omega_o$  was explored. The optimal solution for a  $+45^\circ$  perturbation is shown in Table 14 and the time histories of  $a$ ,  $i$ ,  $e$ ,  $\alpha$ , and  $\beta$  are shown in Figure 39, Figure 40, and Figure 41, respectively. One would expect identical time histories of the classical orbital elements for any  $\Omega_o$ ; the lack of constraint on  $\theta_f$  suggests that the definition of  $\Omega$  is arbitrary in the context of a specific transfer, and this idea is supported by Figure 39. As shown in Figure 40, the time histories of  $e$  are identical between cases.

**Table 14: Optimal Adjoint Variable Initial Conditions for Constant Thrust LEO to GEO Transfer for a Perturbation of  $\Omega_o$**

Case	LEO Baseline	Increase $\Omega_o$ by $45^\circ$
$\Omega_o^\circ$	$0^\circ$	$45^\circ$
$\lambda_{a,o}$ (sec/km)	0.69733703	0.64365506
$\lambda_{h,o}$ (sec)	533.6483	-5324.0854
$\lambda_{k,o}$ (sec)	-8038.6123	-5765.5884
$\lambda_{p,o}$ (sec)	-4434.298	-11343.348
$\lambda_{q,o}$ (sec)	-11725.732	-5093.073
$\lambda_{L,o}$ (sec/rad)	520.88696	536.1609
$TOF$ (sec)	55108.215	55152.92
$f$	$2.70619 \times 10^{-6}$	$3.49754 \times 10^{-6}$

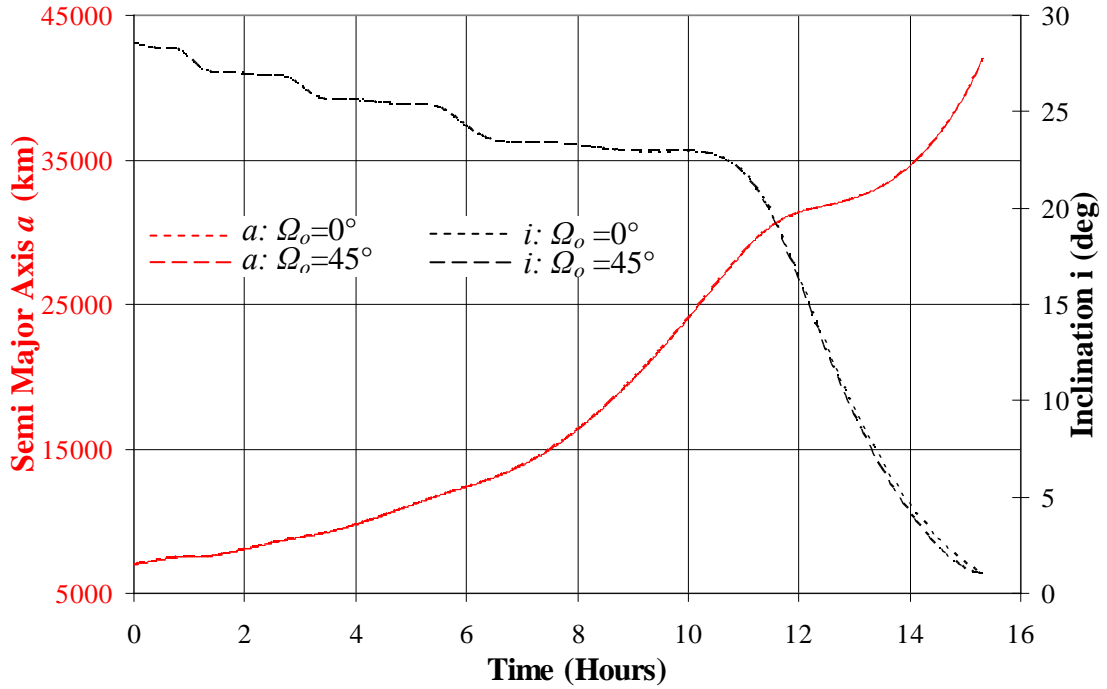


**Figure 39: Semi-Major Axis and Inclination as a Function of Time for a Perturbation of  $\Omega_o$**

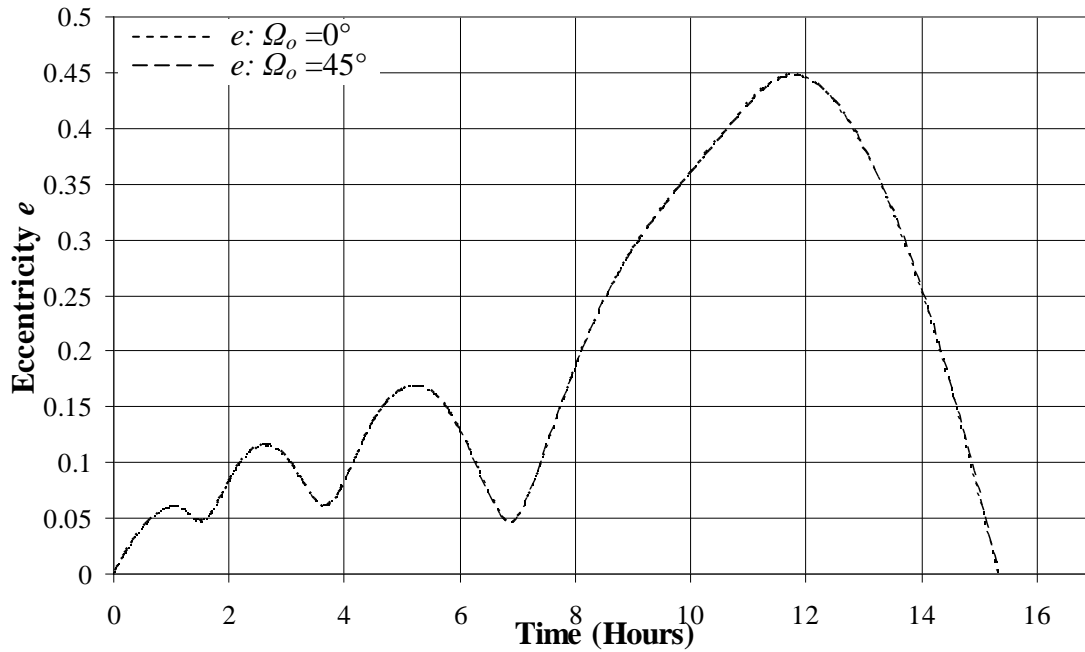


**Figure 40: Eccentricity as a Function of Time for a Perturbation of  $\Omega_o$**

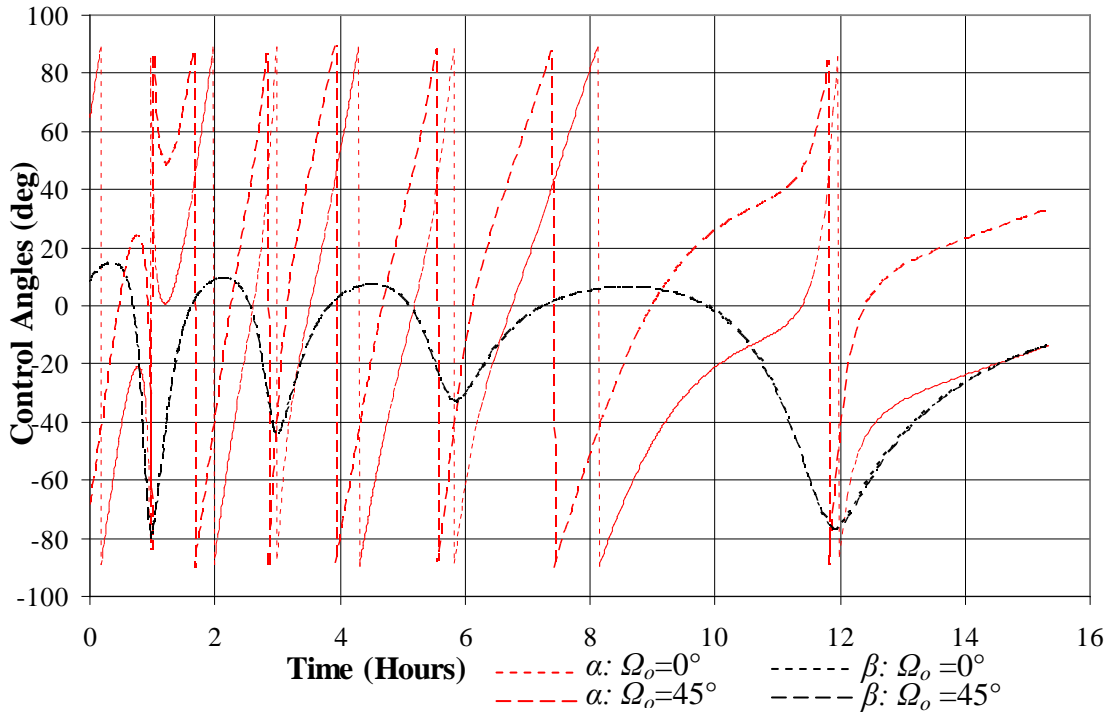


**Figure 41: Control Angles as a Function of Time for a Perturbation of  $\Omega_o$**

The behavior of  $\alpha$  in Figure 41 shows clear differences in time histories between  $\Omega_o = 0^\circ$  and  $\Omega_o = 45^\circ$ . This result is interesting: one would expect identical control angle time histories for such similar  $a$ ,  $i$ , and  $e$  traces since the definition of yaw is independent of an orbit's orientation. Perhaps the manner in which  $\bar{\lambda}$  and  $\bar{x}_e$  are coupled permits various optimal yaw time histories for variations in  $\Omega_o$ . An exploration of more perturbations of  $\Omega_o$  might provide further insight.

By integrating the continuous-thrust problem models with ATSV and permitting the decision maker to observe evolutionary search, optimal trajectories were efficiently located for constant thrust and constant acceleration LEO to GEO transfers. The exploration revealed the manner in which solutions converge to false optima and allowed the user to understand and therefore bypass pre-convergence issues. The inability to locate optimal solutions for some cases and the acquisition of a near optimal solution far from a known optimal reemphasized the necessity of exploring wide bounds on the adjoint variable initial conditions.



## Chapter 5: Conclusions

### 5.1 Conclusions

The Applied Research Lab Trade Space Visualizer (ATSV) has been an effective solution visualization and exploration tool for the test problems and continuous thrust LEO to GEO transfers discussed in this work. Engineering problems were explored both statically and dynamically, and ATSV’s visualization capabilities revealed underlying trends that existed within the objective and decision spaces.

For the continuous thrust spacecraft maneuver problem, a clearly distinct near-optimal set of adjoint variable initial conditions that result in very similar time histories of the classical orbital elements when compared with a known optimal trajectory was located. Optimal solutions were acquired for two engine specific impulses for the constant thrust problem formulation and the sensitivity of one of these solutions to perturbations in the initial LEO orbit was explored. Semi-major axis time histories exhibit “path jumping” behavior early in the transfer for perturbations of  $a_o$  while inclination and eccentricity time histories transition smoothly for small perturbations of  $a_o$  and  $i_o$  in the explored search space. Optimal time histories of the classical orbital elements appear to be independent of perturbations of  $\Omega_o$ .

The “human-in-the-loop” capabilities provided by ATSV’s sampling techniques, the guided Pareto sampler in particular, played an integral role in the efficient acquisition of optimal Pareto solution sets. The exploration of the large decision space in the continuous thrust trajectory optimization problem would not have been temporally feasible without the search acceleration capabilities associated with designer-in-the-loop evolutionary search. By integrating the designer into the evolutionary search algorithm, problem-specific wisdom was gained as information regarding realistic expectations of objective and decision spaces became clear. Through this *a posteriori* knowledge, the designer accelerated search by

1. Ignoring some or all of the known infeasible decision space,
2. Locating potentially promising solutions through previously observed patterns,
3. Stopping pre-converging evolutions early, and
4. Continuing pre-converged evolutions after introducing new promising solutions to the population

ATSV’s visual steering capabilities not only permitted the acquisition of optimal solutions more efficiently than a black-box optimizer, but it also became the means for the designer to more fully understand the nuances particular to a specific engineering problem.




## 5.2 Suggestions for Future Work

Any extended work on the continuous thrust trajectories topic should consider the search of an even wider spectrum of decision variables for both the constant acceleration and constant thrust problem formulations. More sensitivity cases might provide further insight into the relationship between the adjoint variable initial conditions and the time histories of the classical orbital elements and thrust control angles. The sensitivity of optimal trajectories to perturbations in the final desired orbit could be investigated as well. In the interest of model accuracy and actual applicability, the addition of  $J_2$  effects to the system dynamics as well as constraints on the final true anomaly could be added to the problem formulation.

As newer engineering problem models become more and more precise, the computational cost of a single function evaluation grows as well. As shown in this work, when decision space search ranges are expanded, often evolutionary search must be supplemented with larger population sizes. In order to effectively locate Pareto solutions for more complex engineering problem models in a reasonable time frame, designers would benefit from the use of distributed and/or cluster computing. Parallelization would allow for evolutionary search and corresponding real-time visualization of computationally intense problems on a reasonable time scale.

## 5.3 Suggested ATSV Improvements, Modifications, and Future Work

Because ATSV is constantly under development, a number of suggestions have been compiled regarding possible ATSV modifications and improvements. These ideas are summarized as follows.

- Integration with distributed computing or cluster computing mechanisms
- Direct link to MATLAB that would eliminate the need for Spreadsheet Link
- The ability to export only selected points
- Some type of solution de-crowding mechanism, e.g., select points and eliminate redundant solutions, where redundant solutions are defined to be within a certain tolerance of each other
- Allow non-continuous brushing of variables, i.e., the Brush controls could look like 
- Change the “working” animation from the Exploration Engine to a more precise progress bar based on the number of runs selected, i.e., change this  to this  49%
- Add a “pause” button which would allow the designer to pause an evolution in progress and resume it later
- Have solution number and generation number automatically added to all dynamic datasets
- Add functionality to the “show only Pareto points” button, so that the designer can view various evolutionary metrics as an evolution progresses, including

- Only the current population
  - Solutions used in determining scaled vector difference and base vector
- In the Exploration Engine options, suggest a generation size based on the number of inputs and their significant digits
- The ability to take screenshots at regular temporal or generational intervals for video purposes

This thesis includes qualitative justifications for the efficiencies associated with visually steering a trade space when compared to a black-box optimizer. Examining the statistical facts regarding solution quality versus time and/or number of function evaluations would be useful in illustrating the advantages of visual steering over other optimization techniques. Also, calculable information regarding how much problem specific wisdom is gained through the visual steering process versus the black-box optimization process would reinforce the goals of trade space visualization. Quantitative research targeting “human-in-the-loop” vs. “black-box” optimization might articulate ATSV’s motivations to the black-box optimization engineering community more clearly.

## Appendix A: Examples of ATSV's Other Plot Types [16]

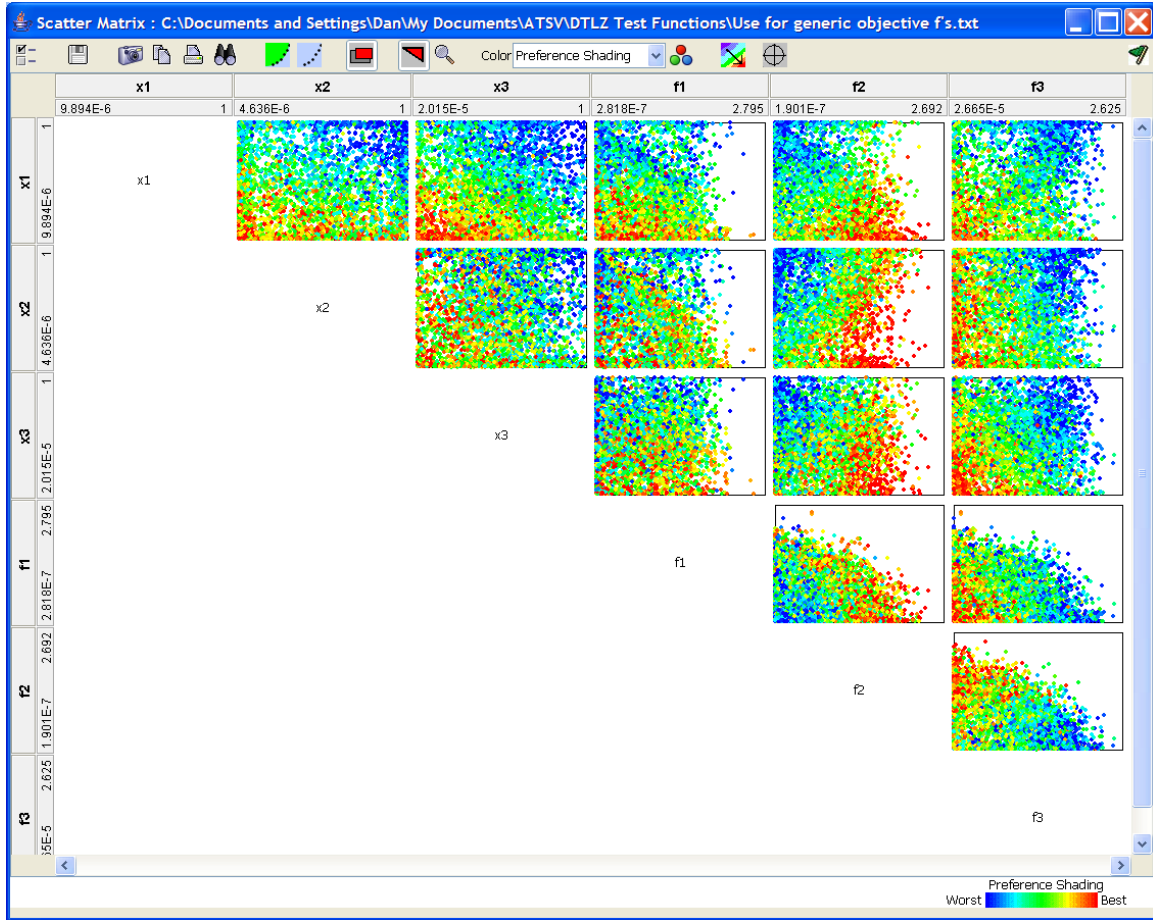
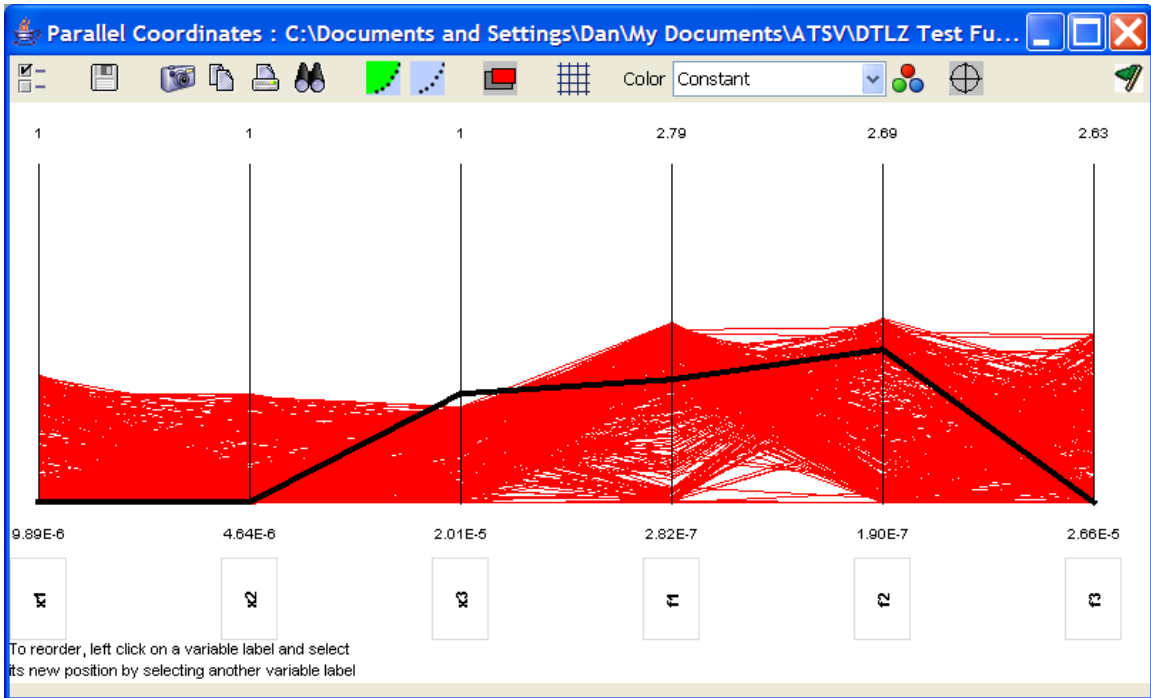
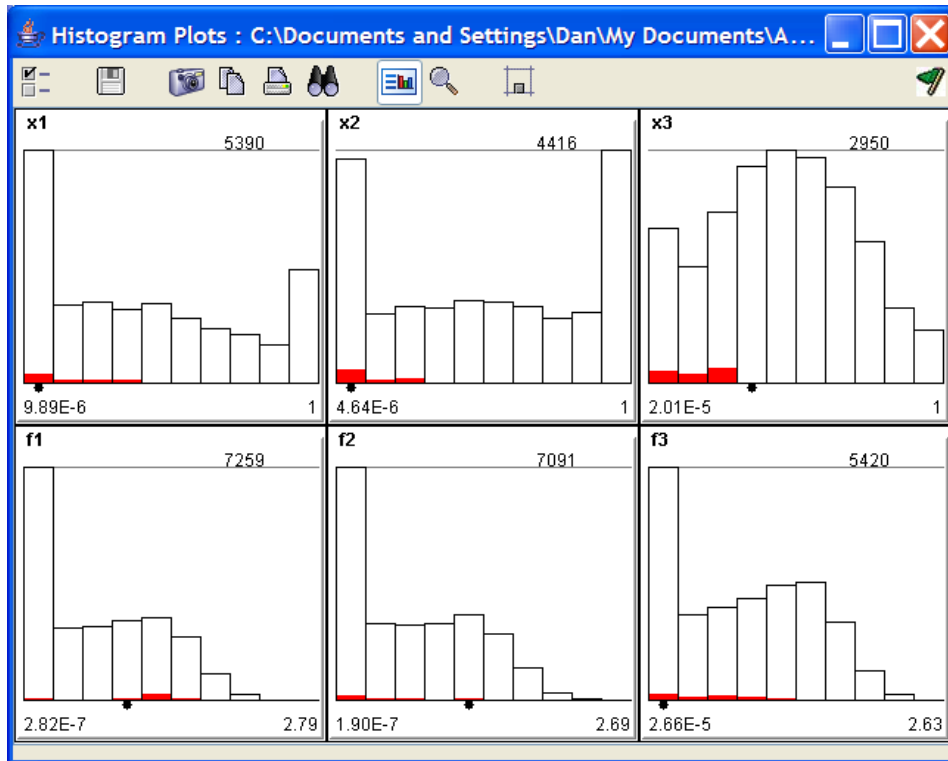


Figure A-1: Scatter Matrix Example



**Figure A-2: Parallel Coordinates Example**



**Figure A-3: Histogram Example**

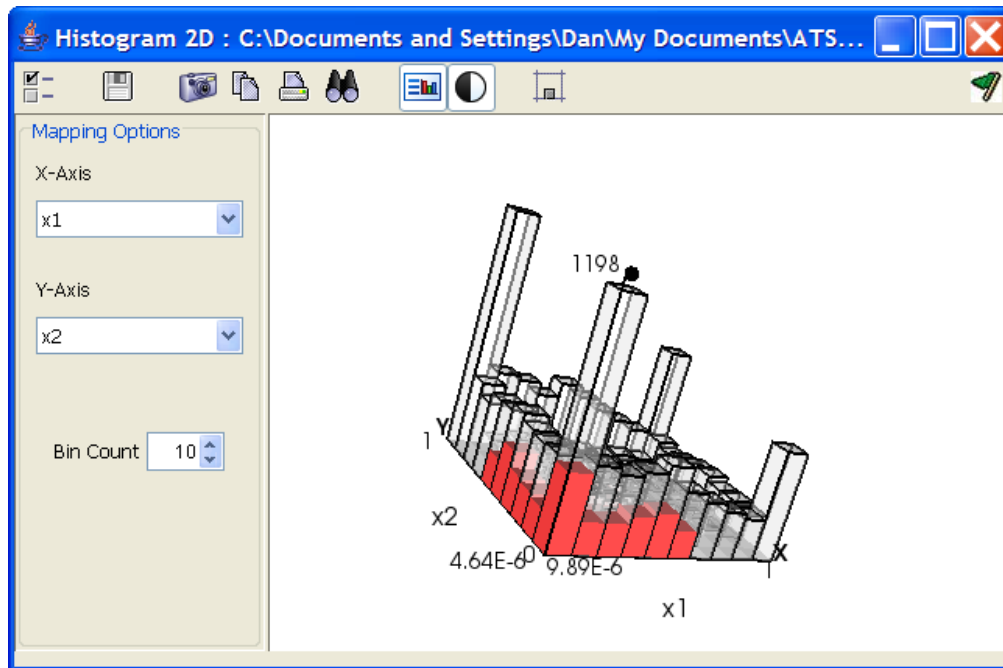


**Figure A-4: 2D Histogram Example**

**Appendix B:** Definition of  $[M]$  as Used in Sections 4.3.1 and 4.3.2

$$M_{11} = \frac{2}{n^2 a} \dot{X} \quad (\text{B.1})$$

$$M_{12} = \frac{2}{n^2 a} \dot{Y} \quad (\text{B.2})$$

$$M_{21} = \frac{G}{na^2} \left( \frac{\partial X}{\partial k} - h\beta \frac{\dot{X}}{n} \right) \quad (\text{B.3})$$

$$M_{22} = \frac{G}{na^2} \left( \frac{\partial Y}{\partial k} - h\beta \frac{\dot{Y}}{n} \right) \quad (\text{B.4})$$

$$M_{23} = \frac{k(qY - pX)}{na^2 G} \quad (\text{B.5})$$

$$M_{31} = -\frac{G}{na^2} \left( \frac{\partial X}{\partial h} + k\beta \frac{\dot{X}}{n} \right) \quad (\text{B.6})$$

$$M_{32} = -\frac{G}{na^2} \left( \frac{\partial Y}{\partial h} + k\beta \frac{\dot{Y}}{n} \right) \quad (\text{B.7})$$

$$M_{33} = -\frac{h(qY - pX)}{na^2 G} \quad (\text{B.8})$$

$$M_{43} = \frac{KY}{2na^2 G} \quad (\text{B.9})$$

$$M_{53} = \frac{KX}{2na^2 G} \quad (\text{B.10})$$

$$M_{61} = \frac{1}{na^2} \left[ -2X + G \left( h\beta \frac{\partial X}{\partial h} + k\beta \frac{\partial X}{\partial k} \right) \right] \quad (\text{B.11})$$

$$M_{62} = \frac{1}{na^2} \left[ -2Y + G \left( h\beta \frac{\partial Y}{\partial h} + k\beta \frac{\partial Y}{\partial k} \right) \right] \quad (\text{B.12})$$

$$M_{63} = \frac{qY - pX}{na^2 G} \quad (\text{B.13})$$

$$M_{13} = 0, M_{41} = 0, M_{42} = 0, M_{51} = 0, M_{52} = 0 \quad (\text{B.14})$$

where

$$X = a \left[ (1 - h^2 \beta) c_F + hk\beta s_F - k \right] \quad (\text{B.15})$$

$$Y = a \left[ (1 - k^2 \beta) s_F + hk\beta c_F - h \right] \quad (\text{B.16})$$

$$\dot{X} = \frac{na^2}{r} \left[ hk\beta c_F - (1-h^2\beta) s_F \right] \quad (\text{B.17})$$

$$\dot{Y} = \frac{na^2}{r} \left[ -hk\beta s_F + (1-k^2\beta) c_F \right] \quad (\text{B.18})$$

$$G = \sqrt{1-h^2-k^2} \quad (\text{B.19})$$

$$\beta = \frac{1}{1+G} \quad (\text{B.20})$$

$$K = 1+p^2+q^2 \quad (\text{B.21})$$

$$\frac{\partial X}{\partial h} = -a \left[ (hc_F - ks_F) \left( \beta + \frac{h^2\beta^3}{1-\beta} \right) - \frac{a}{r} c_F (h\beta - s_F) \right] \quad (\text{B.22})$$

$$\frac{\partial X}{\partial k} = -a \left[ (hc_F - ks_F) \frac{hk\beta^3}{1-\beta} - \frac{a}{r} s_F (h\beta - s_F) + 1 \right] \quad (\text{B.23})$$

$$\frac{\partial Y}{\partial h} = a \left[ (hc_F - ks_F) \frac{hk\beta^3}{1-\beta} + \frac{a}{r} c_F (k\beta - c_F) - 1 \right] \quad (\text{B.24})$$

$$\frac{\partial Y}{\partial k} = a \left[ (hc_F - ks_F) \left( \beta + \frac{k^2\beta^3}{1-\beta} \right) - \frac{a}{r} s_F (k\beta - c_F) \right] \quad (\text{B.25})$$

$$c_F = \cos(F) \quad (\text{B.26})$$

$$s_F = \sin(F) \quad (\text{B.27})$$

$$\text{Eccentric Longitude } F = E + \tan^{-1} \left( \frac{h}{k} \right) \quad (\text{B.28})$$



**Appendix C: Partial Derivatives of  $[M]$  as Used in Equation (9)**

Partial derivatives of  $[M]$  with respect to  $a$ :

$$\frac{\partial M_{11}}{\partial a} = \frac{4}{n^2 a^2} \dot{X} + \frac{2}{n^2 a} \frac{\partial \dot{X}}{\partial a} \quad (\text{C.1})$$

$$\frac{\partial M_{12}}{\partial a} = \frac{4}{n^2 a^2} \dot{Y} + \frac{2}{n^2 a} \frac{\partial \dot{Y}}{\partial a} \quad (\text{C.2})$$

$$\frac{\partial M_{21}}{\partial a} = \frac{G}{na^2} \left[ -\frac{1}{2a} \frac{\partial X}{\partial k} + \frac{\partial^2 X}{\partial a \partial k} - \frac{h\beta}{na} \dot{X} - \frac{h\beta}{n} \frac{\partial \dot{X}}{\partial a} \right] \quad (\text{C.3})$$

$$\frac{\partial M_{22}}{\partial a} = \frac{G}{na^2} \left[ -\frac{1}{2a} \frac{\partial Y}{\partial k} + \frac{\partial^2 Y}{\partial a \partial k} - \frac{h\beta}{na} \dot{Y} - \frac{h\beta}{n} \frac{\partial \dot{Y}}{\partial a} \right] \quad (\text{C.4})$$

$$\frac{\partial M_{23}}{\partial a} = \frac{k}{na^2 G} \left[ -\frac{1}{2a} (qY - pX) + q \frac{\partial Y}{\partial a} - p \frac{\partial X}{\partial a} \right] \quad (\text{C.5})$$

$$\frac{\partial M_{31}}{\partial a} = \frac{G}{na^2} \left[ \frac{1}{2a} \frac{\partial X}{\partial h} - \frac{\partial^2 X}{\partial a \partial h} - \frac{k\beta}{na} \dot{X} - \frac{k\beta}{n} \frac{\partial \dot{X}}{\partial a} \right] \quad (\text{C.6})$$

$$\frac{\partial M_{32}}{\partial a} = \frac{G}{na^2} \left[ \frac{1}{2a} \frac{\partial Y}{\partial h} - \frac{\partial^2 Y}{\partial a \partial h} - \frac{k\beta}{na} \dot{Y} - \frac{k\beta}{n} \frac{\partial \dot{Y}}{\partial a} \right] \quad (\text{C.7})$$

$$\frac{\partial M_{33}}{\partial a} = -\frac{h}{na^2 G} \left[ -\frac{1}{2a} (qY - pX) + q \frac{\partial Y}{\partial a} - p \frac{\partial X}{\partial a} \right] \quad (\text{C.8})$$

$$\frac{\partial M_{43}}{\partial a} = \frac{K}{2na^2 G} \left( -\frac{1}{2a} Y + \frac{\partial Y}{\partial a} \right) \quad (\text{C.9})$$

$$\frac{\partial M_{53}}{\partial a} = \frac{K}{2na^2 G} \left( -\frac{1}{2a} X + \frac{\partial X}{\partial a} \right) \quad (\text{C.10})$$

$$\frac{\partial M_{61}}{\partial a} = -\frac{M_{61}}{2a} - \frac{1}{n \dot{a}} \left[ 2 \frac{\partial X}{\partial a} - G \left( h\beta \frac{\partial^2 X}{\partial a \partial h} + k\beta \frac{\partial^2 X}{\partial a \partial k} \right) \right] \quad (\text{C.11})$$

$$\frac{\partial M_{62}}{\partial a} = -\frac{M_{62}}{2a} - \frac{1}{n \dot{a}} \left[ 2 \frac{\partial Y}{\partial a} - G \left( h\beta \frac{\partial^2 Y}{\partial a \partial h} + k\beta \frac{\partial^2 Y}{\partial a \partial k} \right) \right] \quad (\text{C.12})$$

$$\frac{\partial M_{63}}{\partial a} = -\frac{M_{63}}{2a} + \frac{1}{na^2 G} \left( q \frac{\partial Y}{\partial a} - p \frac{\partial X}{\partial a} \right) \quad (\text{C.13})$$

$$\frac{\partial M_{13}}{\partial a} = 0, \frac{\partial M_{41}}{\partial a} = 0, \frac{\partial M_{42}}{\partial a} = 0, \frac{\partial M_{51}}{\partial a} = 0, \frac{\partial M_{52}}{\partial a} = 0 \quad (\text{C.14})$$

Partial derivatives of  $[M]$  with respect to  $h$ :

$$\frac{\partial M_{11}}{\partial h} = \frac{2}{n^2 a} \frac{\partial \dot{X}}{\partial h} \quad (\text{C.15})$$

$$\frac{\partial M_{12}}{\partial h} = \frac{2}{n^2 a} \frac{\partial \dot{Y}}{\partial h} \quad (\text{C.16})$$

$$\frac{\partial M_{21}}{\partial h} = \frac{-h}{na^2 G} \left( \frac{\partial X}{\partial k} - \frac{h\beta}{n} \dot{X} \right) + \frac{G}{na^2} \left[ \frac{\partial^2 X}{\partial h \partial k} - \left( \beta + \frac{h^2 \beta}{1-\beta} \right) \frac{\dot{X}}{n} - \frac{h\beta}{n} \frac{\partial \dot{X}}{\partial h} \right] \quad (\text{C.17})$$

$$\frac{\partial M_{22}}{\partial h} = \frac{-h}{na^2 G} \left( \frac{\partial Y}{\partial k} - \frac{h\beta}{n} \dot{Y} \right) + \frac{G}{na^2} \left[ \frac{\partial^2 Y}{\partial h \partial k} - \left( \beta + \frac{h^2 \beta}{1-\beta} \right) \frac{\dot{Y}}{n} - \frac{h\beta}{n} \frac{\partial \dot{Y}}{\partial h} \right] \quad (\text{C.18})$$

$$\frac{\partial M_{23}}{\partial h} = \frac{hk}{na^2 G^3} (qY - pX) + \frac{k}{na^2 G} \left( q \frac{\partial Y}{\partial h} - p \frac{\partial X}{\partial h} \right) \quad (\text{C.19})$$

$$\frac{\partial M_{31}}{\partial h} = \frac{h}{na^2 G} \left( \frac{\partial X}{\partial h} + \frac{k\beta}{n} \dot{X} \right) - \frac{G}{na^2} \left[ \frac{\partial^2 X}{\partial h^2} + \frac{h\beta k}{1-\beta} \frac{\dot{X}}{n} + \frac{k\beta}{n} \frac{\partial \dot{X}}{\partial h} \right] \quad (\text{C.20})$$

$$\frac{\partial M_{32}}{\partial h} = \frac{h}{na^2 G} \left( \frac{\partial Y}{\partial h} + \frac{k\beta}{n} \dot{Y} \right) - \frac{G}{na^2} \left[ \frac{\partial^2 Y}{\partial h^2} + \frac{h\beta k}{1-\beta} \frac{\dot{Y}}{n} + \frac{k\beta}{n} \frac{\partial \dot{Y}}{\partial h} \right] \quad (\text{C.21})$$

$$\frac{\partial M_{33}}{\partial h} = -\frac{h^2}{na^2 G^3} (qY - pX) - \frac{1}{na^2 G} \left[ (qY - pX) + h \left( q \frac{\partial Y}{\partial h} - p \frac{\partial X}{\partial h} \right) \right] \quad (\text{C.22})$$

$$\frac{\partial M_{43}}{\partial h} = \frac{K}{2na^2 G} \left( \frac{\partial Y}{\partial h} + \frac{hY}{G^2} \right) \quad (\text{C.23})$$

$$\frac{\partial M_{53}}{\partial h} = \frac{K}{2na^2 G} \left( \frac{\partial X}{\partial h} + \frac{hX}{G^2} \right) \quad (\text{C.24})$$

$$\begin{aligned} \frac{\partial M_{61}}{\partial h} = & \frac{1}{na^2} \left\{ -2 \frac{\partial X}{\partial h} - \frac{h\beta}{G} \left( h \frac{\partial X}{\partial h} + k \frac{\partial X}{\partial k} \right) \right. \\ & \left. + G \left[ \left( \beta + \frac{h^2 \beta^3}{1-\beta} \right) \frac{\partial X}{\partial h} + \frac{hk\beta^3}{1-\beta} \frac{\partial Y}{\partial k} + \beta \left( h \frac{\partial^2 X}{\partial h^2} + k \frac{\partial^2 X}{\partial h \partial k} \right) \right] \right\} \quad (\text{C.25}) \end{aligned}$$

$$\begin{aligned} \frac{\partial M_{62}}{\partial h} = & \frac{1}{na^2} \left\{ -2 \frac{\partial Y}{\partial h} - \frac{h\beta}{G} \left( h \frac{\partial Y}{\partial h} + k \frac{\partial Y}{\partial k} \right) \right. \\ & \left. + G \left[ \left( \beta + \frac{h^2 \beta^3}{1-\beta} \right) \frac{\partial Y}{\partial h} + \frac{hk\beta^3}{1-\beta} \frac{\partial Y}{\partial k} + \beta \left( h \frac{\partial^2 Y}{\partial h^2} + k \frac{\partial^2 Y}{\partial h \partial k} \right) \right] \right\} \quad (\text{C.26}) \end{aligned}$$

$$\frac{\partial M_{63}}{\partial h} = \frac{1}{na^2 G} \left[ \left( q \frac{\partial Y}{\partial h} - p \frac{\partial X}{\partial h} \right) + \frac{h}{G^2} (qY - pX) \right] \quad (\text{C.27})$$

$$\frac{\partial M_{13}}{\partial h} = 0, \quad \frac{\partial M_{41}}{\partial h} = 0, \quad \frac{\partial M_{42}}{\partial h} = 0, \quad \frac{\partial M_{51}}{\partial h} = 0, \quad \frac{\partial M_{52}}{\partial h} = 0 \quad (\text{C.28})$$

Partial derivatives of  $[M]$  with respect to  $k$ :

$$\frac{\partial M_{11}}{\partial k} = \frac{2}{n^2 a} \frac{\partial \dot{X}}{\partial k} \quad (\text{C.29})$$

$$\frac{\partial M_{12}}{\partial k} = \frac{2}{n^2 a} \frac{\partial \dot{Y}}{\partial k} \quad (\text{C.30})$$

$$\frac{\partial M_{21}}{\partial k} = -\frac{k}{na^2 G} \left( \frac{\partial X}{\partial k} - \frac{h\beta}{n} \dot{X} \right) + \frac{G}{na^2} \left[ \frac{\partial^2 X}{\partial k^2} - \frac{h}{1-\beta} \frac{\beta k \dot{X}}{n} - \frac{h\beta}{n} \frac{\partial \dot{X}}{\partial k} \right] \quad (\text{C.31})$$

$$\frac{\partial M_{22}}{\partial k} = -\frac{k}{na^2 G} \left( \frac{\partial Y}{\partial k} - \frac{h\beta}{n} \dot{Y} \right) + \frac{G}{na^2} \left[ \frac{\partial^2 Y}{\partial k^2} - \frac{h}{1-\beta} \frac{\beta k \dot{Y}}{n} - \frac{h\beta}{n} \frac{\partial \dot{Y}}{\partial k} \right] \quad (\text{C.32})$$

$$\frac{\partial M_{23}}{\partial k} = \frac{G^2 + k^2}{na^2 G^3} (qY - pX) + \frac{k}{na^2 G} \left( q \frac{\partial Y}{\partial k} - p \frac{\partial X}{\partial k} \right) \quad (\text{C.33})$$

$$\frac{\partial M_{31}}{\partial k} = \frac{k}{na^2 G} \left( \frac{\partial X}{\partial h} + \frac{k\beta}{n} \dot{X} \right) - \frac{G}{na^2} \left[ \frac{\partial^2 X}{\partial k \partial h} + \left( \beta + \frac{k^2 \beta^3}{1-\beta} \right) \frac{\dot{X}}{n} + \frac{k\beta}{n} \frac{\partial \dot{X}}{\partial k} \right] \quad (\text{C.34})$$

$$\frac{\partial M_{32}}{\partial k} = \frac{k}{na^2 G} \left( \frac{\partial Y}{\partial h} + \frac{k\beta}{n} \dot{Y} \right) - \frac{G}{na^2} \left[ \frac{\partial^2 Y}{\partial k \partial h} + \left( \beta + \frac{k^2 \beta^3}{1-\beta} \right) \frac{\dot{Y}}{n} + \frac{k\beta}{n} \frac{\partial \dot{Y}}{\partial k} \right] \quad (\text{C.35})$$

$$\frac{\partial M_{33}}{\partial k} = -\frac{hk}{na^2 G^3} (qY - pX) - \frac{h}{na^2 G} \left( q \frac{\partial Y}{\partial k} - p \frac{\partial X}{\partial k} \right) \quad (\text{C.36})$$

$$\frac{\partial M_{43}}{\partial k} = \frac{K}{2na^2 G} \left( \frac{\partial Y}{\partial k} + \frac{kY}{G^2} \right) \quad (\text{C.37})$$

$$\frac{\partial M_{53}}{\partial k} = \frac{K}{2na^2 G} \left( \frac{\partial X}{\partial k} + \frac{kX}{G^2} \right) \quad (\text{C.38})$$

$$\frac{\partial M_{61}}{\partial k} = \frac{1}{na^2} \left\{ -2 \frac{\partial X}{\partial k} - \frac{k\beta}{G} \left( h \frac{\partial X}{\partial h} + k \frac{\partial X}{\partial k} \right) \right. \quad (\text{C.39})$$

$$\left. + G \left[ \left( \beta + \frac{k^2 \beta^3}{1-\beta} \right) \frac{\partial X}{\partial k} + \frac{hk\beta^3}{1-\beta} \frac{\partial X}{\partial h} + \beta \left( h \frac{\partial^2 X}{\partial k \partial h} + k \frac{\partial^2 X}{\partial k^2} \right) \right] \right\}$$

$$\frac{\partial M_{62}}{\partial k} = \frac{1}{na^2} \left\{ -2 \frac{\partial Y}{\partial k} - \frac{k\beta}{G} \left( h \frac{\partial Y}{\partial h} + k \frac{\partial Y}{\partial k} \right) \right. \quad (\text{C.40})$$

$$\left. + G \left[ \left( \beta + \frac{h^2 \beta^3}{1-\beta} \right) \frac{\partial Y}{\partial k} + \frac{hk\beta^3}{1-\beta} \frac{\partial Y}{\partial h} + \beta \left( h \frac{\partial^2 Y}{\partial k \partial h} + k \frac{\partial^2 Y}{\partial k^2} \right) \right] \right\}$$

$$\frac{\partial M_{63}}{\partial k} = \frac{1}{na^2 G} \left[ \left( q \frac{\partial Y}{\partial k} - p \frac{\partial X}{\partial k} \right) + \frac{k}{G^2} (qY - pX) \right] \quad (\text{C.41})$$

$$\frac{\partial M_{13}}{\partial k} = 0, \frac{\partial M_{41}}{\partial k} = 0, \frac{\partial M_{42}}{\partial k} = 0, \frac{\partial M_{51}}{\partial k} = 0, \frac{\partial M_{52}}{\partial k} = 0 \quad (\text{C.42})$$

Partial derivatives of  $[M]$  with respect to  $p$ :

$$\frac{\partial M_{23}}{\partial p} = \frac{-kX}{na^2G} \quad (\text{C.43})$$

$$\frac{\partial M_{33}}{\partial p} = \frac{hX}{na^2G} \quad (\text{C.44})$$

$$\frac{\partial M_{43}}{\partial p} = \frac{pY}{na^2G} \quad (\text{C.45})$$

$$\frac{\partial M_{53}}{\partial p} = \frac{pX}{na^2G} \quad (\text{C.46})$$

$$\frac{\partial M_{63}}{\partial p} = \frac{-X}{na^2G} \quad (\text{C.47})$$

$$\frac{\partial M_{11}}{\partial p} = \frac{\partial M_{12}}{\partial p} = \frac{\partial M_{13}}{\partial p} = \frac{\partial M_{21}}{\partial p} = \frac{\partial M_{22}}{\partial p} = \frac{\partial M_{31}}{\partial p} = \frac{\partial M_{32}}{\partial p} = 0 \quad (\text{C.48})$$

$$\frac{\partial M_{41}}{\partial p} = \frac{\partial M_{42}}{\partial p} = \frac{\partial M_{51}}{\partial p} = \frac{\partial M_{52}}{\partial p} = \frac{\partial M_{61}}{\partial p} = \frac{\partial M_{62}}{\partial p} = 0 \quad (\text{C.49})$$

Partial derivatives of  $[M]$  with respect to  $q$ :

$$\frac{\partial M_{23}}{\partial q} = \frac{kY}{na^2G} \quad (\text{C.50})$$

$$\frac{\partial M_{33}}{\partial q} = \frac{-hY}{na^2G} \quad (\text{C.51})$$

$$\frac{\partial M_{43}}{\partial q} = \frac{qY}{na^2G} \quad (\text{C.52})$$

$$\frac{\partial M_{53}}{\partial q} = \frac{qX}{na^2G} \quad (\text{C.53})$$

$$\frac{\partial M_{63}}{\partial a} = \frac{Y}{na^2G} \quad (\text{C.54})$$

$$\frac{\partial M_{11}}{\partial q} = \frac{\partial M_{12}}{\partial q} = \frac{\partial M_{13}}{\partial q} = \frac{\partial M_{21}}{\partial q} = \frac{\partial M_{22}}{\partial q} = \frac{\partial M_{31}}{\partial q} = \frac{\partial M_{32}}{\partial q} = 0 \quad (\text{C.55})$$

$$\frac{\partial M_{41}}{\partial q} = \frac{\partial M_{42}}{\partial q} = \frac{\partial M_{51}}{\partial q} = \frac{\partial M_{52}}{\partial q} = \frac{\partial M_{61}}{\partial q} = \frac{\partial M_{62}}{\partial q} = 0 \quad (\text{C.56})$$

Partial derivatives of  $[M]$  with respect to  $L$ :

$$\frac{\partial M_{11}}{\partial L} = \frac{2}{n^2 r} \frac{\partial \dot{X}}{\partial F} \quad (\text{C.57})$$

$$\frac{\partial M_{12}}{\partial L} = \frac{2}{n^2 r} \frac{\partial \dot{Y}}{\partial F} \quad (\text{C.58})$$

$$\frac{\partial M_{21}}{\partial L} = \frac{G}{nar} \left( \frac{\partial^2 X}{\partial F \partial k} - \frac{h\beta}{n} \frac{\partial \dot{X}}{\partial F} \right) \quad (\text{C.59})$$

$$\frac{\partial M_{22}}{\partial L} = \frac{G}{nar} \left( \frac{\partial^2 Y}{\partial F \partial k} - \frac{h\beta}{n} \frac{\partial \dot{Y}}{\partial F} \right) \quad (\text{C.60})$$

$$\frac{\partial M_{23}}{\partial L} = \frac{k}{narG} \left( q \frac{\partial Y}{\partial F} - p \frac{\partial X}{\partial F} \right) \quad (\text{C.61})$$

$$\frac{\partial M_{31}}{\partial L} = -\frac{G}{nar} \left( \frac{\partial^2 X}{\partial F \partial h} + \frac{k\beta}{n} \frac{\partial \dot{X}}{\partial F} \right) \quad (\text{C.62})$$

$$\frac{\partial M_{32}}{\partial L} = -\frac{G}{nar} \left( \frac{\partial^2 Y}{\partial F \partial h} + \frac{k\beta}{n} \frac{\partial \dot{Y}}{\partial F} \right) \quad (\text{C.63})$$

$$\frac{\partial M_{33}}{\partial L} = -\frac{h}{narG} \left( q \frac{\partial Y}{\partial F} - p \frac{\partial X}{\partial F} \right) \quad (\text{C.64})$$

$$\frac{\partial M_{43}}{\partial L} = \frac{K}{2narG} \frac{\partial Y}{\partial F} \quad (\text{C.65})$$

$$\frac{\partial M_{53}}{\partial L} = \frac{K}{2narG} \frac{\partial X}{\partial F} \quad (\text{C.66})$$

$$\frac{\partial M_{61}}{\partial L} = \frac{1}{nar} \left[ -2 \frac{\partial X}{\partial F} + G \left( h\beta \frac{\partial^2 X}{\partial F \partial h} + k\beta \frac{\partial^2 X}{\partial F \partial k} \right) \right] \quad (\text{C.67})$$

$$\frac{\partial M_{62}}{\partial L} = \frac{1}{nar} \left[ -2 \frac{\partial Y}{\partial F} + G \left( h\beta \frac{\partial^2 Y}{\partial F \partial h} + k\beta \frac{\partial^2 Y}{\partial F \partial k} \right) \right] \quad (\text{C.68})$$

$$\frac{\partial M_{63}}{\partial L} = \frac{1}{narG} \left( q \frac{\partial Y}{\partial F} - p \frac{\partial X}{\partial F} \right) \quad (\text{C.69})$$

$$\frac{\partial M_{13}}{\partial L} = 0, \frac{\partial M_{41}}{\partial L} = 0, \frac{\partial M_{42}}{\partial L} = 0, \frac{\partial M_{51}}{\partial L} = 0, \frac{\partial M_{52}}{\partial L} = 0 \quad (\text{C.70})$$

Partial derivatives of dummy variables X and Y used in Equations C.1-C.70:

$$\frac{\partial^2 X}{\partial a \partial h} = \frac{1}{a} \frac{\partial X}{\partial h} \quad (\text{C.71})$$

$$\frac{\partial^2 X}{\partial a \partial k} = \frac{1}{a} \frac{\partial X}{\partial k} \quad (\text{C.72})$$

$$\frac{\partial^2 Y}{\partial a \partial h} = \frac{1}{a} \frac{\partial Y}{\partial h} \quad (\text{C.73})$$

$$\frac{\partial^2 Y}{\partial a \partial k} = \frac{1}{a} \frac{\partial Y}{\partial k} \quad (\text{C.74})$$

$$\begin{aligned} \frac{\partial \dot{X}}{\partial h} = & \frac{a}{r} \dot{X} \left[ s_F + \frac{a}{r} c_F (ks_F - hc_F) \right] + \frac{na^2}{r} \left\{ h\beta s_F \right. \\ & \left. + (kc_F + hs_F) \left( \beta + \frac{h^2 \beta^3}{1-\beta} \right) + \frac{a}{r} c_F \left[ hk\beta s_F + (1-h^2\beta) c_F \right] \right\} \end{aligned} \quad (\text{C.75})$$

$$\begin{aligned} \frac{\partial \dot{X}}{\partial k} = & \frac{a}{r} \dot{X} \left[ c_F - \frac{a}{r} s_F (ks_F - hc_F) \right] + \frac{na^2}{r} \left\{ h\beta c_F \right. \\ & \left. + (kc_F + hs_F) \frac{hk\beta^3}{1-\beta} - \frac{a}{r} s_F \left[ hk\beta s_F + (1-h^2\beta) c_F \right] \right\} \end{aligned} \quad (\text{C.76})$$

$$\begin{aligned} \frac{\partial \dot{Y}}{\partial h} = & \frac{a}{r} \dot{Y} \left[ s_F + \frac{a}{r} c_F (ks_F - hc_F) \right] - \frac{na^2}{r} \left\{ k\beta s_F \right. \\ & \left. + (kc_F + hs_F) \frac{hk\beta^3}{1-\beta} - \frac{a}{r} c_F \left[ hk\beta c_F + (1-k^2\beta) s_F \right] \right\} \end{aligned} \quad (\text{C.77})$$

$$\begin{aligned} \frac{\partial \dot{Y}}{\partial k} = & \frac{a}{r} \dot{Y} \left[ c_F - \frac{a}{r} s_F (ks_F - hc_F) \right] - \frac{na^2}{r} \left\{ k\beta c_F \right. \\ & \left. + (kc_F + hs_F) \left( \beta + \frac{k^2 \beta^3}{1-\beta} \right) + \frac{a}{r} s_F \left[ hk\beta c_F + (1-k^2\beta) s_F \right] \right\} \end{aligned} \quad (\text{C.78})$$

$$\begin{aligned} \frac{\partial^2 X}{\partial h^2} = & -a \left\{ \frac{2a}{r} c_F \left( \beta + \frac{h^2 \beta^3}{1-\beta} \right) + \frac{h\beta^3}{1-\beta} (hc_F - ks_F) \left[ 3 + \frac{h^2 \beta^2 (3-2\beta)}{(1-\beta)^2} \right] \right. \\ & \left. - \frac{a^2}{r^2} c_F (h\beta - s_F) \left[ -s_F + \frac{a}{r} (h - s_F) \right] + \frac{a^2}{r^2} c_F^3 \right\} \end{aligned} \quad (\text{C.79})$$

$$\begin{aligned} \frac{\partial^2 X}{\partial k^2} = & a \left\{ \frac{2a}{r} s_F \frac{hk\beta^3}{1-\beta} - \frac{h\beta^3}{1-\beta} (hc_F - ks_F) \left[ 1 + \frac{k^2 \beta^2 (3-2\beta)}{(1-\beta)^2} \right] \right. \\ & \left. - \frac{a^2}{r^2} s_F (h\beta - s_F) \left[ -c_F + \frac{a}{r} (k - c_F) \right] - \frac{a^2}{r^2} c_F s_F^2 \right\} \end{aligned} \quad (\text{C.80})$$

$$\begin{aligned} \frac{\partial^2 Y}{\partial h^2} = & a \left\{ \frac{2a}{r} c_F \frac{hk\beta^3}{1-\beta} + \frac{k\beta^3}{1-\beta} (hc_F - ks_F) \left[ 1 + \frac{k^2\beta^2(3-2\beta)}{(1-\beta)^2} \right] \right. \\ & \left. + \frac{a^2}{r^2} c_F (k\beta - c_F) \left[ s_F - \frac{a}{r} (h - s_F) \right] - \frac{a^2}{r^2} s_F c_F^2 \right\} \end{aligned} \quad (\text{C.81})$$

$$\begin{aligned} \frac{\partial^2 Y}{\partial k^2} = & -a \left\{ \frac{2a}{r} s_F \left( \beta + \frac{k^2\beta^3}{1-\beta} \right) - \frac{k\beta^3}{1-\beta} (hc_F - ks_F) \left[ 3 + \frac{k^2\beta^2(3-2\beta)}{(1-\beta)^2} \right] \right. \\ & \left. + \frac{a^2}{r^2} s_F (k\beta - c_F) \left[ c_F - \frac{a}{r} (k - c_F) \right] + \frac{a^2}{r^2} s_F^3 \right\} \end{aligned} \quad (\text{C.82})$$

$$\begin{aligned} \frac{\partial^2 X}{\partial h \partial k} = & -a \left\{ \frac{a}{r} c_F \frac{hk\beta^3}{1-\beta} + \frac{k\beta^3}{1-\beta} (hc_F - ks_F) \left[ 1 + \frac{h^2\beta^2(3-2\beta)}{(1-\beta)^2} \right] \right. \\ & \left. + \frac{a^2}{r^2} (h\beta - s_F) \left[ c_F^2 + \frac{a}{r} (hs_F - s_F^2) \right] - \frac{a^2}{r^2} s_F c_F^2 - \frac{a}{r} s_F \left( \beta + \frac{h^2\beta^3}{1-\beta} \right) \right\} \end{aligned} \quad (\text{C.83})$$

$$\begin{aligned} \frac{\partial^2 X}{\partial k \partial h} = & -a \left\{ \frac{a}{r} c_F \frac{hk\beta^3}{1-\beta} + \frac{k\beta^3}{1-\beta} (hc_F - ks_F) \left[ 1 + \frac{h^2\beta^2(3-2\beta)}{(1-\beta)^2} \right] \right. \\ & \left. - \frac{a^2}{r^2} (h\beta - s_F) \left[ s_F^2 + \frac{a}{r} (kc_F - c_F^2) \right] - \frac{a^2}{r^2} s_F c_F^2 - \frac{a}{r} s_F \left( \beta + \frac{h^2\beta^3}{1-\beta} \right) \right\} \end{aligned} \quad (\text{C.84})$$

$$\begin{aligned} \frac{\partial^2 Y}{\partial h \partial k} = & -a \left\{ \frac{a}{r} s_F \frac{hk\beta^3}{1-\beta} - \frac{h\beta^3}{1-\beta} (hc_F - ks_F) \left[ 1 + \frac{k^2\beta^2(3-2\beta)}{(1-\beta)^2} \right] \right. \\ & \left. - \frac{a^2}{r^2} (k\beta - c_F) \left[ c_F^2 + \frac{a}{r} (hs_F - s_F^2) \right] - \frac{a^2}{r^2} c_F s_F^2 - \frac{a}{r} c_F \left( \beta + \frac{k^2\beta^3}{1-\beta} \right) \right\} \end{aligned} \quad (\text{C.85})$$

$$\begin{aligned} \frac{\partial^2 Y}{\partial k \partial h} = & -a \left\{ \frac{a}{r} s_F \frac{hk\beta^3}{1-\beta} - \frac{h\beta^3}{1-\beta} (hc_F - ks_F) \left[ 1 + \frac{k^2\beta^2(3-2\beta)}{(1-\beta)^2} \right] \right. \\ & \left. + \frac{a^2}{r^2} (k\beta - c_F) \left[ s_F^2 + \frac{a}{r} (kc_F - c_F^2) \right] - \frac{a^2}{r^2} c_F s_F^2 - \frac{a}{r} c_F \left( \beta + \frac{k^2\beta^3}{1-\beta} \right) \right\} \end{aligned} \quad (\text{C.86})$$

$$\frac{\partial X}{\partial F} = a \left[ hk\beta c_F - (1 - h^2\beta) s_F \right] \quad (\text{C.87})$$

$$\frac{\partial Y}{\partial F} = a \left[ -hk\beta s_F + (1 - k^2\beta) c_F \right] \quad (\text{C.88})$$

$$\frac{\partial \dot{X}}{\partial F} = -\frac{a}{r} (ks_F - hc_F) \dot{X} + \frac{a^2 n}{r} \left[ -hk\beta s_F - (1 - h^2\beta) c_F \right] \quad (\text{C.89})$$

$$\frac{\partial \dot{Y}}{\partial F} = -\frac{a}{r}(ks_F - hc_F)\dot{Y} + \frac{a^2 n}{r} \left[ -hk\beta c_F - (1 - k^2\beta)s_F \right] \quad (\text{C.90})$$

$$\frac{\partial^2 X}{\partial F \partial h} = a \left[ (hs_F + kc_F) \left( \beta + \frac{h^2 \beta^3}{1 - \beta} \right) + \frac{a^2}{r^2} (h\beta - s_F)(s_F - h) + \frac{a}{r} c_F^2 \right] \quad (\text{C.91})$$

$$\frac{\partial^2 X}{\partial F \partial k} = a \left[ (hs_F + kc_F) \frac{hk\beta^3}{1 - \beta} + \frac{a^2}{r^2} (h\beta - s_F)(c_F - k) - \frac{a}{r} s_F c_F \right] \quad (\text{C.92})$$

$$\frac{\partial^2 Y}{\partial F \partial h} = -a \left[ (hs_F + kc_F) \frac{hk\beta^3}{1 - \beta} + \frac{a^2}{r^2} (k\beta - c_F)(s_F - h) - \frac{a}{r} s_F c_F \right] \quad (\text{C.93})$$

$$\frac{\partial^2 X}{\partial F \partial k} = -a \left[ (hs_F + kc_F) \left( \beta + \frac{k^2 \beta^3}{1 - \beta} \right) + \frac{a^2}{r^2} (k\beta - c_F)(c_F - k) + \frac{a}{r} s_F^2 \right] \quad (\text{C.94})$$



**Appendix D: Excel Interfaces used for Continuous Thrust Problem Formulations  
from Sections 4.3.1 and 4.3.2**

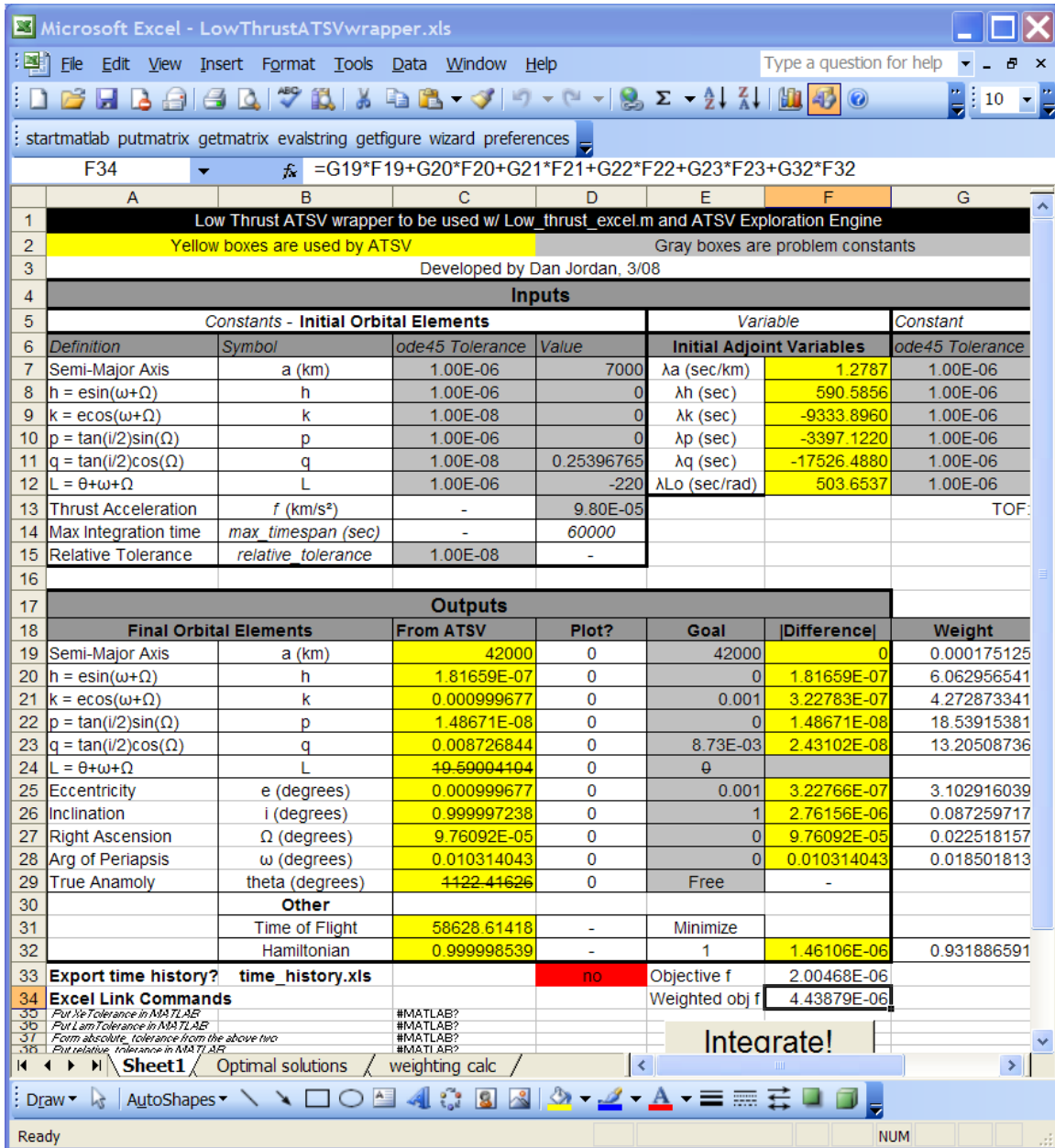


**Figure D-1: Excel Interface for Constant Acceleration Problem Formulation  
(Section 4.3.1)**

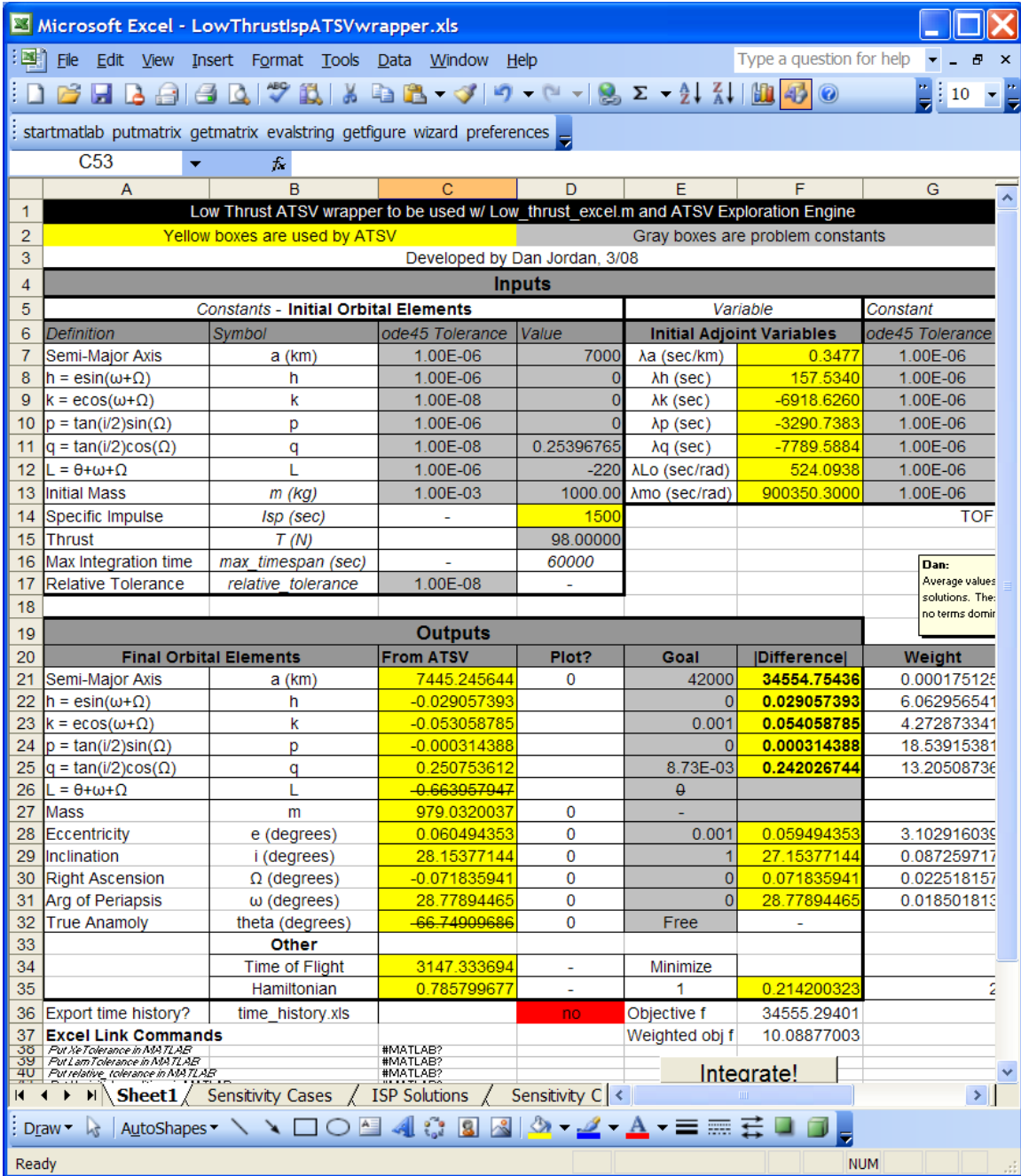


Figure D-2: Excel Interface for Constant Thrust Problem Formulation (Section 4.3.2)

## References

- [1] Soelberg, P. O., 1967. "Unprogrammed Decision Making," *Industrial Management Review*, 8, 19-29.
- [2] Savage, L., 1954. *Foundations of Statistics*. New York, John Wiley and Son.
- [3] Balling, R., 1999. "Design by Shopping: A New Paradigm?," *Proceedings of the Third World Congress of Structural and Multidisciplinary Optimization (WCSMO-3)*, Buffalo, NY, University at Buffalo, pp. 295-297.
- [4] Wilson, T.D., and J.W. Schooler, 1991. "Thinking Too Much: Introspection can Reduce the Quality of Preferences and Decisions", *Journal of Personality and Social Psychology*, 60(2), pp. 181-192.
- [5] Hwang, C.-L. and Masud, A. S., 1979. *Multiple Objective Decision Making - Methods and Applications*, Springer-Verlag, New York
- [6] Yukish, M., 2004. "Algorithms to Identify Pareto Points in Multi-Dimensional Data Sets," *Ph.D. Dissertation*, Department of Mechanical and Nuclear Engineering, The Pennsylvania State University, University Park, PA
- [7] Yukish, M. and Simpson, T. W., 2004. "Analysis of an Algorithm for Identifying Pareto Points in Multi-Dimensional Data Sets," *10th AIAA/ISSMO Multidisciplinary Analysis and Optimization Conference*, Albany, NY, AIAA, AIAA-2004-4324.
- [8] Yukish, M. A. and Simpson, T. W., 2005. "Analysis of an  $O(n^2)$  Algorithm for Identifying Pareto Points in Multi-Dimensional Data Sets," *46th AIAA/ASME/ASCE/AHS/ASC Structures, Structural Dynamics and Materials Conference and 1st AIAA Multidisciplinary Design Optimization Specialist Conference*, Austin, TX, AIAA, AIAA-2005-1812.
- [9] Simpson, T. W., Spencer, D. B., Yukish, M. A., and Stump, G., 2008. "Visual Steering Commands and Test Problems to Support Research in Trade Space Exploration" *12th AIAA/ISSMO Multidisciplinary Analysis and Optimization Conference*, Victoria, British Columbia, Canada. AIAA-2008-6085.
- [10] Messac, A., and X. Chen, 2000. "Visualizing the Optimization Process in Real-Time Using Physical Programming," *Engineering Optimization*, 32(6), pp. 721-747.
- [11] Ng, W.Y., 1991. "Generalized Computer-Aided Design System: A Multiobjective Approach", *Computer-Aided Design*, 23(8), pp. 548-553.
- [12] Eddy, W.F., and A. Mockus, 1995. "Dynamic Visualization in Modeling and Optimization of Ill-Defined Problems: Case Studies and Generalizations", *Technical Report*, Department of Statistics, Carnegie Mellon University, Pittsburgh, PA.
- [13] Carlsen, D. E., 2008. "Assessment of User-Guided Visual Steering Commands During Trade Space Exploration," *Master's Thesis*, Department of Mechanical and Nuclear Engineering. The Pennsylvania State University, University Park, PA.

- [14] Stump, G., Yukish, M. and Simpson, T. W., 2004. "The ARL Trade Space Visualizer: An Engineering Decision-Making Tool," *10th AIAA/ISSMO Multidisciplinary Analysis and Optimization Conference*, Albany, NY, AIAA, AIAA-2004-4568.
- [15] Stump, G., S. Lego, M. Yukish, T.W. Simpson and J.A. Donndelinger, 2007. "Visual Steering Commands for Trade Space Exploration: User-Guided Sampling with Example", *ASME Design Engineering Technical Conferences - Design Automation Conference*, Las Vegas, NV, ASME, DETC2007/DAC-34684, 2007.
- [16] "Applied Research Laboratory Trade Space Visualization", <http://www.atsv.psu.edu>, date cited 1/22/08.
- [17] Madavan, N. K. 2002. "Multiobjective Optimization Using a Pareto Differential Evolution Approach". *Evolutionary Computation, 2002. CEC '02. Proceedings of the 2002 Congress Volume 2*, 12-17 pp. 1145 - 1150
- [18] Price, K. V., Storn, R. M., and Lampinen. J. A., 2005. *Differential Evolution: A Practical Approach to Global Optimization*. Springer Press. New York.
- [19] Deb, K., Agrawal, S., Pratap, A., and Meyarivan, T., 2000. "A Fast Elitist Nondominated Sorting Genetic Algorithm for Multi-objective Optimization: NSGA-II," *Proceedings of the Parallel Problem Solving from Nature VI Conference*, pp. 849-858, Paris, France, 16-20 September.
- [20] Vallado, D. A. 2001. *Fundamentals of Astrodynamics and Applications*. Microcosm Press; pp. 130.
- [21] Edelbaum, T. N., Sackett, L. L., and Malchow, H. L., Nov. 1973. "Optimal Low Thrust Geocentric Transfer," AIAA Paper 73-1074.
- [22] Kechichian, J. A., 1997. "Optimal Low-Earth-Orbit-Geostationary-Earth-Orbit Intermediate Acceleration Orbit Transfer" *Journal of Guidance, Control, and Dynamics*, 20(4), pp. 803-811.
- [23] Igarashi, J. 2004. "Optimal Continuous Thrust Orbit Transfer Using Evolutionary Algorithms." *M. S. Thesis*, Department of Aerospace Engineering, The Pennsylvania State University.
- [24] Kechichian, J. A., 1990. "Equinoctial Orbit Elements: Applications to Optimal Transfer Problems", *AIAA/AAS Astrodynamics Conference*, Portland, OR. AIAA-90-2976